Univerzita Karlova v Praze

Matematicko-fyzikální fakulta

DIPLOMOVÁ PRÁCE

Vladimír Novotný

Studium kosmického záření o nejvyšších energiích

Ústav částicové a jaderné fyziky
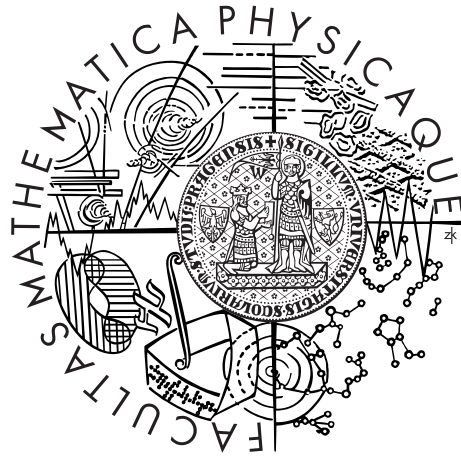
Vedoucí diplomové práce: RNDr. Dalibor Nosek, Dr.

Studijní program: Fyzika

Studijní obor: Jaderná a subjaderná fyzika

Praha 2013

Charles University in Prague

Faculty of Mathematics and Physics

MASTER THESIS

Vladimír Novotný

Study of the Highest Energy Cosmic Rays

Institute of Particle and Nuclear Physics

Supervisor of the master thesis: RNDr. Dalibor Nosek, Dr.

Study programme: Physics

Specialization: Nuclear and Subnuclear Physics

Prague 2013

Název práce: Studium kosmického záření o nejvyšších energiích

Autor: Vladimír Novotný

Ústav: Ústav částicové a jaderné fyziky

Vedoucí diplomové práce: RNDr. Dalibor Nosek, Dr., Ústav částicové a jaderné fyziky

Abstrakt: Zkoumání nejenergetičtějších částic kosmického záření je v centru pozornosti experimentální i teoretické fyziky. Energie těchto částic převyšují až o několik řádů energie dosažitelné na současných urychlovačích. V této práci jsou zkoumány techniky rekonstrukce atmosférických spršek měřených na Observatoři Pierra Augera. Pro tento účel byly modelovány spršky pomocí simulačního programu CORSIKA. Rozlišení rekonstrukčních metod byla určena pomocí dat naměřených na Observatoři Pierra Augera a také pomocí simulací. Hlavní důraz práce je kladen na rekonstrukci pomocí více fluorescenčních teleskopů. Tato rekonstrukce může sloužit k nezávislému ověření experimentálních výsledků Observatoře.

Klíčová slova: Spršky kosmického záření, rekonstrukční techniky, rekonstrukce pomocí více teleskopů, CORSIKA.

Title: Study of the highest energy cosmic rays

Author: Vladimír Novotný

Department: Institute of Particle and Nuclear Physics

Supervisor: RNDr. Dalibor Nosek, Dr., Institute of Particle and Nuclear Physics

Abstract: Research of the highest energy cosmic ray particles is in the middle of the interest of theoretical and experimental physics. Their energies are several orders of magnitude higher than energies accessible at present accelerators. In this work, the reconstruction techniques of extensive air showers measured at the Pierre Auger Observatory are studied. For this purpose, extensive air showers are modelled in the simulation tool CORSIKA. Data collected at the Pierre Auger Observatory together with simulations are used to calculate resolutions of reconstruction methods. The Multiple–eye reconstruction is the main interest of this work. It can be used for independent verification of experimental results of the Observatory.

Keywords: Cosmic ray showers, reconstruction techniques, Multiple–eye reconstruction, CORSIKA.

Contents

Introduction

Physicists can study elementary particles on accelerators, which are capable to achieve energies up to 14 TeV in the central mass system (CMS) at present time. Besides, a flux of extremely energetic cosmic ray (CR) particles comes to the Earth from the space. Some of these particles carry energies over 10^{20} eV in the Earth's laboratory frame, which correspond to the CMS energies above 400 TeV for proton–proton collisions. This is one of the reasons why it is interesting to study the cosmic rays. Up to now, the largest CR experiment has been the Pierre Auger Observatory.

In the first two Chapters of this thesis, I present a basic information about cosmic rays and the Pierre Auger Observatory. For purpose of the CR studies the models based on extrapolations of the accelerator data are used. These models are implemented in the tools to simulate extensive air showers. Monte Carlo simulation code called CORSIKA is discussed in Chapter 3. In Chapter 4, an overview of reconstruction techniques is given and the resolutions of investigated reconstruction techniques are calculated in Chapter 5.

This thesis is aimed to study reconstruction techniques of extensive air showers measured at the Pierre Auger Observatory. The main goal is to explore possibilities of the Multiple–eye reconstruction which is currently not used at the Pierre Auger Observatory. Multiple–eye reconstruction technique processes data from air fluorescence measurement. In comparison with two other methods used at the Pierre Auger Observatory, with the Surface Detector reconstruction and the Hybrid reconstruction, it does not utilize the surface detector data. This advantage could be used to independent verification of experimental results.

1. Fundamentals of Cosmic Rays

Fundamental pieces of information about cosmic ray (CR) particles are summarized in this Chapter. CRs are charged particles coming from the space and hitting the Earth's atmosphere. The most energetic CR particles are called ultra–high energy cosmic ray (UHECR) particles. Brief history of CR measurements is presented in Section 1.1. CR flux, i.e. their energy spectrum, is presented in Section 1.2. Basic ideas of the possible acceleration mechanisms and probable places of the UHECR origin are described in Section 1.3. CR propagation in extragalactic space is briefly summarized in Section 1.4. Extensive air shower (EAS) characteristics, which are studied in the rest of the thesis, are introduced in Section 1.5.

1.1 History

The CRs was detected at first by Victor Hess in 1912 in the series of balloon flights up to an altitude of 5300 m a.b.l. He found that ionization of the atmosphere is approximately four times higher in this altitude than at the ground. The first detection of the EAS induced by a high energy particle in the atmosphere was made by B. Rossi in 1934. He saw that counters coincidentally registered a big number of particles even if they were separated by a large distance. Another step of the EAS measurement was made by Pierre Auger in 1939. Improved resolution capabilities of coincidence circuits of Geiger-Mūller counters made by Maze in 1938 allowed Auger to estimate energies of the primary particles to an energy of 10^{15} eV. He assumed that CRs consist of electrons. This energy was over five times of magnitude higher than any other considered energy of particles before.

Determination of the incoming directions of the showers was another problem. It was solved by the MIT team led by Bassi in 1954. They introduced technique of directional reconstruction from time differences of registered signals in scintillation detectors separated by several tens of meters. In 1954-1957, Harvard Agassiz Station project ran. It had 15 scintillation detectors with an area of 0.9 m^2 each. From this experiment, energy spectrum in the range of $3 \cdot 10^{15} - 10^{18}$ eV was measured. This detector array was a prototype for other experiments Chacaltaya in Bolivia and Volcano Ranch in New Mexico. The latter one was the first among the huge detector arrays.

Using this array, Lindsey measured the first event with an energy over 10^{20} eV. Other huge surface detectors were Haverah Park in Great Britan [12], SUGAR in Australia [18], Yakutsk in Russia [16] and AGASA in Japan [65]. Simultaneously, experiments HiRes [10] and HiRes II [63], that measured air fluorescence, took place in Utah. At present time, HiRes and AGASA experiments are combined as Telescope Array experiment in Utah [44]. Nowadays, the biggest CR experiment combining air fluorescence telescopes and surface array covering an area over 3000 km^2 has been the Pierre Auger Observatory in Argentina [53]. Information comes from Ref.[52].

1.2 Energy Spectrum

Energy spectrum, i.e. the CR flux as a function of the energy, measured up to now is discussed in this Section. The energy spectrum is one of the most important experimental results presented by every CR experiment. Together with other quantities, like mass composition, it can provide information about the acceleration mechanism in the CR sources as well as about their approximate distances. These features are discussed in Sections 1.3 and 1.4, respectively.

Energy spectra compiled from recent experiments are depicted in Figs.1.1 and 1.2, respectively. The overall approximate dependence of E^{-3} is shown in Fig.1.1. More detailed view of the high–energy part of the spectrum is shown in Fig.1.2. In this picture, the CR flux is multiplied by $E^{2.7}$ to point up features deviating from the overall dependence.

The most important features are the Knee at energy about $10^{15.5}$ eV, the Ankle at about $10^{18.8}$ eV and the Second Knee at about $10^{17.8}$ eV. Names of these features come from the shape of the spectrum, that evokes a human leg. The Knee is usually explained as the energy for which magnetic fields in our Galaxy are unable to keep protons or lighter nuclei inside. This implies decrease of CR flux at the Knee. Heavier nuclei are kept inside up to the energy of the Second Knee. The Ankle is usually explained as the region where the extragalactic component of the CRs becomes dominant over the Galactic one.

1.3 Origin

Possible mechanisms of CR acceleration to high energies are summarized in this Section. Whether these mechanisms are able to accelerate particles to as high energies as are measured is a subject of discussion. Possible astrophysical sources are discussed also. Origin of CRs is still an open question.

1.3.1 Fermi theory

The first attempt to explain acceleration of the CR particles is the so called Fermi second order theory. It is named after E. Fermi, who proposed it in 1949. Principle of the acceleration is the fact that particles gain energy on average when scatters off magnetized clouds. Gas of interstellar medium have random velocities V of approximately 15 km s^{-1}. The CR particles enters a cloud and scatters off irregularities in the magnetic field which is tied to the cloud, because it is partly ionized. All interactions within the cloud are considered elastic, thus there is no change in energy in the cloud frame. The direction of outgoing CR particles is randomized.

Consider a CR particle entering a cloud with energy E_1 and momentum p_1 travelling in a direction making angle θ_1 with the cloud direction. After scattering inside the cloud, it exits with energy E_2 and momentum p_2 at angle θ_2 to the cloud direction. Scheme of this situation is depicted in Fig.1.3. The energy change is obtained by applying the Lorentz transformations between the laboratory frame (unprimed) and the cloud frame (primed). Transformation to the cloud frame is

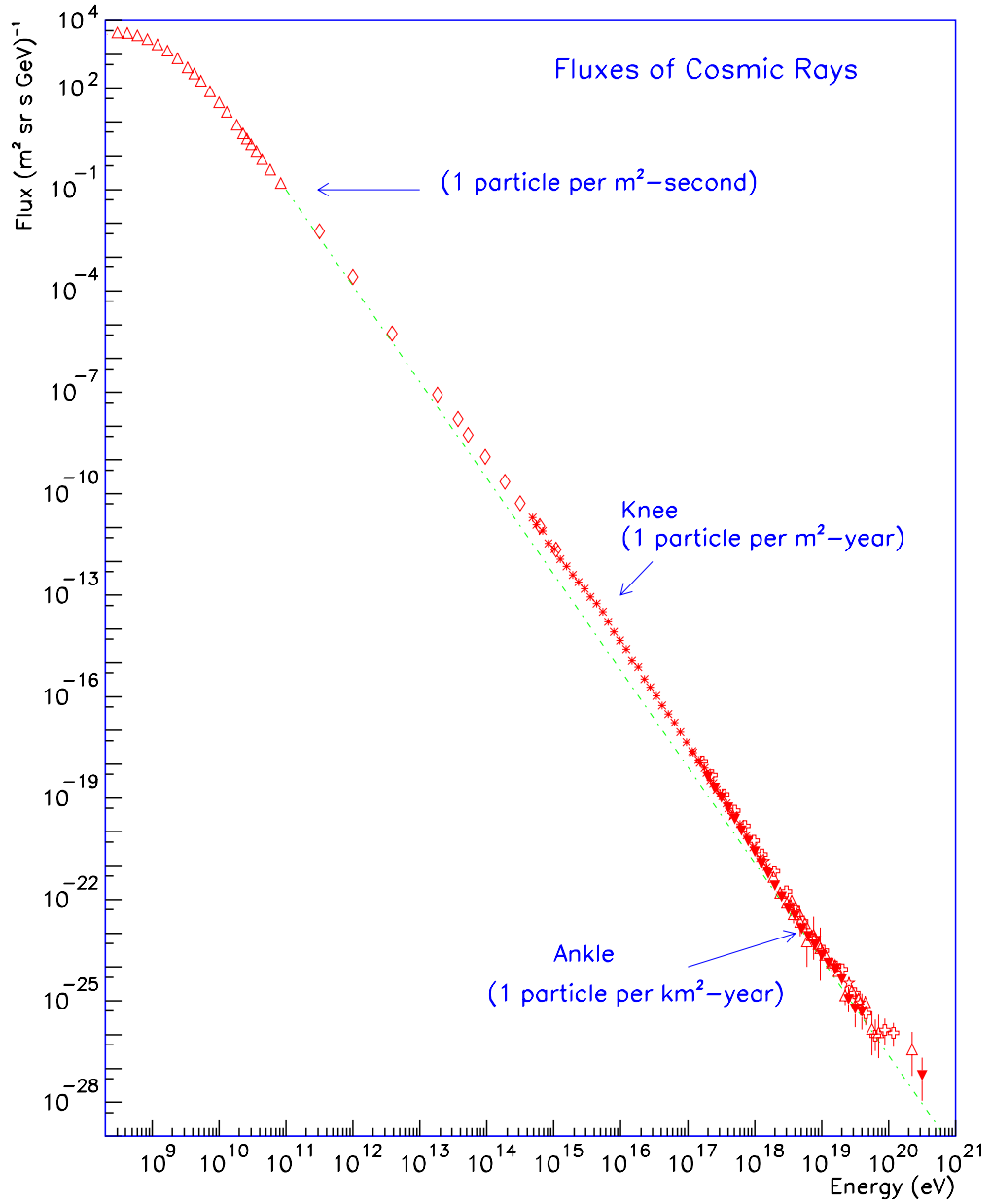$$E_1' = \gamma E_1(1 - \beta \cos\theta_1), \tag{1.1}$$

Figure 1.1: CR energy spectrum in the energy range of $E = 10^8 .. 10^{20}$ eV. Overall approximate dependence of E^{-3} is shown. Knee and Ankle regions are marked. Picture is taken from Ref.[3].
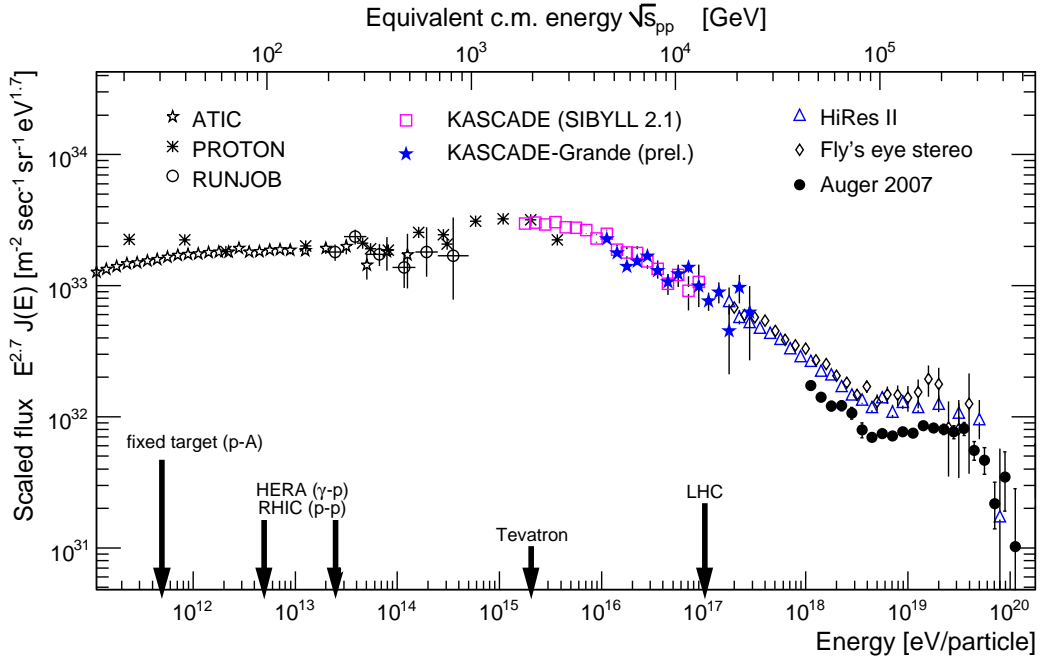
Figure 1.2: CR energy spectrum in the energy range of $E = 10^{11}..10^{20}$ eV. CR flux is multiplied by $E^{2.7}$. Energy capabilities of several accelerators are shown. Picture is taken from Ref.[68].

where $\beta = \frac{V}{c}$, c is the speed of light in vacuum and $\gamma = \frac{1}{\sqrt{1-\beta^2}}$. After exiting from the cloud, the energy in the laboratory frame is

$$E_2 = \gamma E_2'(1 + \beta \cos\theta_2'). \tag{1.2}$$

Because there is no change in energy in the cloud, $E_2' = E_1'$. We obtain energy change in the laboratory frame

$$\frac{\Delta E}{E} = \frac{1 - \beta\cos\theta_1 + \beta\cos\theta_2' - \beta^2\cos\theta_1\cos\theta_2'}{1 - \beta^2} - 1. \tag{1.3}$$

Inside the cloud, particles scatter many times, so their directions are randomized. This implies

$$\langle\cos\theta_2'\rangle = 0. \tag{1.4}$$

The average value of $\cos\theta_1$ depends on the rate at which CRs collide with clouds at different angles. The rate of collisions is proportional to the relative velocity between the cloud and the particles, so the probability per unit solid angle of having a collision at angle θ_1 is proportional to $(v - V\cos\theta_1)$. For ultrarelativistic particles $v = c$ and

$$\frac{dp}{d\Omega_1} \propto (1 - \beta\cos\theta_1). \tag{1.5}$$

One can write

$$\langle\cos\theta_1\rangle = \frac{\int \cos\theta_1 \frac{dp}{d\Omega_1} d\Omega_1}{\int \frac{dp}{d\Omega_1} d\Omega_1} = -\frac{\beta}{3}, \tag{1.6}$$

Figure 1.3: Interaction of entering CR particle, with energy E_1 and momentum p_1, with a cloud of magnetized matter. Particle exits the cloud with energy E_2 and momentum p_2. V is the velocity of the cloud. Picture is taken form Ref.[59].
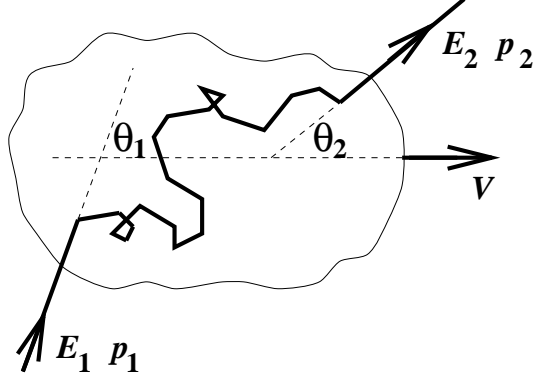
giving approximately [32]

$$\frac{\Delta E}{E} = \frac{1 + \frac{\beta^2}{3}}{1 - \beta^2} - 1 \approx \frac{4}{3}\beta^2 \tag{1.7}$$

for $\beta \ll 1$. Because of quadratic dependence of the energy gain on β, this mechanism is called the second order acceleration.

Energy gain in each interaction is constant, therefore, after n passages through the cloud the energy of the cosmic particle is

$$E_n = E_0 \left(1 + \frac{\Delta E}{E}\right)^n. \tag{1.8}$$

Then, the number of passages needed to reaching this energy is

$$n = \frac{\log \frac{E_n}{E_0}}{\log \left(1 + \frac{\Delta E}{E}\right)}. \tag{1.9}$$

In each iteration, particle can escape the acceleration region with probability P. The probability that particle reach energy E_n is $(1 - P)^n$. The number of particles that are accelerated to energies over E_n is proportional to the number of particles that passed the cloud more then $n-$times. Using Eq.(1.9) one has [32]

$$
\begin{aligned}
N(> E_n) &= N_0 \sum_{k=n}^{\infty}(1-P)^k = N_0 \sum_{k=0}^{\infty}(1-P)^k - N_0 \sum_{k=0}^{n}(1-P)^k \\
&= N_0 \frac{1}{1-(1-P)} - N_0 \frac{1-(1-P)^n}{1-(1-P)} \\
&= \frac{N_0}{P}(1-P)^{\log \frac{E_n}{E_0} / \log\left(1 + \frac{\Delta E}{E}\right)} \propto \frac{N_0}{P}\left(\frac{E_n}{E_0}\right)^{-\Gamma},
\end{aligned} \tag{1.10}
$$

where $\Gamma \simeq \frac{P}{\frac{\Delta E}{E}}$. In Eq.(1.10) the exponential dependence of the energy spectrum on E is derived. Quantity Γ is known as a spectral index.
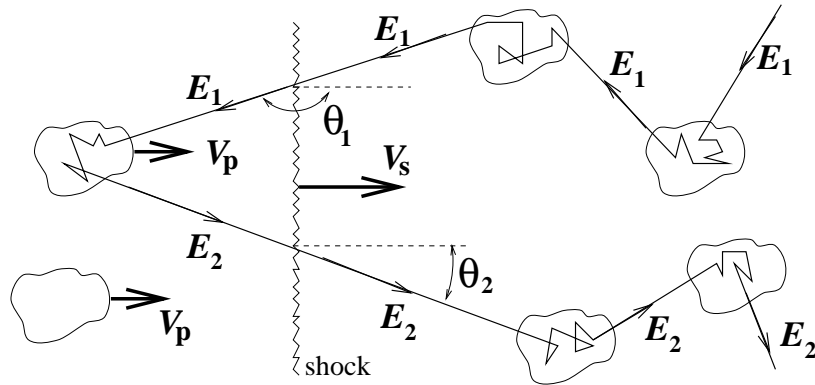
6

Figure 1.4: CR particle interaction with shock wave moving with velocity V_S. Picture is taken from Ref.[59].

Quadratic dependence on the small factor β in the Fermi second order theory causes inefficient acceleration. Also a value of the Γ is not determined.

More efficient mechanism of acceleration is Fermi first order theory proposed in 1970's. In this theory, CR particles are accelerated at supernova shock waves or other astrophysical shocks. In supernova eruptions, material of several Sun masses is thrown away with velocity about 10^4 km s^{-1}. It is about thousand times higher velocity then the speed of sound in interstellar medium. Material thrown away moves against surrounding magnetized medium and makes shock waves. Accelerating particle is moving at the front of the shock wave and scatters off back and front material as in Fermi original theory. This situation is shown in Fig.1.4. By considering the rate at which CR particles cross the shock from downstream to upstream, and upstream to downstream, one finds $\cos\theta_1 = -\frac{2}{3}$ and $\cos\theta_2 = \frac{2}{3}$, giving the average energy gain [59]

$$\frac{\langle\Delta E\rangle}{E} \simeq \frac{4}{3}\beta \simeq \frac{4}{3}k\frac{V_S}{c}, \tag{1.11}$$

where k is a constant depending on the medium material and V_S is the shock wave velocity. This energy gain can be substituted into Eq.(1.10). In this theory, energy gain linearly depends on β, so the mechanism is called first order. More details on Fermi acceleration can by found in Ref.[59].

Maximal energies that are achievable by Fermi mechanism are much higher for protons and nuclei then for electrons. Electrons lose much more energy by synchrotron radiation. Because of that, electrons are not primary particles of UHECRs. Synchrotron radiation, relativistic effects, accounting for radiation pressure and other effects put subsequent restrictions on maximal achievable energies. For more details see Refs.[20] and [59].

1.3.2   Possible Sources

In general, sources that are able to accelerate CR particles up to energies of 10^{20} eV have to be large. Area of regions where acceleration takes place should be comparable to the Larmor radius of the particles in magnetic field in the regions.

On the other hand, magnetic field must be sufficiently weak because particles can not lose much energy through synchrotron radiation. The Larmor radius is given by

$$R_L = \frac{E}{ZeBc},$$ (1.12)

where E is the energy of the particle, Ze is its charge and B is the magnetic induction of the medium. It can be shown, see Ref.[52], that overall energy of the magnetic fields of objects where acceleration takes place must be

$$W = \frac{B^2}{4\pi}\frac{4}{3}\pi R_L^3.$$ (1.13)

This energy must scale with γ^5, where γ is the relativistic Lorentz factor of the particle.

It is assumed that CR particles up to energy of 10^{15} eV originates at diffusive shock waves of supernovas. This process can accelerate more charged nuclei up to energy of 10^{18} eV. Maximal achievable energy is given by [52]

$$E_{\max} = kZeBR\beta c,$$ (1.14)

where $k < 1$ is a constant depending on explicit acceleration mechanism, B is the magnetic induction in the shock wave, R is its size and βc is its velocity.

According to Eq.(1.14), A. J. Hillas draw diagram, see Fig.1.5, that shows astrophysical objects that can be assumed as CR sources. Objects are placed with respect to their sizes and magnetic fields.

1.4   Propagation in Extragalactic Space

Effects that influence CRs on a way from sources to the Earth are summarized in this Section. Deflections in magnetic fields and interactions with the cosmic microwave background radiation (CMB) are the most important effects. More details and simulations of CR propagation can be found in my bachelor's thesis [54].

Deflections in extragalactic magnetic fields for protons are shown in Fig.1.6. Trajectories of protons with energies around 10^{20} eV are almost straight. If the distance of the source from the observer is a few Mpc, even for energies of 10^{19} eV the source should be identified.

1.4.1   Interaction with the CMB

CRs are strongly influenced by the CMB and the cosmic infrared background radiation (CIRB) on their journey through the space. According to theories, the CMB is an artefact of early stages of the universe development. At present time, the CMB fills the space with density of about 400 particles per cm^3 and it has temperature of 2.73 K. This temperature corresponds to photon energy of 0.24 meV. Infrared radiatian in the far region, i.e. wavelengths of about 100 μm, originate mainly from reemission of ultraviolet and visible light from stars on dust clouds. In the near region, i.e. wavelengths of about 1 μm, it is a direct radiation from the stars or a radiation shifted from other parts of the energy spectrum.
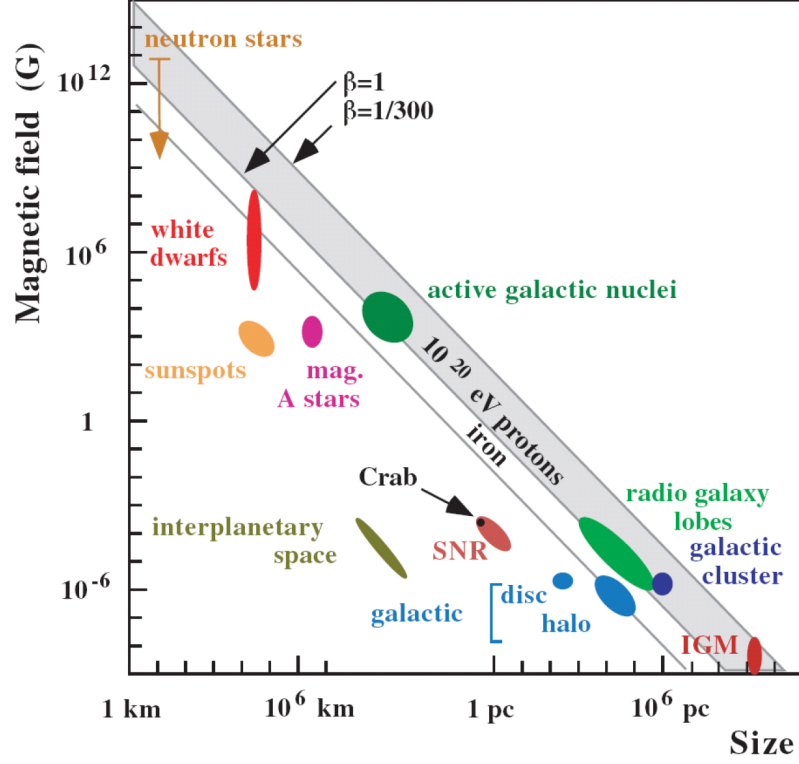
Figure 1.5: Hillas plot. Sizes and absolute values of magnetic inductions of astrophysical objects that can be sources of CRs are depicted. Objects under the line are not able to accelerate protons or iron nuclei, respectively, to the energy of 10^{20} eV. β gives characteristic velocity of scattering centres. Picture is taken from Ref.[41].

Density of the CIRB is about 2 cm^{-3}. It is about 200 times less then density of the CMB. Information comes from Ref.[15].

In 1966, a year after discovery of the CMB by Penzias and Wilson [56], Greisen [34] and independently Zatsepin and Kuzmin [72] theoretically described influence of the CMB to CR particles. Proton interactions with CMB photons are photopion productions and pair production

$$p + \gamma_{CMB} \longrightarrow \Delta^+ \longrightarrow n + \pi^+, \tag{1.15}$$
$$p + \gamma_{CMB} \longrightarrow \Delta^+ \longrightarrow p + \pi^0, \tag{1.16}$$
$$p + \gamma_{CMB} \longrightarrow p + e^+ + e^-. \tag{1.17}$$

Nuclei with mass number A photodisintegrate

$$A + \gamma_{CMB} \longrightarrow (A-1) + n, \tag{1.18}$$
$$A + \gamma_{CMB} \longrightarrow (A-2) + 2n \tag{1.19}$$

and high–energy photons are also subjets of pair production on CMB photons

$$\gamma + \gamma_{CMB} \longrightarrow e^+ + e^-. \tag{1.20}$$

If neutron is produced in one of these processes, it decays

$$n \longrightarrow p + e^- + \tilde{\nu}. \tag{1.21}$$

9
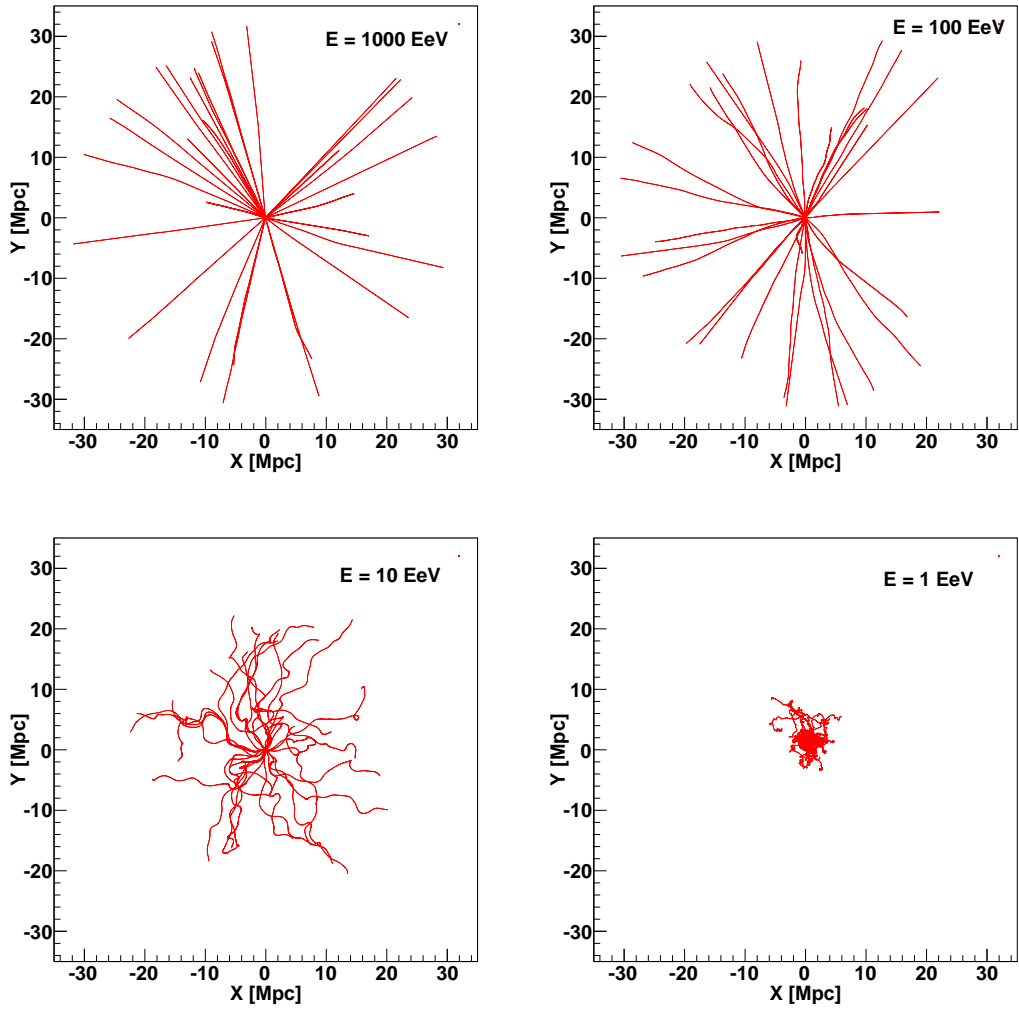
Figure 1.6: Plane projections of trajectories of 30 protons with primary energies 10^{18}, 10^{19}, 10^{20} and 10^{21} eV. Magnetic field is random with the mean magnetic induction of 10 nG in boxes with edges of 1 Mpc. Picture is taken from Ref.[54].

Because of these interactions primary CR particles lose energy. If one considers mean free paths of the processes shown in Fig.1.7, it is possible to construct statistical dependence of CR particles energies with respect to the travelled distance. This dependence is depicted in Fig.1.8.

The fact that energy of particles with arbitrary primary energy falls below the threshold for photopion production (approximately $5 \cdot 10^{19}$ eV) after propagating over certain distance is called Geiser–Zatsepin–Kuzmin cutoff (GZK).

1.5 Extensive Air Showers

When primary very energetic CR particles hit the Earth's atmosphere, secondary EASs are produced. Study of EASs is the most important source of our knowledge about the most energetic CRs. In EASs, three components can be distinguished
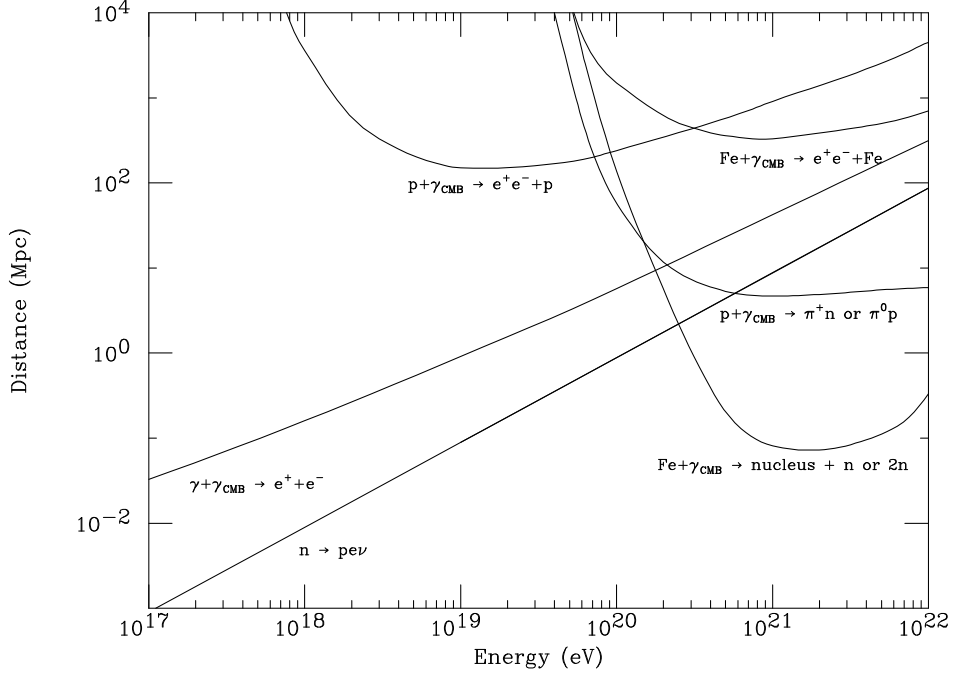
Figure 1.7: Interactions of primary particles with the CMB. Curves marked by "p + γ_{CMB} → e⁺e⁻ + p" and "Fe + γ_{CMB} → e⁺e⁻ + Fe" are energy loss lengths, i.e. the distance for which the proton or Fe nucleus loses $1/e$ of its energy due to pair production. The curve marked by "p + γ_{CMB} → π^+n or π^0p" is the mean free path for photopion production of a proton on the CMB. The curve marked "Fe + γ_{CMB} → nucleus + n or 2n" is the mean free path for a photodisintegration and "$\gamma + \gamma_{\mathrm{CMB}}$ → e⁺e⁻" is the mean free path for the interaction of a high–energy photon with the CMB. Added for reference is the mean decay length for a neutron indicated by "$n \to pe\nu$". Picture is taken from Ref.[25].

- Electromagnetic (EM) component – This is the component of the EAS in which photons, electrons and positrons are formed. The numbers of photons and electrons are very closely linked. The vast majority of the particles arriving at ground level are photons, followed closely by electrons. The latter component deposits majority of the energy deposited to the atmosphere by EAS.

- Meson component – Consists of a wide variety of exotic particles, but the most important ones are the muons which are the third to most abundant particles arriving at the ground. Muons come from π^+, π^-, K^+ and K^- decays. This component induces the electromagnetic component through decays of muons.

- Nucleonic component – Consists of remnants of smashed air molecules and atoms, protons and neutrons. Apart from neutrons, these are the least abundant particles reaching the ground.

Schema of the EAS components is shown in Fig.1.9.
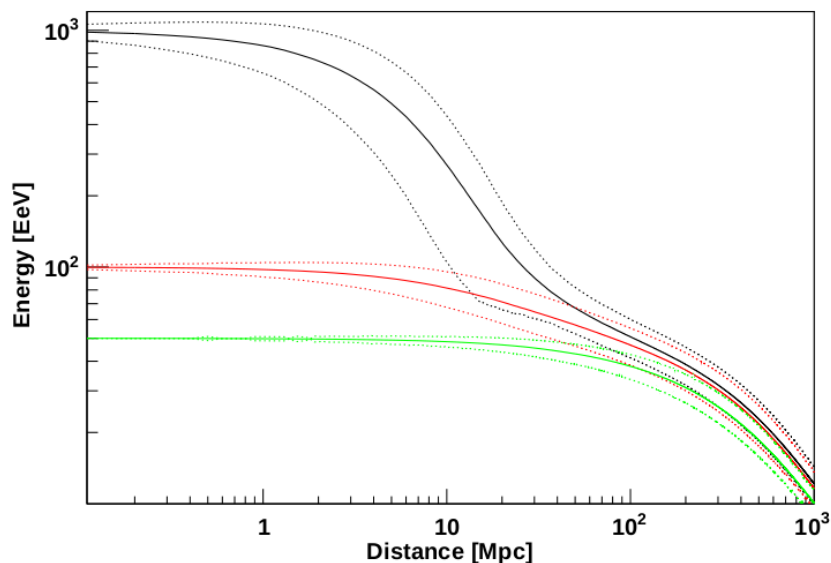
Figure 1.8: The GZK effect. Dependence of the primary CR protons energy on the distance from the source. Primary energies of protons are $5 \cdot 10^{19}$, 10^{20} and 10^{21} eV. Energy losses by interactions with CMB as well as photopion production on CIRB and redshift are accounted for. Full curve gives statistical mean value of the particles energy and dotted curve is its standard deviation. Picture is taken from Ref.[54].

For a description of the depth of the EAS it is usually introduced atmospheric depth X at altitude h as

$$X(h) = \int_h^\infty \frac{\rho(l)}{\cos\theta} \mathrm{d}l, \qquad (1.22)$$

where $\rho(l)$ is the air density at altitude l and θ is a zenith angle of the shower axis.

1.5.1 Heitler model

Basic approach to EAS description is the Heitler model proposed in Ref.[39]. It describes the EM part of the shower. The idea of the model is shown in Fig.1.10. In each generation, all γ's are converted to e^+e^- pair and all e^+, e^- species radiate γ. Characteristic length of these interactions is the radiation length in air λ of about 37 g cm^{-2}. After $n = \frac{X}{\lambda}$ generations, there are 2^n particles in the shower. Energy of secondary particles is given by

$$E(X) = \frac{E_0}{2^{\frac{X}{\lambda}}}, \qquad (1.23)$$

where E_0 is the energy of the primary particle. The shower ends when $E(X) = E_c \approx 80$ MeV. The total number of generations in the shower is given by

$$n_c = \frac{\log\left(\frac{E_0}{E_c}\right)}{\log 2}. \qquad (1.24)$$
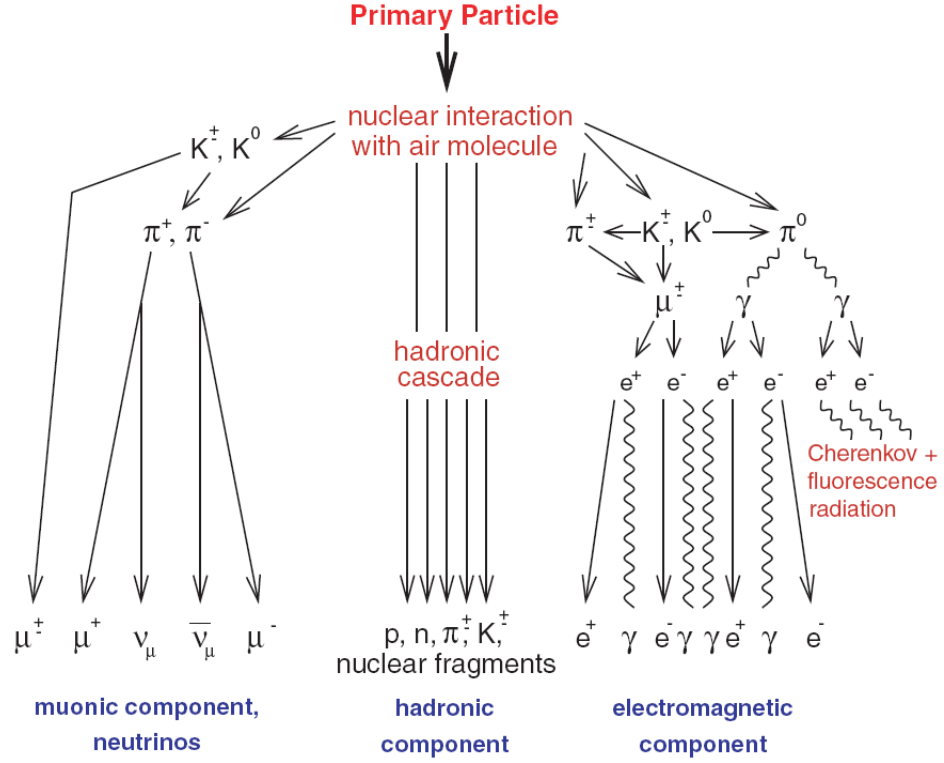
Figure 1.9: Components of the EAS induced by primary CR particle. Picture is taken from Ref.[35].

In Heitler model, atmospheric depth of the shower maximum is given by

$$X_{\text{max}} = \lambda n_c = \frac{\lambda}{\log 2} \log \left(\frac{E_0}{E_c} \right), \tag{1.25}$$

and the total number of EM particles at the shower maximum is given by

$$N_{\text{max}} = \frac{E_0}{E_c}. \tag{1.26}$$

Generalization of the Heitler model for the meson EAS component was proposed by Matthews in Ref.[49]. The idea of the model is shown in Fig.1.11. It is possible to estimate the number of muons in this model. After n generations, the number of muons is given by

$$N_\mu = (n_{\text{ch}})^n. \tag{1.27}$$

The number of pions in a generation is $n_{\text{tot}} = \frac{3}{2} n_{\text{ch}}$. Energy of pions after n generations is given by

$$E_\pi = \frac{E_0}{(n_{\text{tot}})^n}. \tag{1.28}$$

The shower ends when $E_\pi = E_{\text{dec}} \approx 20$ GeV. The total number of generations in the shower is given by

$$n_{c-\mu} = \frac{\log \frac{E_0}{E_{\text{dec}}}}{\log n_{\text{tot}}}. \tag{1.29}$$

13
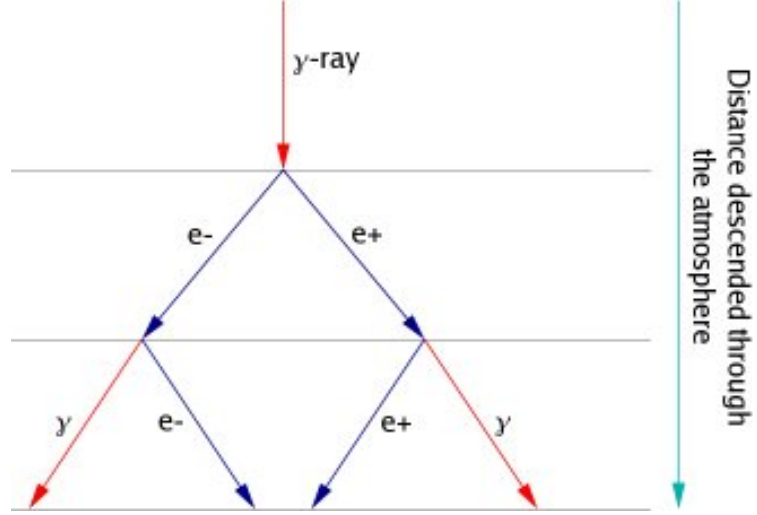
Figure 1.10: Heitler model for EM component. In each generation all γ's are converted to e^+e^- pair and all e^+, e^- particles radiate γ.

From Eqs.(1.27) and (1.29) the total number of muons in the shower is given by

$$N_\mu = (n_{\text{ch}})^{\frac{\log \frac{E_0}{E_{\text{dec}}}}{\log n_{\text{tot}}}}$$

$$\log N_\mu \log n_{\text{tot}} = \log n_{\text{ch}} \log \frac{E_0}{E_{\text{dec}}}$$

$$N_\mu = \left(\frac{E_0}{E_{\text{dec}}}\right)^{\frac{\log n_{\text{ch}}}{\log n_{\text{tot}}}} = \left(\frac{E_0}{E_{\text{dec}}}\right)^\alpha, \tag{1.30}$$

where $\alpha \approx 0.82..0.95$ is the parameter that depends on the number of pions in interactions.

For description of the EAS induced by nuclei with mass number A, the superposition model is used. It assumes that shower generated by nuclei with energy E_0 acts approximately as superposition of A independent showers with energies $E = \frac{E_0}{A}$. In this model, the depth of shower maximum X_{max} for the nuclei is given by

$$X_{\text{max}}^A = \lambda n_c = \frac{\lambda}{\log 2} \log \left(\frac{E_0}{AE_c}\right), \tag{1.31}$$

and the total number of EM particles at the shower maximum is

$$N_{\text{max}}^A = A\frac{E_0}{AE_c} = \frac{E_0}{E_c}. \tag{1.32}$$

It turns out that the number of muons is

$$N_\mu^A = A\left(\frac{E_0}{AE_{\text{dec}}}\right)^\alpha = A^{1-\alpha}N_\mu. \tag{1.33}$$

From Eqs.(1.31) and (1.33) the dependence of X_{max} and N_μ on the mass composition of the CR primary is evident. On the basis of these models, X_{max} dependence on energy E and mass number A can be written as

$$X_{\text{max}} = \alpha(\log E - \log A) + \beta, \tag{1.34}$$

14
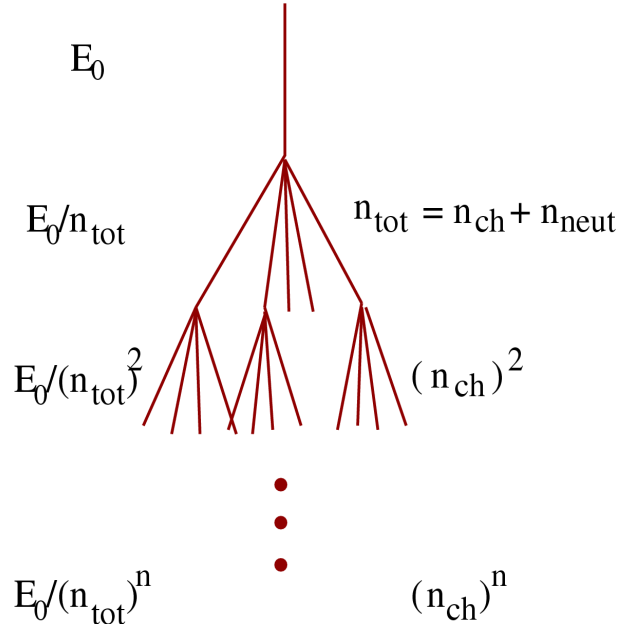
Figure 1.11: Schematic view of generalized Heitler model for meson component.

where α and β enclose the dependence on the properties of the hadronic inter-
action model and the point of the first interaction. For the analysis of the mass
composition gained from X_{max} distributions, a quantity called elongation rate is
defined as

$$D = \frac{\mathrm{d}\,\langle X_{\mathrm{max}}\rangle}{\mathrm{d}\log E}. \tag{1.35}$$

More detailed descriptions of EASs are possible through Monte Carlo simula-
tions summarized in Chapter 3.

2. Detection Techniques and the Pierre Auger Observatory

Extensive air shower (EAS) can be measured by several techniques. Some of these techniques, as are implemented at the Pierre Auger Observatory, are briefly described in this Chapter. The most important methods are the surface detector (SD) array technique and the measurement of the air fluorescence light generated by showers. Fluorescence light is collected by fluorescence detector (FD). Both of these methods were used in many detectors in the past, but The Pierre Auger Observatory is the first hybrid detector capable of measuring in both FD and SD regimes. The For history overview see Section 1.1.

In the last part of the Chapter, the energy calibration of the Pierre Auger Observatory detector is described. The possibility of measurement in FD+SD regime gives opportunity to calibrate SD array through FD telescope measurement.

The Pierre Auger Observatory is located near the city of Malargüe in Argentina. Altitude of the observatory is about 1400 m a.s.l. Map of the Pierre Auger Observatory is shown in Fig.2.1. Four FD stations and SD array are depicted.

2.1 Surface Detector Array

There are several possibilities of creating SD array. Individual SD units can consist of Geiger–Muller counters, scintillators or water Čerenkov tanks. At the Pierre Auger Observatory, water Čerenkov tanks are used. Scheme of the tank is depicted in Fig.2.2. Tanks have cylindrical shape and they are filled by 12 m^3 of pure demineralized water. Čerenkov radiation is produced when charged particles with velocities higher then the speed of light in water travel through the water in the tanks. Emitted light is reflected by Tyvek liner to the three photomultipliers. Digitalized data are transmitted through communication antennae to the central data acquisition system. Energy for tank operation is taken from batteries charged by solar panels.

SD array consists of 1600 tanks and covers an area over 3000 km^2. Tanks are formed into a regular triangular grid with a spacing of 1500 m. The spacing is chosen according to the aim of measuring the EASs initiated by UHECRs [3].

From SD array measurements, the EAS energies and the directions of the shower axes can be reconstructed. Detailed description of the SD reconstruction can be found in Section 4.1.

2.2 Detection of Fluorescence Radiation

Another main technique used at the Pierre Auger Observatory is a measurement of air fluorescence. As an EAS develops in the atmosphere, it dissipates much of its energy by exciting and ionizing air molecules along its path. Excited nitrogen molecules fluoresce. They produce near ultraviolet radiation with approximately 80% of the light emitted between 300 and 450 nm [3]. Fluorescence light is emitted isotropically with an intensity proportional to the number
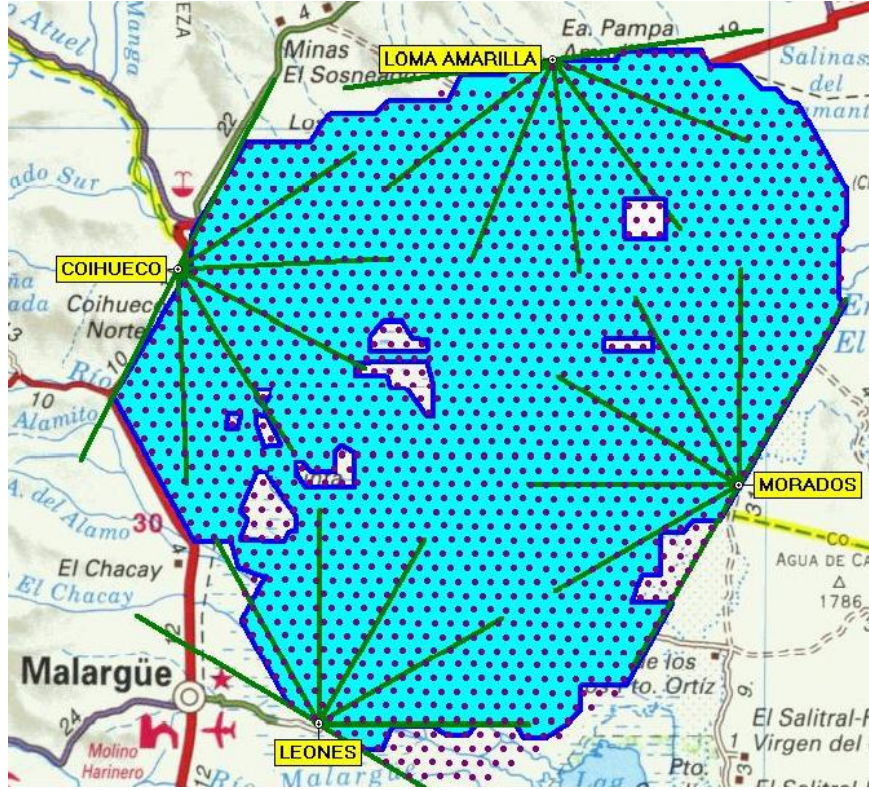
Figure 2.1: Map of the Pierre Auger Observatory. Four FD stations and SD array are depicted. Picture is taken from Ref.[69].

of charged particles in the shower. Electrons and positrons so dominate in the shower in the way that the number of charged particles can be substituted by the number of electrons and positrons in the shower.

In addition to fluorescence light, showers produce a large number of Čerenkov photons. The Čerenkov emission angle in the atmosphere is about 1°, varying with altitude [3]. It is necessary to estimate the number of Čerenkov photons in order to subtract its contribution to the observed signal.

At the Pierre Auger Observatory, 24 FD telescopes are located in four FD stations. Names of the FD stations are Los Leones, Los Morados, Loma Amarilla and Coihueco. Additional 3 FD telescopes operates as the High Elevation Auger Telescopes (HEAT) at Coihueco site. Four FD stations are located on the hills at the edge of the SD array as is shown in Fig.2.1. Schematic view of the FD station is depicted in Fig.2.3. A site consists of 6 telescopes. Each telescope covers an angular area of 30° azimuthally and 28.6° vertically. Each camera consists of 440 hexagonal phototubes, thus each phototube pixel fills the view angle of about $1.5° \times 1.5°$. Geometrical configuration of the FD telescope is shown in Fig.2.4.

Measurement of the fluorescence light allows to specify longitudinal profiles of the showers, i.e. the atmospheric depth of the shower maximum X_{max}. EAS energies and directions of the shower axes can be determined as well. Descriptions of the Hybrid reconstruction and the Multiple–eye reconstruction are summarized in Sections 4.3 and 4.4, respectively.
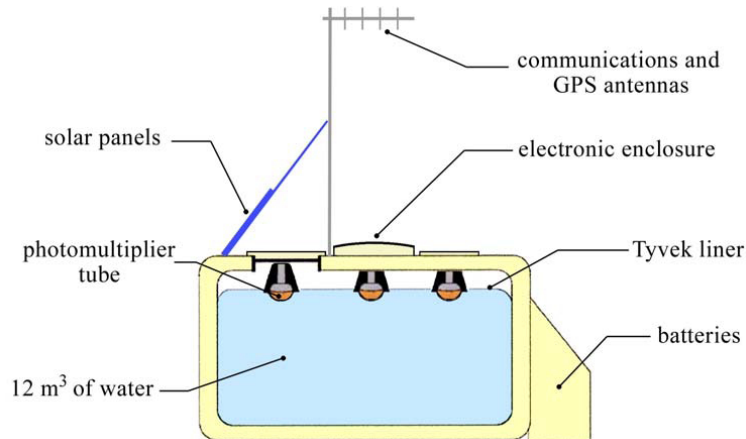
Figure 2.2: Water Čerenkov tank used at the Pierre Auger Observatory. Photomultipliers take Čerenkov radiation reflected by Tyvek liner. Solar panels, GPS and communication antenna and batteries are shown. Picture is taken from Ref.[4].

2.3 Other detection techniques

Besides the main SD array and four FD stations, the Auger Muons and Infill for the Ground Array (AMIGA) [29] and the High Elevation Auger Telescopes (HEAT) [50] operate. The principle of the measurement is the same as for SD array and FD telescopes, respectively. The Infill array consists of similar SD tanks as the regular array but with spacing of 750 m. The HEAT is formed by three FD telescopes. They are dedicated to measure lower EAS energy region down to 10^{17} eV. At the lower energies, data taken by the Pierre Auger Observatory can be compared to data measured by other experiments.

Other different experimental methods are tested at the Pierre Auger Observatory as well. EAS radio emission in MHz region and microwave emission in GHz region are studied. The Auger Engineering Radio Array (AERA) studies the MHz emission and the Air–shower Microwave Bremsstrahlung Experimental Radiometer (AMBER), the Extensive Air Shower Identification using Electron Radiometer (EASIER) and the Microwave Detection of Air Showers (MIDAS) experiments study the microwave emission. For details of the radio and microwave detection see Ref.[61] and [11], respectively.

2.4 Energy Calibration

The possibility of EAS measuring by two different methods allows to perform energy calibration of the SD array through FD telescopes.

To determine the EAS energy from FD measurement it is needed to obtain a relation between counts from individual phototubes of fluorescence camera and light flux. For this purpose, three types of calibration take place at the Pierre Auger Observatory – absolute calibration, relative calibration and calibration using laser shots in the atmosphere. Absolute calibration uses a portable source of homogeneous light flux which is mounted on the FD telescopes. This type of
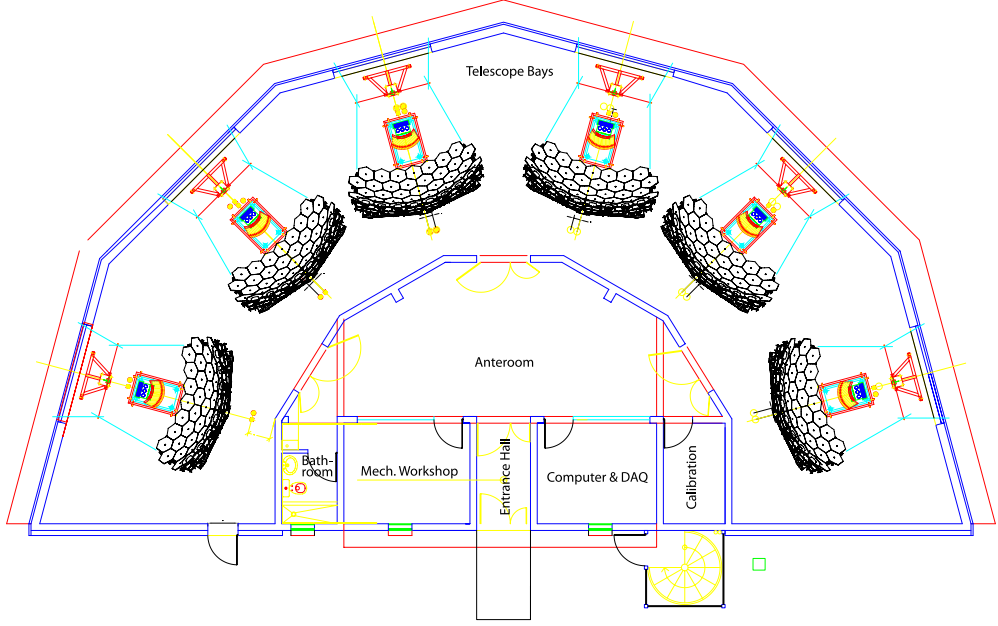
Figure 2.3: Scheme of the FD station. Positions of six FD telescopes are shown. Picture is taken from Ref.[8].

calibration is performed several times per year. The overall absolute calibration uncertainty is about 9% [70]. Calibration using laser shots is done from Central Laser Facility (CLF) station located in the centre of the SD array. A nitrogen laser with wavelength of 370 nm provides 100 mJ pulses into the atmosphere. Scattered fluorescence light is then measured by FD cameras. This procedure is performed during the whole measurement of FD telescopes. Before and after each night of operation, a series of relative calibration measurements is performed. It is used to monitor detector response between absolute calibrations.

Energy calibration of the SD array can be obtained either by simulations or by FD energy measurement. At the Pierre Auger Observatory, the SD energy calibration is obtained by direct FD measurement. This method does not depend on particular hadronic interaction models used in simulations. FD measurements provide information about energy deposited in the air. Thus the correction for a fraction of shower energy carried away by muons and neutrinos must be performed. The correction factor is obtained as an average missing energy from simulated showers initiated by proton and iron at equal rate. For energy of 10^{19} eV the fraction of invisible energy is averaged to about 10% [70].

After the proper FD energy calibration the EAS SD parameter S38 is related to the FD energy E_{FD} as [5]

$$S38 = a \cdot E_{\mathrm{FD}}^{b}. \tag{2.1}$$

Parameter S38 is the SD array signal recalculated to zenith angle $\theta = 38°$ by the Constant Intensity Cut (CIC) method described in Ref.[70]. Parameters a and b are obtained from the fit shown in Fig.2.5. a and b are determined as [5]

$$
\begin{aligned}
a &= (1.51 \pm 0.06(\text{stat}) \pm 0.12(\text{syst})) \cdot 10^{17} \text{ eV}, \\
b &= 1.07 \pm 0.01(\text{stat}) \pm 0.04(\text{syst}).
\end{aligned}
$$

19

Figure 2.4: Geometrical parameters of the FD telescopes. Picture is taken from Ref.[8].

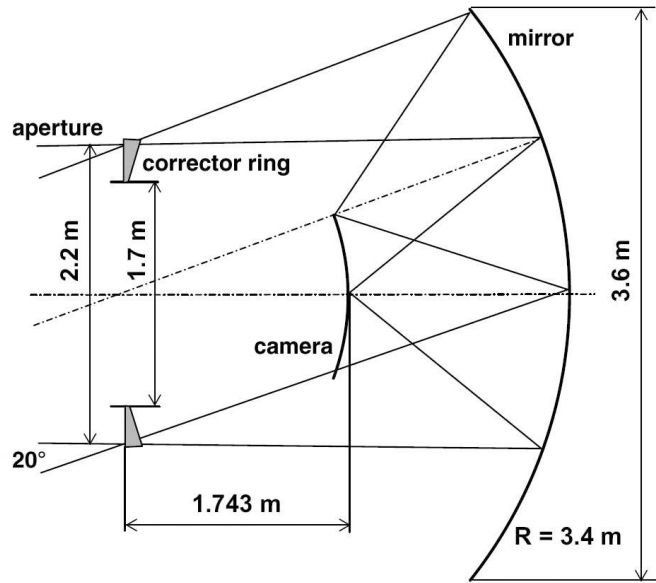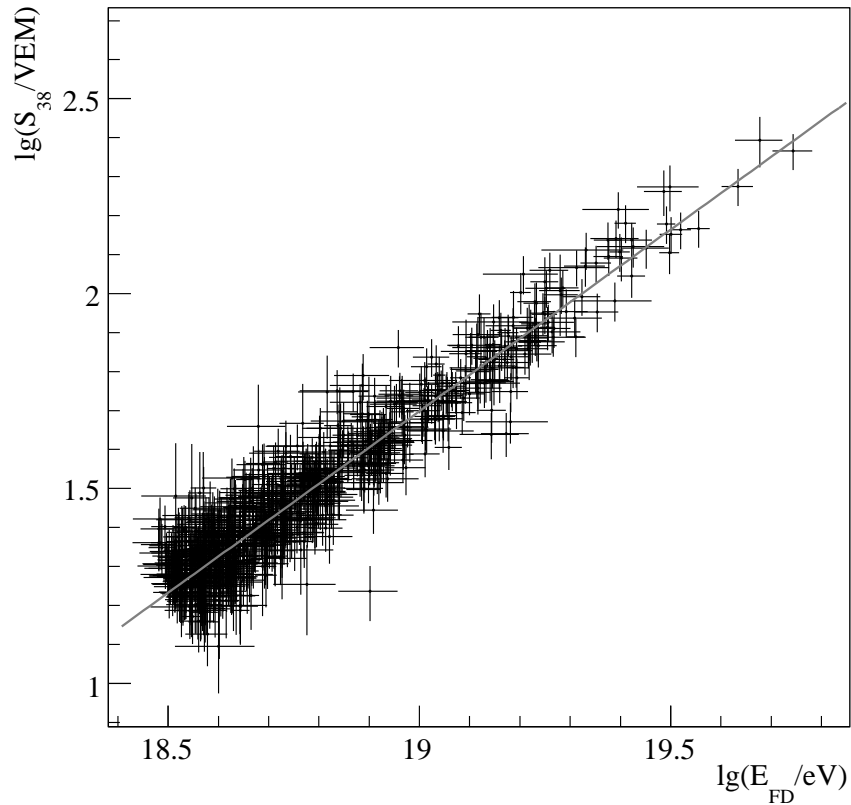Figure 2.5: SD energy calibration by the FD energy E_{FD}. Parameter S38 is the SD array signal recalculated to zenith angle $\theta = 38°$ by the Constant Intensity Cut (CIC) method. Picture is taken from Ref.[5].

3. Extensive Air Shower Simulations

Basic analytical approach to an extensive air shower development caused by cosmic ray (CR) particles is represented by the Heitler model and can be found in Section 1.5. This is a very rough description of the showers and from these calculations only qualitative results can by determined. If more precise descriptions of the showers are necessary, one have to use more complex models incorporated in some Monte Carlo simulation program. The most widely used tool for the extensive air shower (EAS) modelling is the CORSIKA program described in this chapter.

3.1 CORSIKA : A Monte Carlo Simulation Program

CORSIKA is a program for detailed EAS simulations initiated by high energy cosmic ray particles. The name CORSIKA stands for Cosmic Ray Simulation for KASCADE. It was developed for simulations for the KASCADE experiment at Karlsruhe, Germany. For reference on KASCADE, see Ref.[13].

Many particles such as protons, light nuclei up to iron, and photons may be treated as primary CR particles up to an energy above 10^{20} eV. These particles are tracked through the atmosphere until they undergo interactions with air nuclei or decay. The program gives type, energy, location, momentum and arrival times for each particle at up to 10 observation levels. In extension, the program gives longitudinal distributions of particles in EASs and optionally tracks of the individual particles in the atmosphere.

For EAS simulations initiated by very high energy particles ($E_0 > 10^{16}$) the number of simulated particles in EASs is extreme, above 10^{10}. Computing times become excessively large. Solution of this problem was proposed by M. Hillas in 1997, see Ref.[40]. He proposed the so called thinning algorithm. All secondary particles with energies E below a certain fraction of the primary energy E_0, the so called thinning level $\varepsilon_{th} = \frac{E_{\mathrm{th}}}{E_0}$, are subject to this procedure. All particles with energy fractions greater than ε_{th} are followed in detail, but if the energy sum of all j particles produced in a certain interaction falls below the thinning energy E_{th}

$$\sum_j E_j < E_{\mathrm{th}} = \varepsilon_{\mathrm{th}} E_0 \qquad (3.1)$$

only one particle is followed. This surviving $i-$th particle is selected randomly according to its energy E_i with the probability p_i

$$p_i = \frac{E_i}{\sum_j E_j}. \qquad (3.2)$$

All other particles are discarded. In order to conserve energy, an appropriate weight $w_i = \frac{1}{p_i}$ is assigned to the surviving $i-$th particle. If only in part the

Table 3.1: Energy cutoffs used in this thesis.

	hadrons	$\mu^\pm$	$e^\pm$	γ
Energy cutoff [GeV]	0.3	0.3	0.003	0.003

energy of secondary particles falls below the thinning level, the corresponding $i-$th particle survives with a probability p_i given by

$$p_i = \frac{E_i}{\varepsilon_{\text{th}} E_0} \tag{3.3}$$

and, in case of surviving, get the weight factor $w_i = \frac{1}{p_i}$. The latter procedure is also applied if the energy sum of the corresponding particles exceeds the thinning level, thus enabling more than one particle to survive. By this selection mechanism only a rather constant number of particles must be followed in the low energy EAS region instead of an exponentially growing number. Explanation of thinning can be found also in CORSIKA physics manual [36].

There is a drawback however. Only one particle (or more, depending on the energy sum of the secondaries) of the bunch of particles produced in the interaction is followed. Although secondaries with higher energies are more probable to survive, there are still secondaries, with comparable energies, which are discarded completely. Possible reactions caused by secondaries which are not followed in detail are not taken into account in CORSIKA. Conservation of momentum requires that not every particle will travel in the same direction. Thus the development of the shower depends on the momentum and energy of the surviving particle which was tracked. The accuracy of the EAS development can be consequently decreased. A thinning level of 10^{-6} is considered to be the best compromise.

Other important parameters of EAS simulations are energy cuts. Particles with energies below a certain value, the energy cutoff, are dropped from simulations. This ensures that computing times remain manageable. Energy cutoffs used in this thesis are summarized in Table 3.1.

3.1.1 Hadronic Interaction Models

Hadronic interactions are simulated within CORSIKA by several models depending on interaction energy. It is described in details in Ref.[37].

If the interaction energy is high enough, the interaction is treated by one of the models DPMJET (Dual Parton Model with JETs) [60], EPOS (Energy conserving quantum mechanical multi–scattering approach, based on Partons, Off–shell remnants and Splitting parton ladders) [58], HDPM, neXus (NEXt generation of Unified Scattering approach) [28], QGSJET (Quark Gluon String model with JETs) [42], SIBYLL [31] or VENUS (Very Energetic NUclear Scattering) [71].

The high energy models reach their limit when the energy available for generation of secondary particles drops below a certain value, then the low energy models are used. Implemented low energy hadronic interaction models in CORSIKA are GHEISHA (Gamma Hadron Electron Interaction SHower code) [30], FLUKA (FLUctuating KAscade) [17] and UrQMD (Ultra–relativistic Quantum
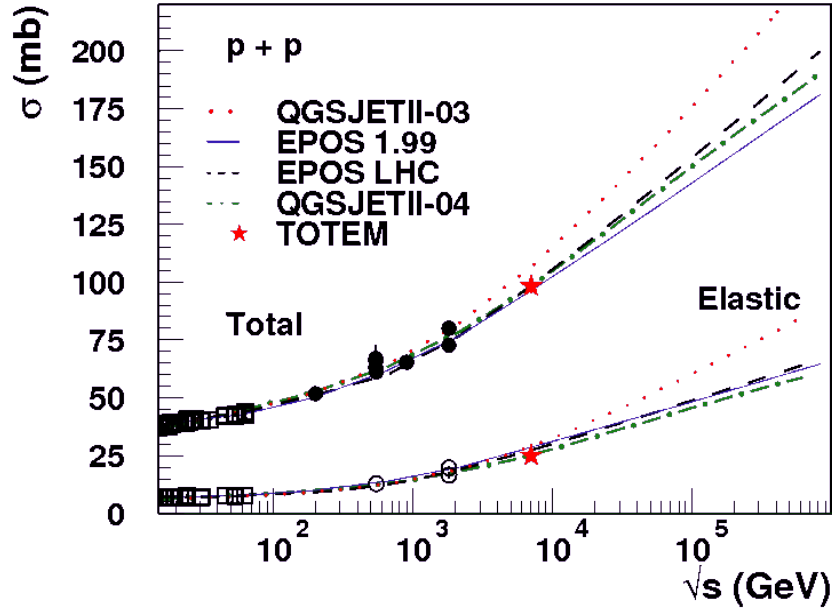
Figure 3.1: Total and elastic p–p cross section calculated with EPOS LHC (full line), QGSJETII-04 (dotted line), EPOS 1.99 (dashed line) and QGSJETII-03 (dashed-dotted line). Points are data from [24] and the stars are the LHC measurements by the TOTEM experiment [27]. Picture is taken from Ref.[57].

Molecular Dynamics) [21]. The transition energy between the high and low energy models is 80 GeV.

Many studies comparing both high and low energy models exists. There is no general recommendation for what model should be used. Parameters of the models are partly determined analytically and partly fitted on accelerators data. Predictions of different models differs as can be seen in Figs.3.2 and 3.3. An interesting fact is that none of the models can accurately describe the muon component measured at the Pierre Auger Observatory [62]. Currently, LHC data has large impact on hadronic interaction models. EPOS (version EPOS LHC) and QGSJET (version QGSJETII-04) models are updated to the LHC data, see Ref.[57] and cross section predictions in Fig.3.1. For reference on hadronic models comparisons see for example Refs.[66], [38], [55].

Brief description of included hadronic interaction models in CORSIKA can be found in CORSIKA User's Guide [37].

3.2 Simulations and Data Analysis

In this section I will present my own simulations performed using CORSIKA program version 6990. I chose QGSJET01 as the high energy interaction model and GHEISHA as the low energy interaction model. I used a thinning level of $5 \cdot 10^{-5}$ to reduce computing time. Energy cutoffs are shown in Table 3.1. Local geomagnetic field at the Pierre Auger Observatory site[1] was set in CORSIKA.

----

[1] Horizontal component to the north : 19.6 μT, vertical component downwards : -14.3 μT.
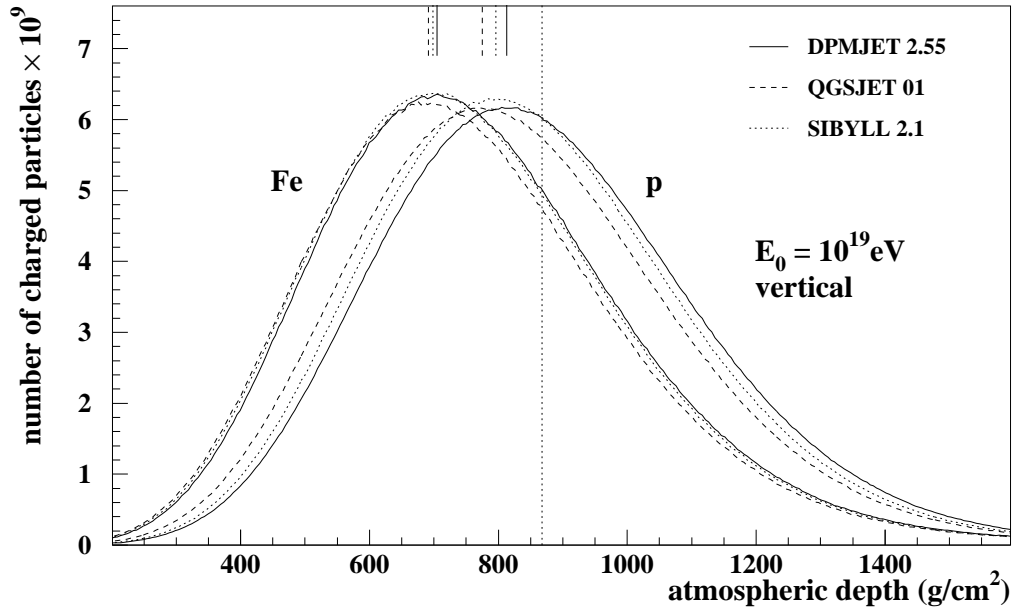
Figure 3.2: Longitudinal development of charged particle number in the vertical shower generated by a CR particle with initial energy $E_0 = 10^{19}$ eV. The vertical dotted line indicates the vertical depth of the Pierre Auger Observatory in Argentina. Picture is taken from Ref.[66].
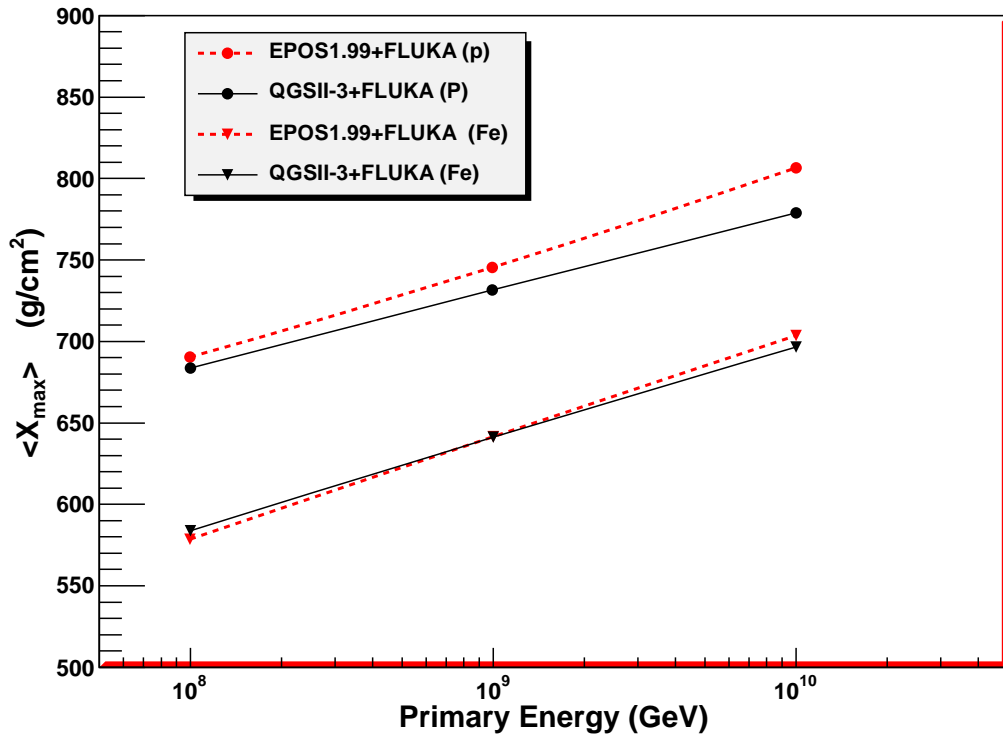
Figure 3.3: Average X_{max} vs. log of primary energy for proton and iron induced showers. EPOS1.99 and QGSJETII–3 with FLUKA were used. Picture is taken from Ref.[38].

Table 3.2: The numbers of particles in CR showers at observation level 1400 m a.s.l. Caused by primaries with energy of $E_0 = 10^{19}$ eV.

θ [°]	hadrons	muons	EM
0°	81 516	793 743	11 546 775
50°	4 610	471 773	128 751

CORSIKA can provide tracks of individual particles. For illustration of this feature, tracks of the individual particles from side and top views are shown in Figs.3.4 and 3.5, respectively. Energy of the primary particle is 10^{16} eV, zenith angle $\theta = 0°$. Narrow hadronic component (blue), wider electromagnetic[2] (red) and muonic (green) components are shown. Tracks of the particles are traced in the cylinder with the radius of 8 km.

Longitudinal EAS profiles can be well described by the Gaisser–Hillas function [33]

$$N(X) = N_{\max} \left(\frac{X - X_0}{X_{\max} - X_0} \right)^{\frac{X_{\max} - X_0}{\lambda}} e^{\frac{X_{\max} - X}{\lambda}}, \qquad (3.4)$$

where $N(X)$ is the number of particles in the EAS at atmospheric depth X, $X_{\max}$ is the atmospheric depth of the shower maximum, $N_{\max}$ is the normalization factor and X_0 and λ are other parameters obtained by fit. Good agreements of the fits of longitudinal profiles by Gaisser–Hillas functions are shown in Fig.3.6 for proton and iron initiated EASs at energy of $5 \cdot 10^{19}$ eV.

In CORSIKA, up to 10 observation levels can be set. In the simulation below, one observation level at the altitude of the Pierre Auger Observatory[3] was set. Impact points of all particles at the observation level are shown in Figs.3.7 and 3.8 for zenith angles 0° and 50°, respectively. Graphs are centred to the intersection of the shower axis and the observation level. Energy of the primary particle is 10^{19} eV. Blue dots are for hadrons, red dots for EM particles and green dots are for muons, respectively. The numbers of particles that reach the observation level is shown in Table 3.2. For $\theta = 0°$, the area hit by muons is almost the same as the area hit by EM component. The number of EM particles is 15 times bigger than number of muons. For $\theta = 50°$, the area hit by muons is larger and the number of muons is 4 times bigger. For large zenith angles, the muonic component dominates.

In Section 1.5, dependence of $X_{\max}$ distributions on the primary particle type is described. Particularly $\langle X_{\max} \rangle$ and $\mathrm{RMS}(X_{\max})$ can be used for study of chemical composition. I simulated 100 events for proton, iron and oxygen at energies 10^{18}, $5 \cdot 10^{18}$, 10^{19} and $5 \cdot 10^{19}$ eV. For each energy I determined $\langle X_{\max} \rangle$ and $\mathrm{RMS}(X_{\max})$.

Results of the simulations together with Auger hybrid data are shown in Figs.3.9 and 3.10, respectively. These results may be interpreted as heavier nuclei causing registered CR showers at higher energies, while protons seem to be responsible for data collected by the Auger detector at lower energies. Similar

---

[2] Electromagnetic (EM) means electrons, pozitrons and gammas.
[3] Altitude is 1400 m a.s.l.
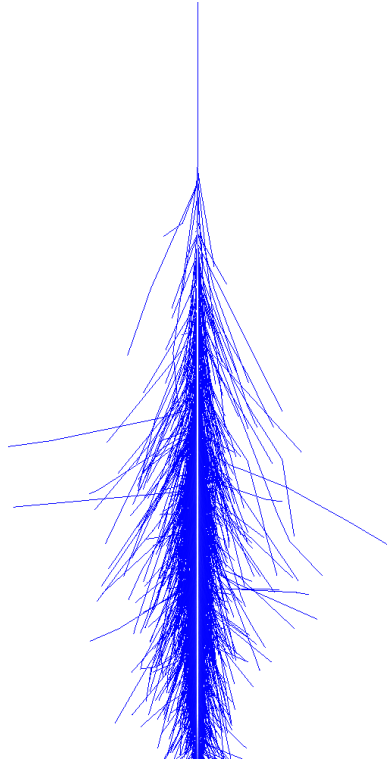
(a) Hadronic component, side view.
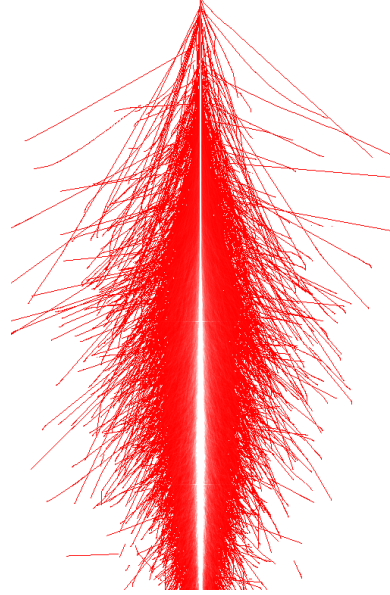
(b) EM component, side view.
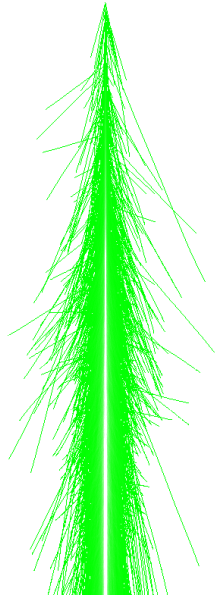
(c) Muonic component, side view.
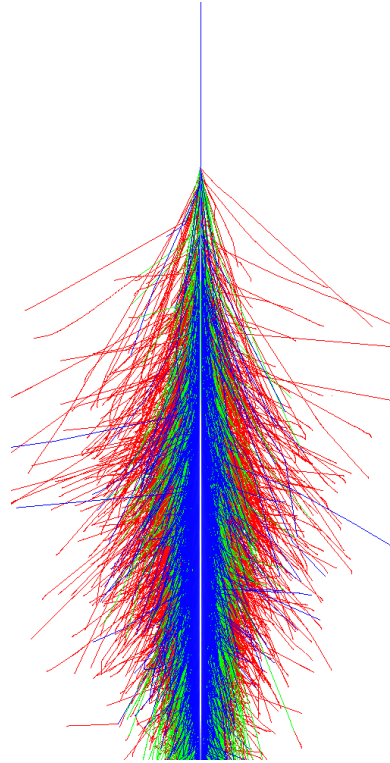
(d) All components, side view.

Figure 3.4: Tracks of the individual particles. Side views for primary CR particle with energy of $E_0 = 10^{16}$ eV are shown. Tracks of the particles are traced in the cylinder with the radius of 8 km. Simulation ends at sea level.

(a) Hadronic component, top view.

(b) EM component, top view.

(c) Muonic component, top view.

(d) All components, top view.
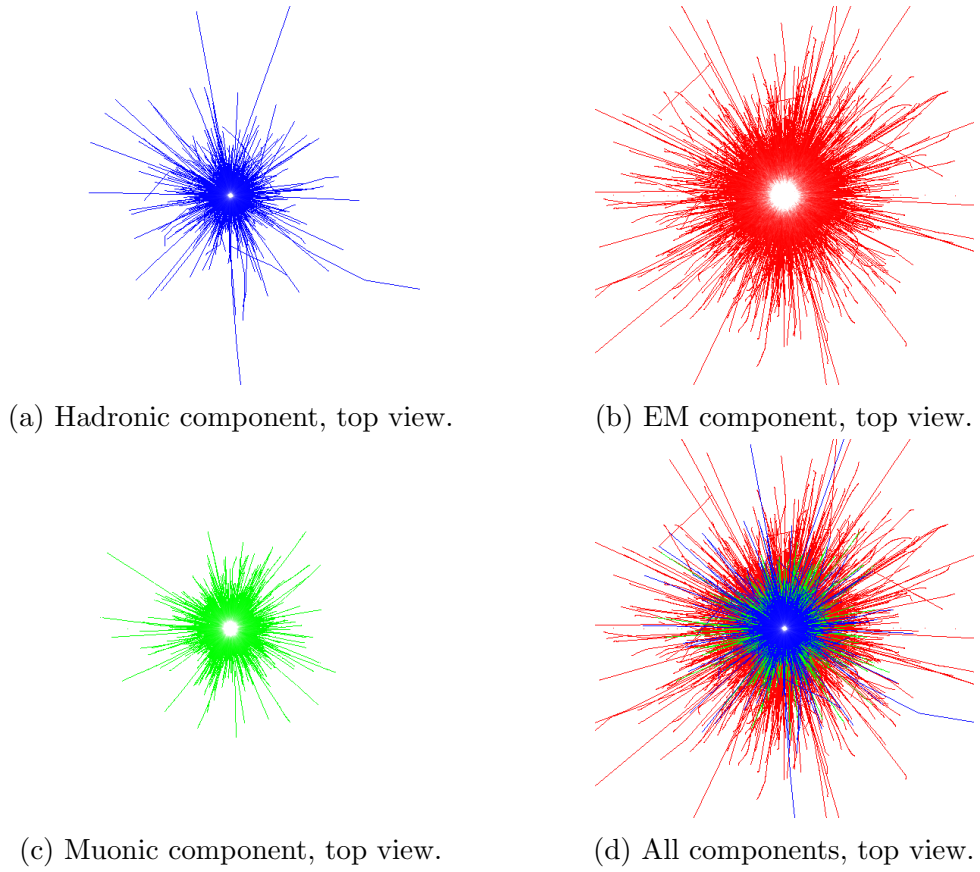
Figure 3.5: Tracks of the individual particles. Top views for primary CR particle with energy of $E_0 = 10^{16}$ eV are depicted. Tracks of the particles are traces in the cylinder with the radius of 8 km.
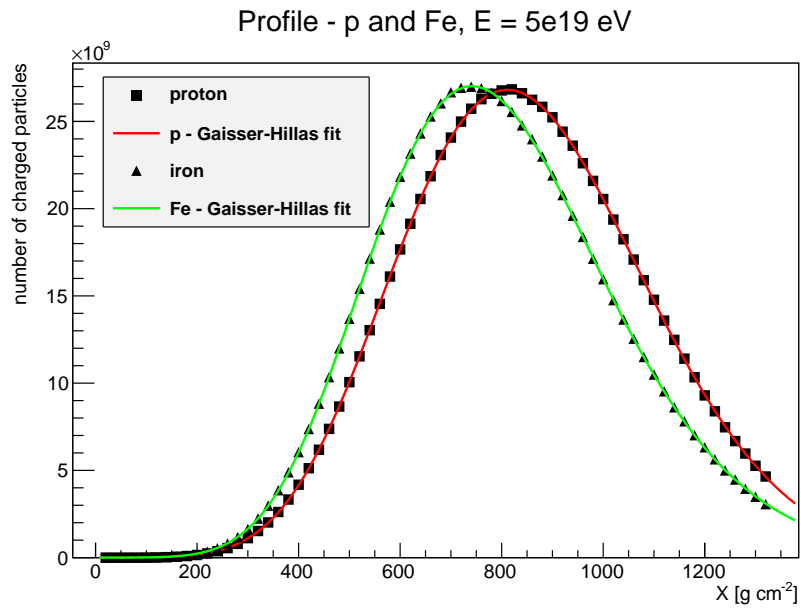
Figure 3.6: Simulated EASs induced by proton and iron primaries are fitted by Gaisser–Hillas functions.
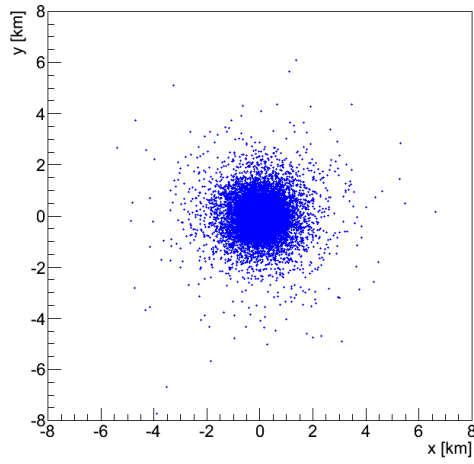
(a) Hadronic component.
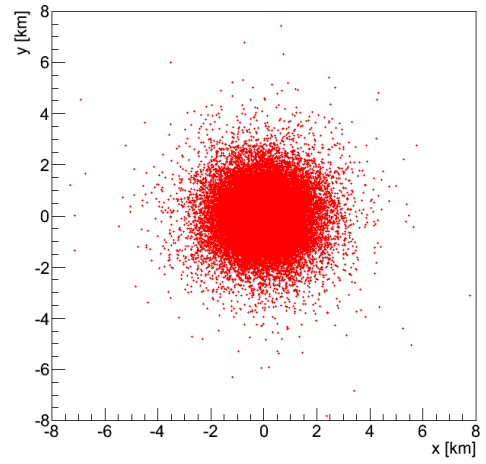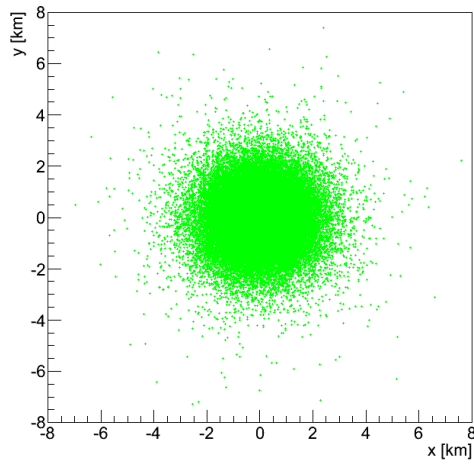
(b) EM component.
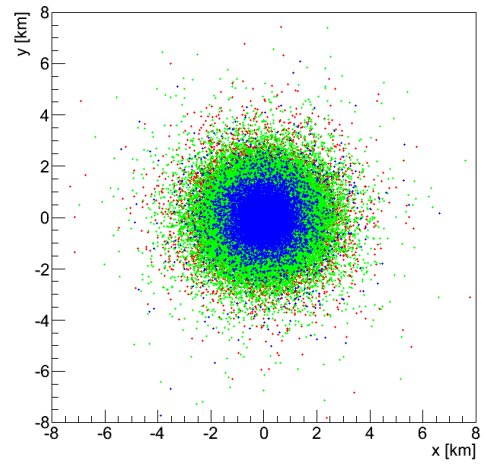
(c) Muonic component.

(d) All components.

Figure 3.7: Impact points of shower particles that reach the observation level at 1400 m a.s.l. for primary particle with energy of $E_0 = 10^{19}$ eV, zenith angle $\theta = 0°$.
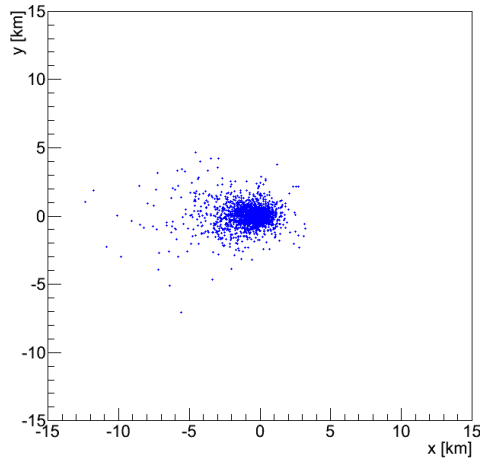
(a) Hadronic component.
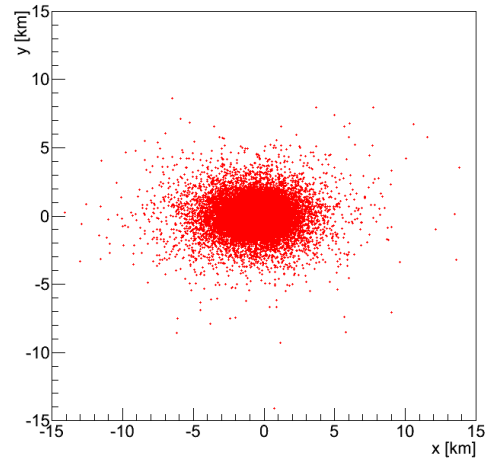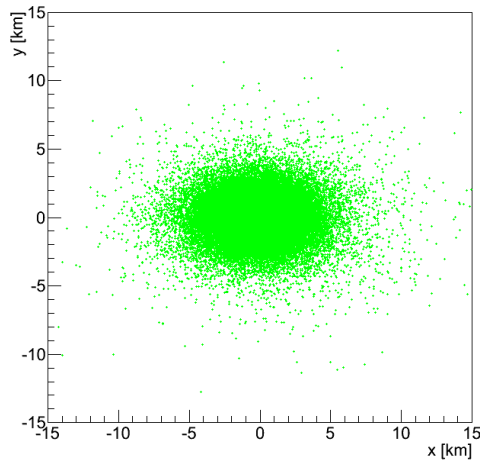
(b) EM component.

(c) Muonic component.
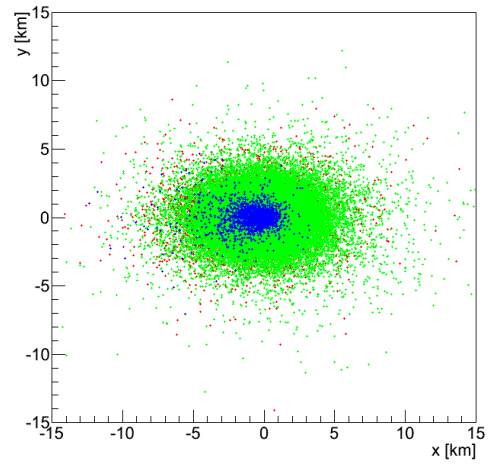
(d) All components.

Figure 3.8: Impact points of shower particles that reach the observation level at 1400 m a.s.l. for primary particle with energy of $E_0 = 10^{19}$ eV, zenith angle $\theta = 50°$.
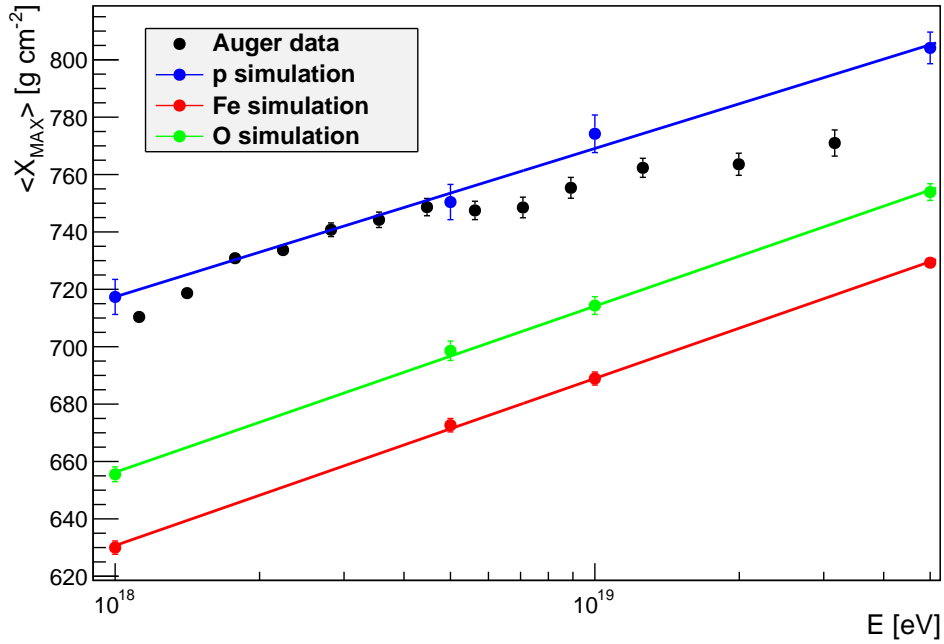
Figure 3.9: Energy dependence of $\langle X_{\max} \rangle$. Simulations of EASs generated by primary proton, iron and oxygen are compared to Auger data. Simulations for primary particle energies 10^{18}, $10^{18.5}$, 10^{19} and $10^{19.5}$ eV are performed. Colour lines show linear regression fits of simulations. Error bars correspond to statistical errors.

$X_{\max}$ analyses was presented for example in Ref.[6].

Analyses of the $X_{\max}$ distributions are very important for study of the mass composition of the CR. Quantity called elongation rate given in Eq.(1.35) can be directly measured and simulated. It is much less sensitive to the particular hadronic interaction model then the absolute location of the points in Fig.3.9. For more detailed discussion of the elongation rate measurement see for example Ref.[26].

It is necessary to point up that the evidence for heavier nuclei is measured only at the Pierre Auger Observatory. Results presented by the Telescope Array experiment in Ref.[67] are consistent with proton composition. This can be explained for example by a point source of heavier nuclei located on the southern hemisphere, because the Telescope Array is placed on the northern hemisphere.
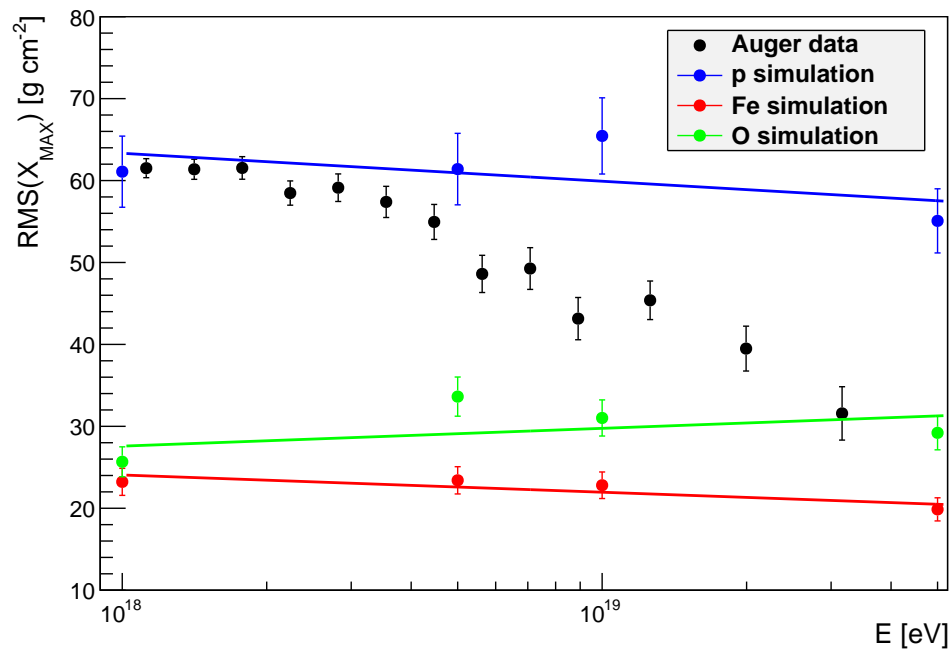
Figure 3.10: Energy dependence of RMS(X_{max}). Simulations of EASs caused by proton, iron and oxygen are compared to Auger data. For more details see caption to Fig.3.9.

4. Extensive Air Shower Reconstruction

This Chapter summarizes reconstruction methods of extensive air shower (EAS) important parameters. These parameters are vectors of the showers axes, EAS energies, longitudinal profiles and the atmospheric depths of the EAS maxima.

Detectors which can be used in EAS reconstructions are fluorescence detector (FD) and surface detector (SD).

4.1 SD Reconstruction

SD reconstruction can be used even if no FD signal is present. SD reconstruction is necessary because SD array operates all the time. FD can measure only at moonless nights which is only about 13% of the total time. This is the main importance of the SD reconstruction. On the other hand, the reconstructions of the shower axes and energies by SD are less accurate than the reconstructions by FD and there is no opportunity to measure the longitudinal EAS profiles.

SD reconstruction is based on the processing of time information from triggered tanks of the surface array combined with their total signal.

From the FADC[1] (Flash ADC) traces we get a time t_i^m which is the measured times when signal in the $i-$th station exceeds a given threshold[2]. The total signals in the $i-$th tank S_i^m is determined for all n global triggered tanks. A plane fit procedure is performed. Shower front is considered to be a plane. Neglecting differences of altitudes the signal in the $i-$th station is

$$t_i^{\mathrm{pl}} = T_0 - \frac{ux_i + vy_i}{c}, \tag{4.1}$$

where $u = \sin\theta\cos\phi$, $v = \sin\theta\sin\phi$, θ is a zenith angle, ϕ is an azimuth angle, (x_i, y_i) are coordinates of the tank and T_0 is a reference time. A minimization of residual sum of squares (RSS)

$$\rho_{\mathrm{pl}}^2 = \sum_{i=1}^{n} \frac{(t_i^m - t_i^{\mathrm{pl}})^2}{\sigma_i^2} \tag{4.2}$$

is performed to fit T_0, u and v. σ_i are systematic uncertainties of t_i^m. Iterative method to account for differences of the tanks altitudes is performed, t_i^m are replaced by $t_i^m + \delta t_i^{\mathrm{alt}}$ where

$$\delta t_i^{\mathrm{alt}} = (z_i - Z_{\mathrm{ref}})\frac{\cos\theta}{c} = (z_i - Z_{\mathrm{ref}})\frac{\sqrt{1 - u^2 - v^2}}{c}, \tag{4.3}$$

where Z_{ref} is a reference altitude[3]. This procedure converges rapidly for a small altitude differences. Finally an effect of shower front curvature is accounted for.

---

[1] Analog to digital converter of the tank signals.

[2] 4 VEM (vertical equivalent muon) at the Pierre Auger Observatory.

[3] At the Pierre Auger Observatory 1400 m a.s.l. for example.

According to simulations, the shower front can be consider as spherical with a radius of $R = R_0/\cos\theta$[4]. It corresponds to the signal delays in the $i-$th tank

$$\delta t_i^{\text{curv}} = -\frac{d_i^2}{2Rc}, \tag{4.4}$$

$$d_i^2 = (x_i - x_c)^2 + (y_i - y_c)^2 - [u(x_i - x_c) + v(y_i - y_c)]^2. \tag{4.5}$$

Here, center coordinates (x_c, y_c) assign an impact point of a shower core on the ground. This center will be further determined from a lateral shape fit. In a first step, barycenter with the weights $\sqrt{S_i}$ of the stations is chosen.

The sum of residuals

$$\rho_{\text{acc}}^2 = \sum_{i=1}^{n} \frac{(t_i^m - t_i^{\text{fit}})^2}{n - 3} \tag{4.6}$$

are calculated and if $\rho_{\text{acc}} < \rho_{\text{max}}$[5], all involved stations are accepted. Else one of the stations is excluded. If an acceptable residual is found with $n - 1$ stations, $n - 1$ stations are accepted. If the residual is not acceptable, another station from n stations is excluded and the process repeats until an acceptable residual is found. For each new configuration barycenter is computed. At each step of procedure a compacity criterion is imposed if less than 6 stations are kept – a distance of all stations to the barycenter should be less than $d_{\text{max}}^{\text{grd}}$ on ground, where $d_{\text{max}}^{\text{grd}}$ is 4 km with 4 stations, 6 km with 5 stations and less than $d_{\text{max}}^{\text{prj}}$ on projection onto the front plane for $d_{\text{max}}^{\text{prj}} = 2$ and 3 km, respectively. If this filtering is successful a 4–parameter fit with adjustable curvature is applied and iterated with a new cut

$$\rho_{\text{acc}}'^2 = \sum_{i=1}^{m} \frac{(t_i^m - t_i^{\text{fit}})^2}{n - 4} < \rho_{\text{max}}'^2 \text{[6]} \tag{4.7}$$

Principle of the adjustable curvature fit similar to the fit described above but curvature is considered as an adjustable parameter.

In the next step, a fit of lateral distribution function (LDF) is performed. In this procedure, the signal S in the tank is consider as a function of a distance from the shower axis r. The LDF depends on a zenith angle θ. If one set normalized LDF $f_{\text{LDF}}(1000\text{m}) = 1$, one can write

$$S(r) = S_{1000} f_{\text{LDF}}(r). \tag{4.8}$$

Traditionally, the NKG function is chosen [43]

$$f_{\text{LDF}}(r) = \left(\frac{r}{r_{1000}}\right)^\beta \left(\frac{r + r_{700}}{r_{1000} + r_{700}}\right)^{\beta + \gamma}. \tag{4.9}$$

Initial estimates for β and γ are given by

$$\beta_0 = 0.9\sec\theta - 3.3, \tag{4.10}$$

$$\gamma_0 = 0. \tag{4.11}$$

---

[4] R_0 is 5000 m at the Pierre Auger Observatory

[5] $\rho_{\text{max}} = 300$ ns at the Pierre Auger Observatory reconstruction.

[6] $\rho_{\text{max}}' = 200$ ns at the Pierre Auger Observatory reconstruction
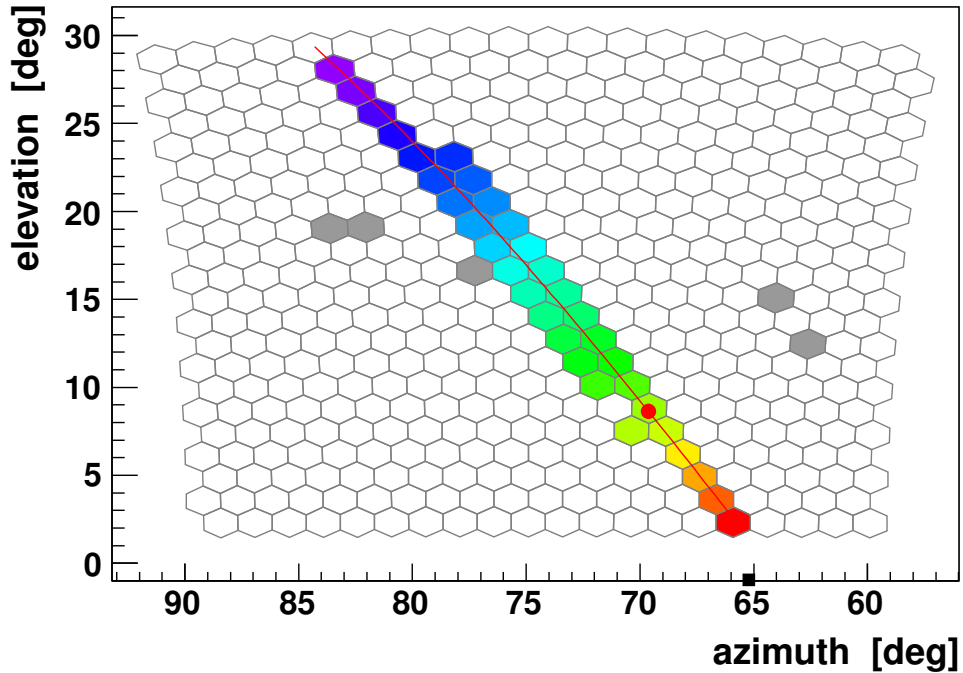
Figure 4.1: FD camera signal of event No. 200827505541 registered at Coihueco telescope by mirror 3. Red line is a reconstructed shower–detector plane, i.e. projection of the shower axis. Colour tracks correspond to the time information, grey pixels are triggered pixels with bad timing. Picture is prepared in Auger Offline EventBrowser [14].

Then a RSS fit with respect to the S_{1000}, the core position (x_c, y_c) in a local tangent plane and parameters β, γ is performed. Form of the sum of residuals is

$$\rho_S^2 = \sum_{i=1}^{m} \frac{(S_i - S(r_i))^2}{S(r_i)} + \sum_{\text{zero}-\text{signal}} S(r_i), \tag{4.12}$$

where r_i are perpendicular distances of the $i-$th tank to the core and the second term in Eq.(4.12) is an additional term for the tanks with zero signal.

Energy of the shower is reconstructed as

$$\begin{aligned} a &= 0.37 - 0.51 \sec\theta + 0.30 \sec^2\theta, \tag{4.13} \\ b &= 1.27 - 0.27 \sec\theta + 0.08 \sec^2\theta, \tag{4.14} \\ E &= a(S_{1000})^b \quad \text{[in EeV]}, \tag{4.15} \end{aligned}$$

where a and b are obtained from calibration, see Section 2.4.

4.2   Monocular FD Reconstruction

If a FD signal is detected, the basic reconstruction mechanism is a monocular time fit. The most of the fluorescent light is produced close to the shower axis. Thus the shower axis is visible as a line of the pixels in FD camera, see Fig.4.5.
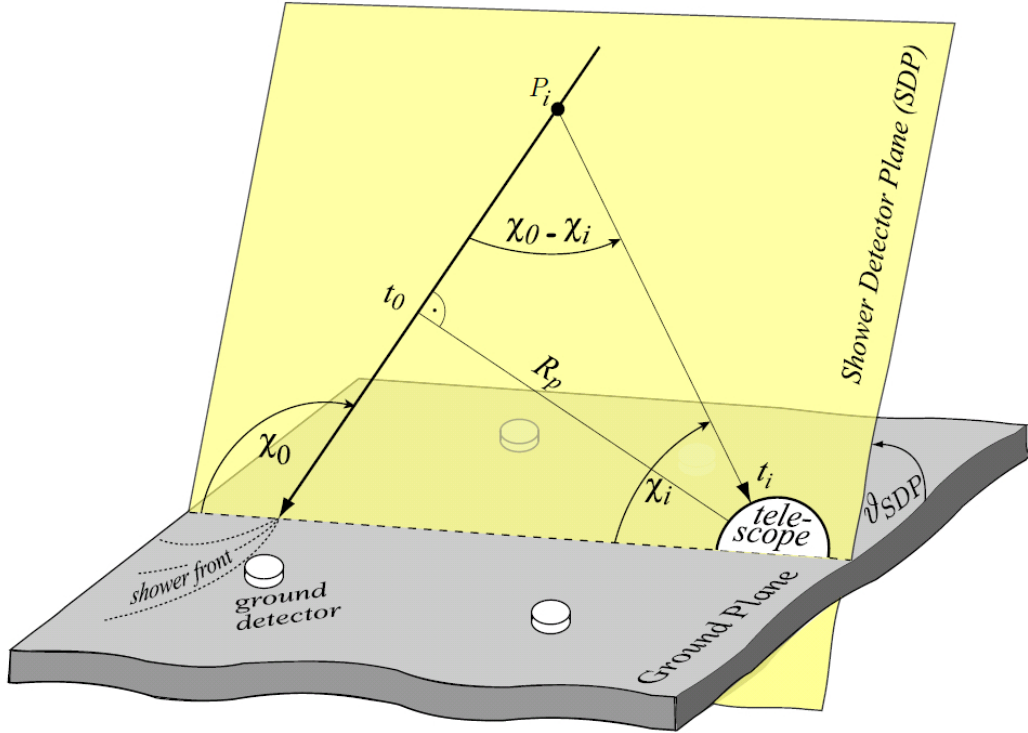
Figure 4.2: Shower axis reconstruction. Different quantities used in reconstruction are introduced. χ_i are the acute angles between horizontal line in the SDP and join of the FD telescope and points on the shower axis P_i. Triangle T is specified by FD telescope, P_i and the shower core. In the following, $\psi = \pi - \chi_0$ is the inner angle of the triangle T at the shower core vertex and χ_0 is the exterior angle at the same vertex. t_i are the arrival times of the fluorescence light from P_i to the FD camera. t_0 is the reference time when the light is emitted at the closest point of the shower axis to the FD telescope. R_p is the perpendicular distance of the FD telescope to the shower axis. θ_{SDP} is the angle between the ground and the SDP. Picture is taken from Ref.[46].

The first step of monocular reconstruction is determination of a shower–detector plane (SDP). It is given as the plane in which the shower axis and the fluorescence detector lay. This is done by SDP fit which uses the pointing directions of each phototube together with integral signal information. Phototube time information is not used. SDP fit consists of constructing the trial planes and comparing them with the pointing directions of the phototube by minimizing sum of residuals between SDP and phototube pointing directions with respect to θ_{SDP} angle of the SDP. θ_{SDP} assigns the angle between the ground and the SDP, see Fig.4.2.

Once the shower–detector plane is determined, the time information from phototubes is used to determine the geometry of the shower development. It is given in Fig.4.2 and 4.3. χ_i is the $i-$th phototube pointing angle in the SDP and ψ assigns the angle of the axis in the SDP. For determination of angle ψ, a timing relation given in Eq.(4.19) is employed, see Fig.4.2. Assuming the fluorescence light to be emitted by a point–like object moving at velocity c along the shower axis, the shower propagation time $\tau_{\mathrm{s},i}$ from point P_i to the point at reference time t_0 on the shower axis is

$$\tau_{\mathrm{s},i} = \frac{R_{\mathrm{p}}}{c\tan(\chi_0 - \chi_i)}, \qquad (4.16)$$

where R_{p} is a perpendicular distance from the shower axis to the FD telescope and χ_0 is the angle between the horizontal line in the SDP and the shower axis, see Fig.4.2. Assuming the fluorescence photons to propagate on the straight lines with velocity c, the light propagation time $\tau_{\mathrm{l},i}$ from P_i to the FD eye is

$$\tau_{\mathrm{l},i} = \frac{R_{\mathrm{p}}}{c\sin(\chi_0 - \chi_i)}. \qquad (4.17)$$

If we also assume that the light is emitted immediately at the point P_i, an expected arrival time to the FD camera is

$$
\begin{aligned}
t_i &= t_0 - \tau_{\mathrm{s},i} + \tau_{\mathrm{l},i} \\
&= t_0 + \frac{R_{\mathrm{p}}}{c}\left(\frac{1}{\sin(\chi_0 - \chi_i)} - \frac{1}{\tan(\chi_0 - \chi_i)}\right) \\
&= t_0 + \frac{R_{\mathrm{p}}}{c}\tan\left(\frac{\chi_0 - \chi_i}{2}\right). \qquad (4.18)
\end{aligned}
$$

It follows that the timing relation is given by

$$t(\theta_i) = \frac{R_{\mathrm{p}}}{c}\tan\frac{\theta_i}{2} + t_0, \qquad (4.19)$$

where t_0 is the time when the shower reaches the point A in the Fig.4.3 and $\theta_i = \pi - \psi - \chi_i$. This derivation and a more general discussion about the fluorescence light propagation, the time delays caused by a fluorescence deexcitation itself and the other effects can by found in Ref.[46].

Once one derived the timing relation, a proper fit of the data to this equation can be performed. This is done by minimizing time residuals with respect to the R_{p} and the shower axis ψ angle in the SDP. When one estimate geometry of the shower axis, one can calculate the expected arrival times of the photons to the
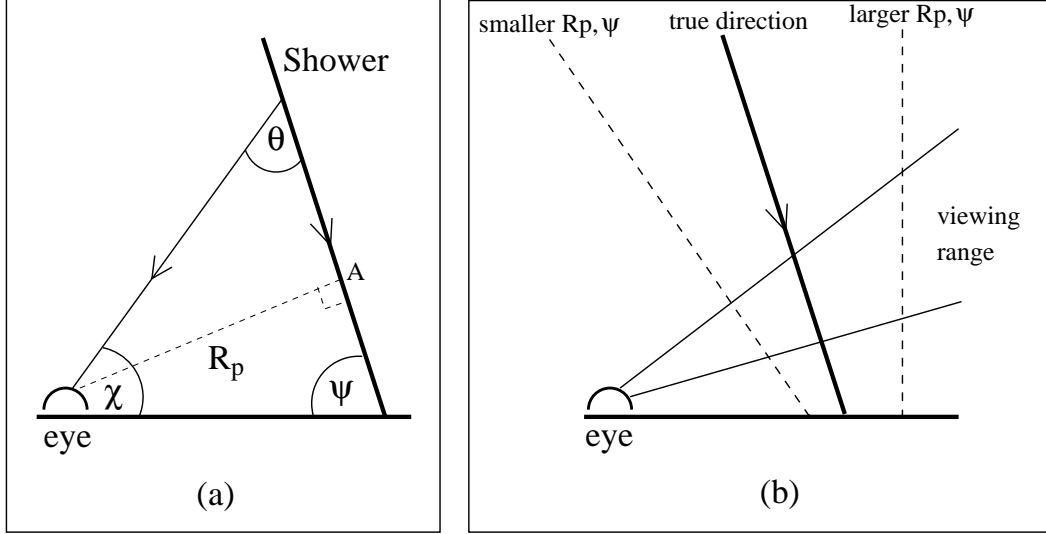
Figure 4.3: Monocular reconstruction (a) and its ambiguity of the axis in the shower–detector plane (b). Each of the three shower tracks at (b) would pass through the detector's field of view with similar (and approximately uniform) angular velocity. Picture is taken from Ref.[3].

FD eye. Fluorescence ρ_1^2 term has a form

$$\rho_1^2 = \frac{N_t}{\sum_{i=1}^n pe_i} \sum_{i=1}^n \frac{(t_i - t_{\text{expected},i})^2}{\sigma_{ti}^2} pe_i, \tag{4.20}$$

where t_i are estimates of the pulse mid–point time, σ_{ti} are the mid–point time uncertainties for each phototube, N_t is a number of firing phototubes. All elements are weighted by the total signal in each phototube pe_i.

After the time fit, one know θ_{SDP} and ψ angles, which can be easily recalculated in to the zenith angle θ and the azimuth angle ϕ of the shower axis. This method is in principle sufficient for the reconstruction of the shower geometry. It was used for the shower reconstruction at the Fly's Eye and HiRes experiments [64]. But in comparison with the Hybrid reconstruction or the Multiple–eye reconstruction it is much less accurate, see Sections 4.3 and 4.4. This is caused by the fact that the timing relation given in Eq.(4.19) is fitted with respect to two parameters R_{p} and ψ. If the time–angle path in the FD camera is too short, it can be accurately fitted by a line. Thus there can be an ambiguity in determination of the shower axis parameters. This problem is shown in Fig.4.3.

4.3   Hybrid Reconstruction

Hybrid reconstruction method is one of the key reconstruction method used at the Pierre Auger Observatory. It is based on adding information from SD tanks to the FD reconstruction time fit. In the beginning, it follows the reconstruction of the Monocular FD method, see Section 4.2. The shower–detector plane fit is performed and the timing relation written in Eq.(4.19) is adopted. Then the two
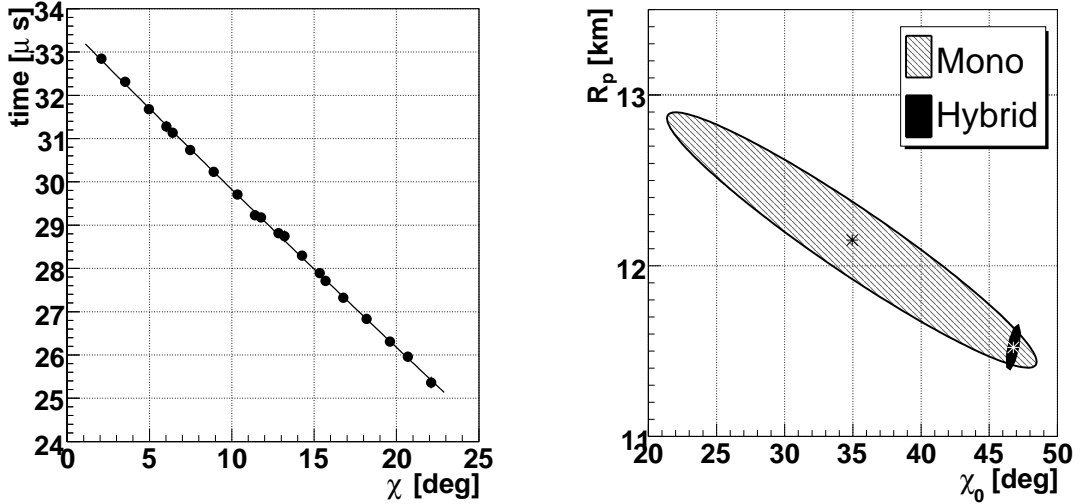
Figure 4.4: Time–angle path for the Monocular reconstruction (left) and R_p and ψ determination improvement for the Hybrid reconstruction (right). Picture is taken from Ref.[51].

parts of residuals are stated

$$\rho^2 = \rho_1^2 + \rho_2^2, \tag{4.21}$$

where ρ_1^2 stands for the fluorescence timing term and ρ_2^2 assigns the SD residuals. Form of the ρ_1^2 is the same as in Monocular FD reconstruction, see Eq.(4.20). Following the Design Report [3], form of the ρ_2^2 is

$$\chi_2^2 = \frac{(t_i - t_\mathrm{exp})^2}{\sigma_{ti}^2}, \tag{4.22}$$

where t_i is a mean arrival time of the particles to the tank with the largest particle count and

$$\sigma_{ti} = \frac{\sigma_{0i}}{\sqrt{n_i}}, \tag{4.23}$$

where σ_{0i} is a dispersion in the particle arrival time and n_i is a number of particles detected in the tank. Parameter t_exp is computed from a position of the tank and a curvature of the shower front estimated from simulation[7].

Hybrid reconstruction is much more accurate in comparison with the Monocular FD reconstruction. It is caused by effectively larger time–angle path due to the incorporated SD tank signals. Because of that the fit of Eq.(4.19) has no degeneration and both R_p and ψ can be accurately obtained, see Fig.4.4.

Hybrid reconstruction time fit of the detected event is shown in Fig.4.5.

At the Pierre Auger Observatory, Hybrid reconstruction is the main reconstruction method of the FD signal. This method is one of the biggest advantage of the observatory. The only reconstruction method that is in principle equally accurate is the Multiple–eye reconstruction.

---

[7] Typical vertical curvature ($\frac{1}{R_0}$, see footnote [4] in Section 4.1) used at the Pierre Auger Observatory in the reconstruction is 0.0001111 m^{-1}
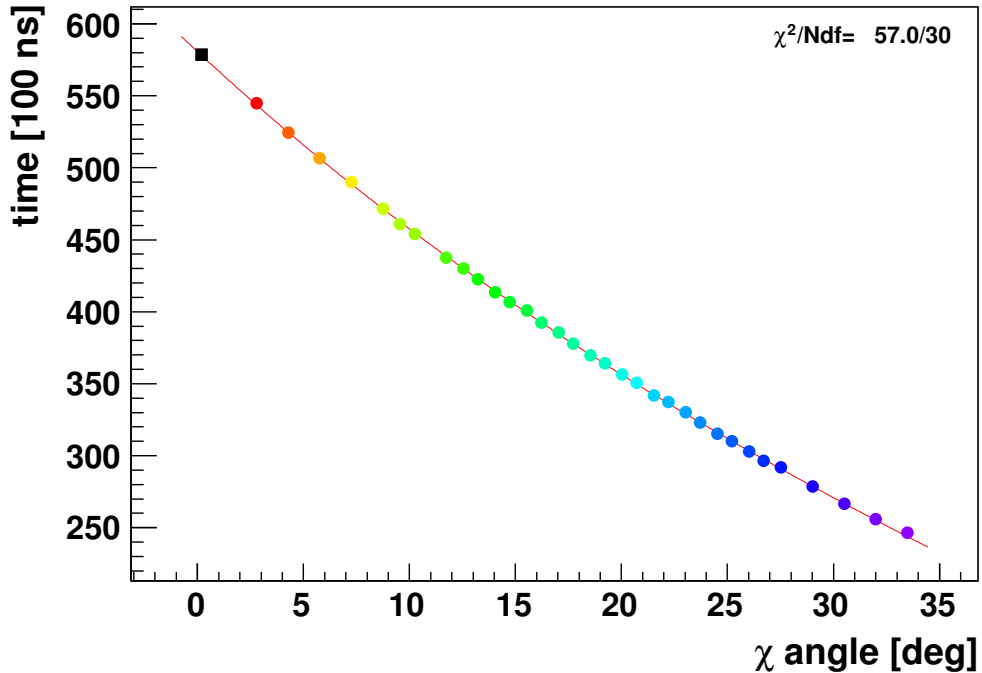
Figure 4.5: Hybrid reconstruction time fit of event No. 200827505541 registered at Coihueco site by mirror 3. Red line is reconstructed shower axis. Colour dots represent points measured by FD eye, the black dot is from the SD array. Picture is prepared in the Auger Offline EventBrowser [14].

4.4 Multiple–eye Reconstruction

Previously presented methods use information from the SD tanks and/or from one FD telescope. Multiple–eye reconstruction mechanism is based on the fact that if one use information from two or more different fluorescence detector eyes, degeneration of the time fit described in Section 4.2 and illustrated in Fig.4.3 no longer exists. One of the advantage of the Multiple–eye reconstruction is the fact that it should be in principle equally accurate as the Hybrid reconstruction but it does not need information from the SD array. Thus Multiple–eye reconstruction could be an independent test of detector functionality. It could reconstruct events in which no SD information is present. In the future, it could be also used in projects where no SD array is possible to build, for example in the space. There is also the project called FAST at the Pierre Auger Observatory to increase a number of the fluorescence stations with a small number of wide–angle phototubes, data of which will be reconstructed in Multiple–eye mode.

There are two types of Multiple–eye reconstruction fits. In practice both methods are usually performed simultaneously with appropriate weights.

4.4.1 Multiple–eye Shower–Detector Plane Fit

The idea of the multiple SDP fit is presented in Fig.4.6. An intersection of the two or more shower–detector planes forms the shower axis. Practically it is represented by a minimization of a sum of the individual off plane angles
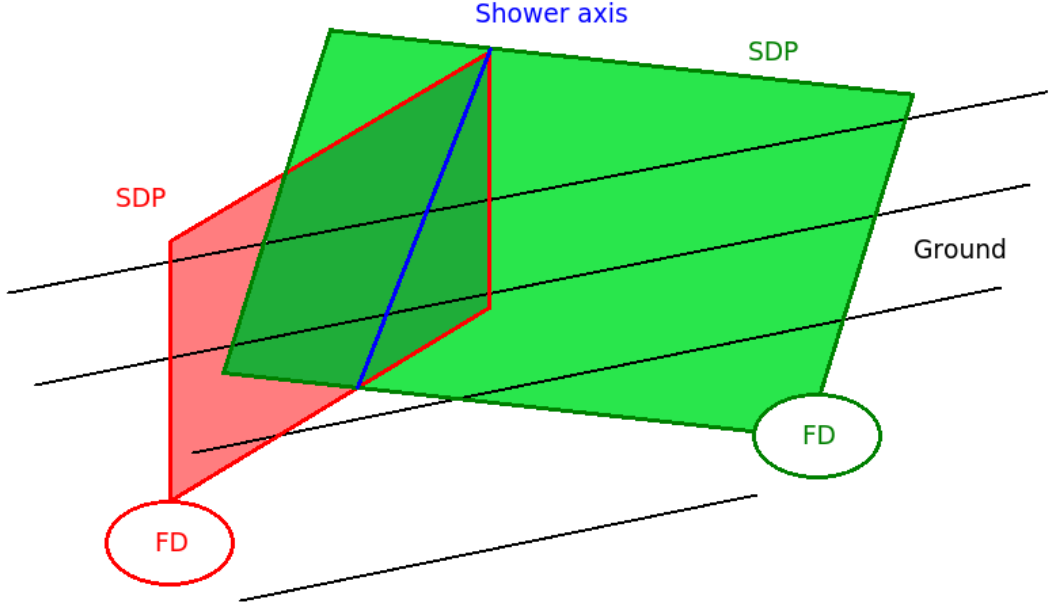
Figure 4.6: Schematic view of the Stereo shower–detector plane reconstruction. Two SDPs intersect in the shower axis.

residuals for all pixels in all FD telescopes included in the Multiple–eye SDP fit. The fit is performed with respect to the zenith angle θ, the azimuth angle ϕ and an impact point of the shower axis. The impact point is the point where the shower axis intersects the ground or selected horizontal plane[8]. In this type of reconstruction, no time information from phototubes is needed. This is an advantage because several time offset problems can be overcome. But it is also a disadvantage because the measurement of the time is very accurate in comparison to the measurement of the pointing angle. A sum of angle residuals is given by

$$\rho_{\text{SDP}}^2 = \frac{N_t}{\sum_{i=1}^{n} pe_i} \sum_{i=1}^{n} \frac{\left(\frac{\pi}{2} - \Delta\phi_i\right)^2}{\sigma_i^2} pe_i, \quad (4.24)$$

where N_t is the number of firing phototubes, pe_i is the total signal in $i-$th phototube, $\Delta\phi_i$ is the angle between the normal of the shower axis projection in the FD camera and the pointing direction of the phototube, and σ_i is the uncertainty of the angle. This uncertainty is 0.35° at the Pierre Auger Observatory.

4.4.2 Multiple–eye Time Fit

The Multiple–eye time fit is based on the same procedure as the Monocular time fit, see Section 4.2. The only difference is that time information from all included eyes contribute to the total sum of time residuals

$$\rho_{\text{tot}}^2 = \sum_{i=1}^{k} \rho_i^2, \quad (4.25)$$

---

[8] Usually in UTM (Universal Time Mercator) coordinate system with easting and northing coordinates at a reference altitude.

where ρ_i^2 belongs to $i-$th eye and has the form given in Eq.(4.20).

Visualization of the real event reconstructed by the Multiple–eye reconstruction is shown in Fig.4.7.

4.5 Energy and Longitudinal Profile

When a geometry of the shower is accurately determined, it is necessary to estimate its energy and longitudinal profile. If we have information from FD eye, these estimates are simple in principle. One can compute the distance of the shower axis in the direction of each phototube, compute an attenuation of the light intensity in the atmosphere along the propagation distance and then, by knowing the total signal in each phototube, compute the shower energy deposited in the atmosphere. This way, the longitudinal profile and the total energy of the shower is obtained. From a geometry of the shower also an amount of scattered and Čerenkov light that effects the signal in the phototubes can by estimated and appropriate corrections can be applied. According to the simulations, total amount of electromagnetic energy deposited in the atmosphere is approximately 90% of the energy of the primary particle. The rest of the energy is formed mainly by muons and neutrinos.

Total electromagnetic shower energy can be estimated from a total integral of the measured longitudinal profile

$$E_{\mathrm{EM}} = 2.2\mathrm{MeV}g^{-1}\mathrm{cm}^2 \int N_{\mathrm{e}}(X)dX, \qquad (4.26)$$

where $N_{\mathrm{e}}(X)$ is the number of charged particles at the atmospheric depth X. A charged particle in the cascade deposits on average of 2.2 MeV into the atmosphere in each depth interval of the width of 1 g cm^{-2} [47].

For accurate determination of the longitudinal profile it is necessary to know the air density as a function of an altitude, the fluorescence yield, the concentration of aerosols and other parameters of the atmosphere. For more information about aerosols see Ref.[48] and for the atmospheric conditions at the Pierre Auger Observatory see Ref.[45]. Monitoring of the atmosphere is done by the system of four lidar stations, see e.g. Ref.[19].

4.6 Auger Offline Reconstruction Software

Auger Offline is the main reconstruction and detector simulation tool at the Pierre Auger Observatory.

The Offline framework consists of three principal parts: a collection of processing modules which can be assembled and sequenced by instructions provided in an XML file, an event data model through which modules can relay data to one another and which accumulates all simulation and reconstruction information, and a detector description which provides a gateway to data describing the configuration and performance of the observatory as well as atmospheric conditions as a function of time. Its schema is presented in Fig.4.8.

Data reconstructed by the Auger Offline framework are stored in a special ROOT data files [23] called ADST (Advanced Data Summary Trees). These trees
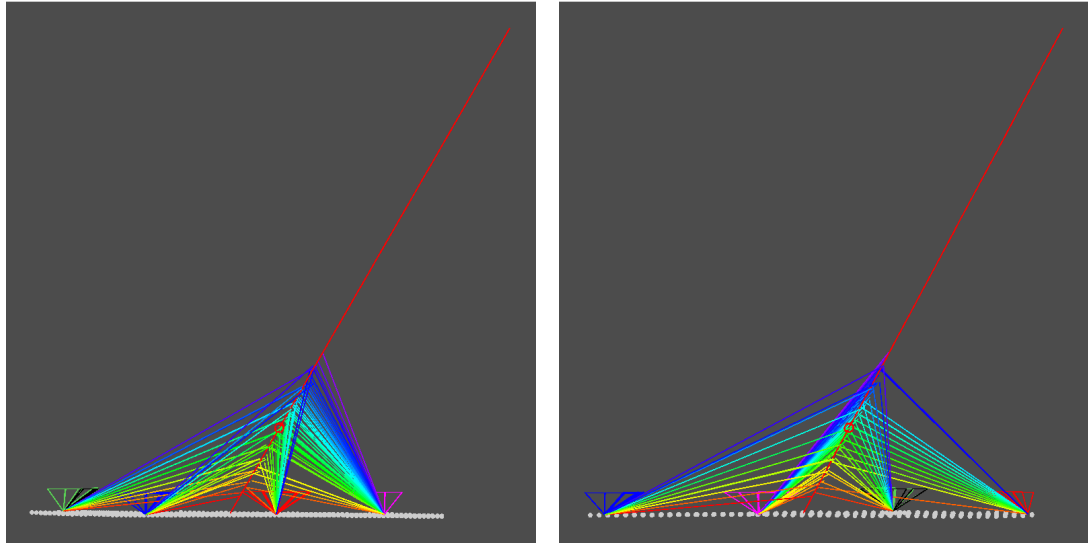
(a) Front view

(b) Side view
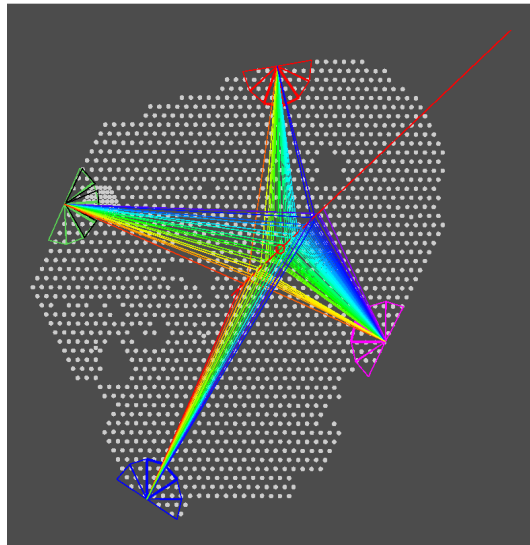
(c) Top view

Figure 4.7: Multiple–eye reconstruction of event No. 201001804541. Colour lines indicates the rays of fluorescence light with time information matching the colours. Three different views are presented. Picture is prepared in the Auger Offline EventBrowser [14].
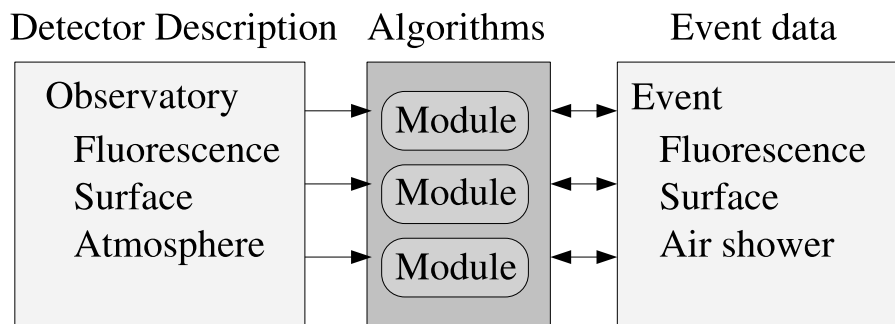
Figure 4.8: General structure of the Offline framework. Simulation and reconstruction tasks are broken down into modules. Each module is able to read information from the detector description and/or the event, process the information, and write the results back into the event. Picture is taken from Ref.[14].

contain all necessary physical information of reconstructed measured or simulated events. Data files can be read either by a standard C++/ROOT programs with appropriate classes or by the EventBrowser program included in the Auger Offline which is a graphical tool for events investigation.

For more details on the Auger Offline Framework see Ref.[14].

5. Resolution of Reconstruction Techniques

In this chapter, I will present results of my own calculations of SD, Hybrid and Multiple–eye[1] reconstructions. For Hybrid and Stereo reconstructions, energy, angular and X_{max} resolutions are calculated both from simulations and from data measured at the Pierre Auger Observatory. For the SD reconstruction, only energy and angular resolutions are calculated from simulations.

Auger experimental data are taken from Centre de Calcul de l'Institut National de Physique Nucléaire et de Physique des Particules (CC-IN2P3) [1] in Lyon where central data depository is placed. Experimental data are actual to the 11th of November 2012. Hybrid reconstructions are performed by the Auger Observer group [2] and Stereo reconstructions are performed by myself.

Simulated showers are also taken from CC-IN2P3 together with their Hybrid reconstructions. Proton induced showers simulated in CORSIKA with high energy interaction model EPOS 2 are chosen. Stereo reconstructions of simulations are performed by myself. Simulated events are actual to the 10th of February 2013.

I performed Stereo reconstruction with SDP fit and time fit, see Section 4.4. Weights of the SDP and time fits are 5 and 1, respectively.

Cuts on both simulations and experimental data are done to improve quality of the reconstructed sample. These cuts for all data are

- reconstructed zenith angle $\theta < 90°$,
- reconstructed FD energy $E > 10^{18}$ eV,
- X_{max} in the field of view of the FD camera,
- X_{max} error less than 40 g cm^{-2},
- minimum viewing angle 20°,
- longitudinal profile residual Gaisser–Hillas fit $\chi^2 < 2.5$,
- maximum hole in depth profile $< 20\%$,

and for experimental data also

- bad FD period rejection,
- no bad pixels in FD camera,
- has entry in aerosols Mie database,
- vertical aerosol optical depth > 0.1,
- Lidar cloud removal – cloud coverage $< 25\%$.

---

[1] The Multiple–eye reconstruction is often called the Stereo reconstruction for simplicity.

5.1 SD Reconstruction

The SD reconstruction method is described in Section 4.1. In the SD reconstruction, it is possible to calculate shower geometry, in particular zenith angle θ and azimuth angle ϕ of showers. EAS Energy E can be deduced as well. Longitudinal EAS profile can not be measured. Energy and angular resolutions of the SD reconstruction are calculated in this Section using simulated events.

5.1.1 Monte Carlo Simulations

The energy resolution of the SD reconstruction can be determined from Monte Carlo simulations. Simulated energy E_{sim} is subtracted from the reconstructed energy E_{rec}. Histograms of this difference are created. One of these histograms for $E_{\text{sim}} = 10^{19}$ eV and $\theta = 26°$ is shown in Fig.5.1. RMSs of the distributions give the absolute energy resolutions. Means of the distributions are given systematic shifts of the reconstructed energies. If one divides the absolute energy resolution by the energy of the primary CR particles, the relative energy resolution is calculated. Results of the energy resolution analysis of the SD reconstruction are listed in Table 5.1.

Also the angular resolution of the SD reconstruction can be determined from Monte Carlo simulations. One can define the angular resolution as the radius of the circle on the sphere, in which 68% of the events coming from the center of the circle, are reconstructed. It can be calculated from the histogram of angular distances of the reconstructed events from a simulated direction. An example of the histogram for $E_{\text{sim}} = 10^{18.5}$ eV is shown in Fig.5.2. Results of the angular resolution analysis of the SD reconstruction are summarized in Table 5.2.

Table 5.1: Energy resolution of the SD reconstruction from Monte Carlo simulations. E assigns simulated energy of primary protons, θ is zenith angle, N is the number of reconstructed events, $\langle E \rangle = \langle E_{\text{rec}} - E_{\text{sim}} \rangle$, see Fig.5.1, is the mean of energy distribution of reconstructed events. $R_{E-\text{sim}}^{\text{SD}-\text{abs}}$ is the absolute energy resolution of the SD reconstruction, $R_{E-\text{sim}}^{\text{SD}-\text{rel}}$ is the relative energy resolution of the SD reconstruction. Listed uncertainties correspond to statistical errors.

Log(E/eV)	θ [°]	N	$\langle E \rangle$ [EeV]	$R_{E-\text{sim}}^{\text{SD}-\text{abs}}$ [EeV]	$R_{E-\text{sim}}^{\text{SD}-\text{rel}}$ [%]
18.5	0	197	-0.65 ± 0.03	0.40 ± 0.02	12.5 ± 0.6
	18	273	-0.71 ± 0.02	0.41 ± 0.02	12.8 ± 0.5
	26	341	-0.65 ± 0.02	0.39 ± 0.02	12.5 ± 0.5
	32	425	-0.66 ± 0.02	0.40 ± 0.01	12.6 ± 0.4
	38	425	-0.58 ± 0.02	0.41 ± 0.01	13.1 ± 0.4
	41	519	-0.61 ± 0.02	0.42 ± 0.01	13.4 ± 0.4
	45	400	-0.66 ± 0.02	0.48 ± 0.02	15.3 ± 0.5
	49	482	-0.73 ± 0.02	0.48 ± 0.02	15.3 ± 0.5
	53	307	-0.95 ± 0.03	0.51 ± 0.02	16.1 ± 0.7
	57	359	-1.01 ± 0.03	0.49 ± 0.02	15.4 ± 0.6
	60	244	-0.89 ± 0.03	0.49 ± 0.02	15.6 ± 0.7
	63	244	-0.80 ± 0.04	0.60 ± 0.03	18.8 ± 0.9
18.5	**0–63**	**4216**	$\mathbf{-0.734 \pm 0.008}$	$\mathbf{0.477 \pm 0.005}$	$\mathbf{15.1 \pm 0.2}$

Continued on next page

Continued from previous page

| Log(E/eV)	θ [°]	N	$\langle E \rangle$ [EeV]	$R_{E-\text{sim}}^{\text{SD}-\text{abs}}$ [EeV]	$R_{E-\text{sim}}^{\text{SD}-\text{rel}}$ [%]
19.0	0	129	-1.92 ± 0.08	0.96 ± 0.06	9.6 ± 0.6
	18	298	-2.02 ± 0.06	1.03 ± 0.04	10.3 ± 0.4
	26	409	-1.84 ± 0.05	1.07 ± 0.04	10.7 ± 0.4
	32	602	-1.78 ± 0.04	1.02 ± 0.03	10.2 ± 0.3
	38	405	-1.65 ± 0.06	1.11 ± 0.04	11.1 ± 0.4
	41	648	-1.61 ± 0.04	1.07 ± 0.03	10.7 ± 0.3
	45	446	-1.88 ± 0.06	1.29 ± 0.04	12.9 ± 0.4
	49	628	-2.28 ± 0.05	1.22 ± 0.03	12.2 ± 0.3
	53	439	-2.61 ± 0.06	1.25 ± 0.04	12.5 ± 0.4
	57	542	-3.25 ± 0.05	1.20 ± 0.04	12.0 ± 0.4
	60	334	-3.31 ± 0.07	1.32 ± 0.05	13.2 ± 0.5
	63	451	-3.20 ± 0.06	1.19 ± 0.04	11.9 ± 0.4
19.0	**0–63**	**5331**	$\mathbf{-2.26 \pm 0.02}$	$\mathbf{1.31 \pm 0.01}$	$\mathbf{13.1 \pm 0.1}$
19.5	0	84	-5.2 ± 0.3	2.8 ± 0.2	8.9 ± 0.7
	18	217	-5.6 ± 0.2	2.5 ± 0.1	7.9 ± 0.4
	26	340	-5.2 ± 0.1	2.5 ± 0.1	7.8 ± 0.3
	32	529	-4.7 ± 0.1	2.46 ± 0.08	7.8 ± 0.2
	38	450	-4.0 ± 0.1	2.9 ± 0.1	9.1 ± 0.3
	41	504	-4.5 ± 0.1	2.57 ± 0.08	8.1 ± 0.3
	45	460	-4.3 ± 0.1	3.1 ± 0.1	9.8 ± 0.4
	49	508	-5.3 ± 0.1	2.85 ± 0.09	9.0 ± 0.3
	53	457	-6.1 ± 0.2	3.4 ± 0.1	10.7 ± 0.4
	57	404	-6.5 ± 0.2	2.8 ± 0.1	8.7 ± 0.4
	60	372	-7.3 ± 0.2	2.7 ± 0.2	8.5 ± 0.5
	63	467	-7.5 ± 0.2	2.3 ± 0.1	7.4 ± 0.4
19.5	**0–63**	**4792**	$\mathbf{-5.21 \pm 0.05}$	$\mathbf{2.94 \pm 0.03}$	$\mathbf{9.3 \pm 0.1}$
20.0	0	20	-7 ± 2	8 ± 2	8 ± 2
	18	96	-10.7 ± 0.7	6.0 ± 0.5	6.0 ± 0.5
	26	275	-9.4 ± 0.5	6.7 ± 0.3	6.7 ± 0.3
	32	316	-9.2 ± 0.4	6.2 ± 0.3	6.2 ± 0.3
	38	242	-6.2 ± 0.5	7.0 ± 0.4	7.0 ± 0.4
	41	379	-7.1 ± 0.4	6.4 ± 0.2	6.4 ± 0.2
	45	357	-8.7 ± 0.4	7.4 ± 0.3	7.4 ± 0.3
	49	471	-9.5 ± 0.4	7.3 ± 0.3	7.3 ± 0.3
	53	238	-11.2 ± 0.7	7.7 ± 0.5	7.7 ± 0.5
	57	658	-12.4 ± 0.5	6.2 ± 0.3	6.2 ± 0.3
	60	403	-13.8 ± 0.8	6.2 ± 0.6	6.2 ± 0.6
	63	396	-14.4 ± 0.6	4.5 ± 0.4	4.5 ± 0.4
20.0	**0–63**	**3851**	$\mathbf{-9.2 \pm 0.2}$	$\mathbf{7.1 \pm 0.1}$	$\mathbf{7.1 \pm 0.1}$
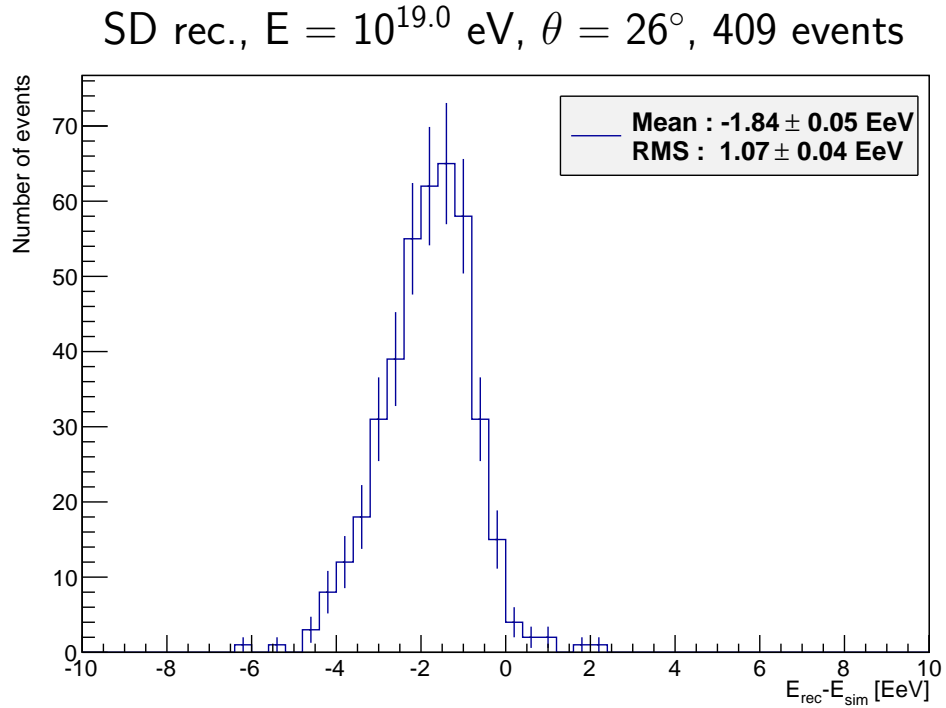
Figure 5.1: Energy resolution of the SD reconstruction for $\theta = 26°$. Simulated data for primary protons with energy 10^{19} eV are depicted.
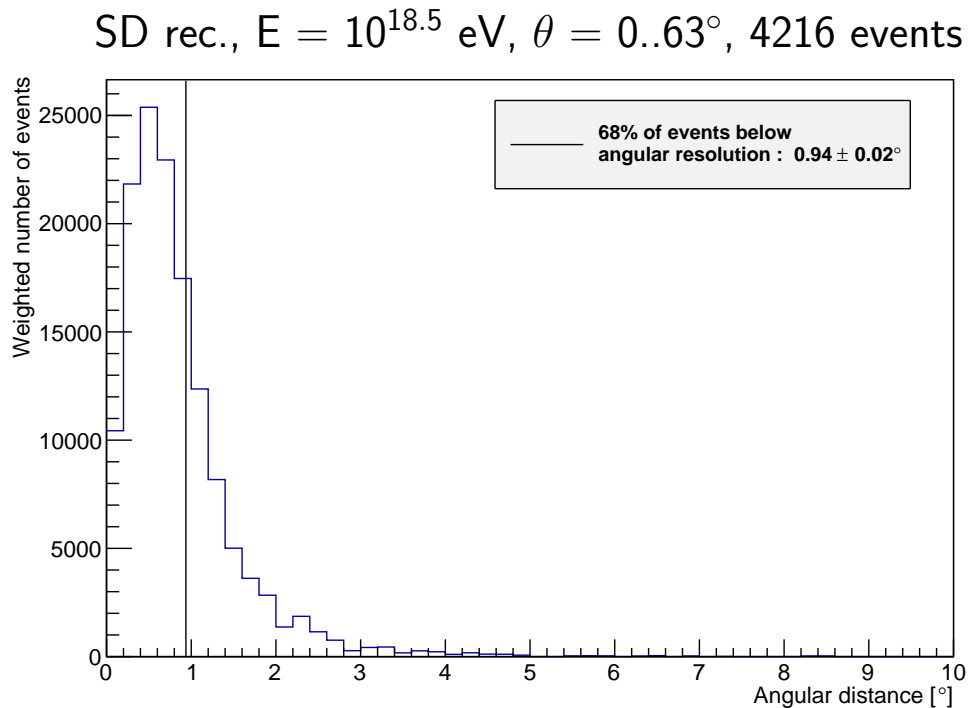
Figure 5.2: Angular resolution of the SD reconstruction for $\theta = 0..63°$. Simulated data for primary protons with energy $10^{18.5}$ eV are depicted. Vertical line marks the boundary below which 68% of events is found.

Table 5.2: Angular resolution of the SD reconstruction from Monte Carlo simulations. E assigns simulated energy of primary protons, θ is zenith angle, N is the number of reconstructed events. $R^{\mathrm{SD}}_{\mathrm{ang-sim}}$ is the angular resolution of the SD reconstruction. Given uncertainties correspond to statistical errors.

Log(E/eV)	θ [°]	N	$R^{\mathrm{SD}}_{\mathrm{ang-sim}}$ [°]
18.5	0	197	1.32 ± 0.07
	18	273	1.23 ± 0.05
	26	341	1.24 ± 0.05
	32	425	1.01 ± 0.03
	38	425	1.03 ± 0.04
	41	519	0.99 ± 0.03
	45	400	0.94 ± 0.03
	49	482	0.82 ± 0.03
	53	307	0.76 ± 0.03
	57	359	0.73 ± 0.03
	60	244	0.78 ± 0.04
	63	244	0.71 ± 0.03
18.5	**0–63**	**4216**	**0.937 ± 0.002**
19.0	0	129	1.00 ± 0.06
	18	298	0.88 ± 0.04
	26	409	0.81 ± 0.03
	32	602	0.76 ± 0.02
	38	405	0.62 ± 0.02
	41	648	0.63 ± 0.02
	45	446	0.58 ± 0.02
	49	628	0.56 ± 0.02
	53	439	0.53 ± 0.02
	57	542	0.52 ± 0.02
	60	334	0.50 ± 0.02
	63	451	0.50 ± 0.02
19.0	**0–63**	**5331**	**0.625 ± 0.001**
19.5	0	84	0.62 ± 0.05
	18	217	0.63 ± 0.03
	26	340	0.55 ± 0.02
	32	529	0.51 ± 0.02
	38	450	0.49 ± 0.02
	41	504	0.50 ± 0.02
	45	460	0.50 ± 0.02
	49	508	0.46 ± 0.01
	53	457	0.44 ± 0.01
	57	404	0.43 ± 0.02
	60	372	0.41 ± 0.02
	63	467	0.36 ± 0.01
19.5	**0–63**	**4792**	**0.479 ± 0.001**
20.0	0	20	0.54 ± 0.09
	18	96	0.52 ± 0.04

Log(E/eV)	θ [°]	N	$R^{\text{SD}}_{\text{ang-sim}}$ [°]
	26	275	0.51 ± 0.02
	32	316	0.46 ± 0.02
	38	242	0.42 ± 0.02
	41	379	0.41 ± 0.01
	45	357	0.42 ± 0.02
	49	471	0.38 ± 0.01
	53	238	0.34 ± 0.02
	57	658	0.334 ± 0.009
	60	403	0.34 ± 0.01
	63	396	0.31 ± 0.01
20.0	**0–63**	**3851**	**0.394 ± 0.001**

The data in Tables 5.1 and 5.2 clearly show that both relative energy and angular resolutions go down with respect to the energy of primary particles. It is caused by higher number of particles in the EAS and thus higher number of hit tanks of the SD array. Number of hit tanks depends on zenith angle as well. Because of that, the resolutions are better at higher θ. Also there is a systematic shift of the reconstructed energy which is a part of the systematic uncertainty of the reconstruction. For more details see Ref.[7].

The energy resolution of the SD reconstruction is poorer in comparison to Hybrid and Stereo reconstructions. The angular resolution is poorer for energy $10^{18.5}$ eV as well. For higher energies the angular resolution is comparable to the Stereo reconstruction resolution and even better than the Hybrid reconstruction resolution. These results are in overall agreement with the results published in Ref.[22].

5.2 Hybrid Reconstruction

The Hybrid reconstruction method is introduced in Section 4.3. In the Hybrid reconstruction, it is possible to calculate shower geometry, in particular zenith angle θ and azimuth angle ϕ of showers. Their energy E and longitudinal profile, i.e. atmospheric depth X_{max}, can be calculated as well. In this Section, shower energy, X_{max} and corresponding angular resolutions of the Hybrid reconstruction are obtained both from simulations and experimental Auger data.

5.2.1 Monte Carlo Simulations

Method of the absolute and relative energy resolution determination is similar to that one used in Section 5.1.1. Definition of the angular resolution is the same as in Section 5.1.1 and method of its calculation is similar. Histograms used for the determination of energy resolutions for showers with energy $E = 10^{18.5}$ eV and zenith angle $\theta = 32°$ and for $E = 10^{19.5}$ eV, $\theta = 0..63°$ are depicted in Figs.5.3 and 5.5, respectively. Histogram used for the determination of the angular resolution for $E = 10^{19}$ eV is shown in Fig.5.4.
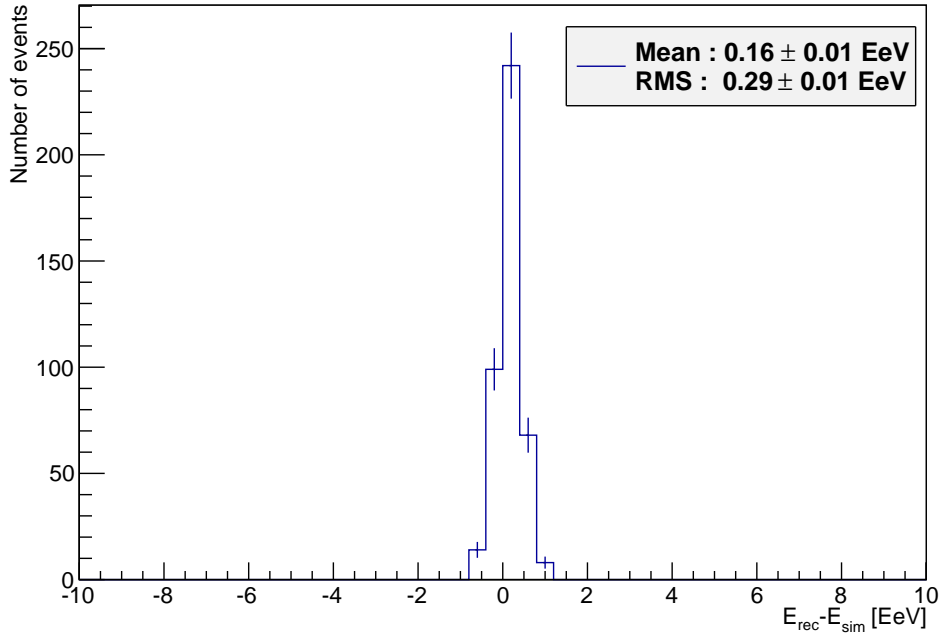
Figure 5.3: Energy resolution of the Hybrid reconstruction for $\theta = 32°$. Simulated data are used. Energies of primary protons are $10^{18.5}$ eV.

In the Hybrid reconstruction, the $X_{\max}$ resolution can be calculated as well. Simulated $X_{\max-\text{sim}}$ is subtracted from reconstructed $X_{\max-\text{rec}}$ and distributions of these differences are created. One of such histograms for $E = 10^{20}$ eV is shown in Fig.5.6. RMSs of the distributions define the $X_{\max}$ resolutions. Means of the distributions are then given systematic shifts of the reconstructed $X_{\max}$.

Results of energy and $X_{\max}$ resolution analyses of the Hybrid reconstruction on simulated data are summarized in Tables 5.3 and 5.4, respectively. Results of the angular resolution on simulated data are listed in Table 5.5.

Table 5.3: Energy resolution of the Hybrid reconstruction from Monte Carlo simulations. E assigns simulated energy of primary particles, θ is zenith angle, N is the number of reconstructed events, $\langle E \rangle = \langle E_{\text{rec}} - E_{\text{sim}} \rangle$, see Fig.5.3, is the mean of energy distribution of reconstructed events. $R_{E-\text{sim}}^{\text{hyb-abs}}$ is the absolute energy resolution of the Hybrid reconstruction, $R_{E-\text{sim}}^{\text{hyb-rel}}$ stands for the relative energy resolution of the Hybrid reconstruction. Uncertainties correspond to statistical errors.

Log(E/eV)	θ [°]	N	$\langle E \rangle$ [EeV]	$R_{E-\text{sim}}^{\text{hyb-abs}}$ [EeV]	$R_{E-\text{sim}}^{\text{hyb-rel}}$ [%]
18.5	0	199	0.12 ± 0.02	0.34 ± 0.02	10.7 ± 0.5
	18	277	0.14 ± 0.02	0.31 ± 0.01	9.8 ± 0.4
	26	344	0.16 ± 0.02	0.29 ± 0.01	9.0 ± 0.3
	32	431	0.16 ± 0.01	0.29 ± 0.01	9.1 ± 0.3
	38	437	0.17 ± 0.01	0.28 ± 0.01	9.0 ± 0.3
	41	534	0.15 ± 0.01	0.252 ± 0.008	8.0 ± 0.2

Continued on next page

Log(E/eV)	θ [°]	N	$\langle E \rangle$ [EeV]	$R_{E-\text{sim}}^{\text{hyb}-\text{abs}}$ [EeV]	$R_{E-\text{sim}}^{\text{hyb}-\text{rel}}$ [%]
	45	418	0.16 ± 0.01	0.250 ± 0.009	7.9 ± 0.3
	49	518	0.16 ± 0.01	0.243 ± 0.008	7.7 ± 0.2
	53	335	0.14 ± 0.01	0.27 ± 0.01	8.4 ± 0.3
	57	394	0.13 ± 0.01	0.264 ± 0.009	8.3 ± 0.3
	60	260	0.11 ± 0.02	0.30 ± 0.01	9.6 ± 0.4
	63	263	0.13 ± 0.02	0.28 ± 0.01	9.0 ± 0.4
18.5	**0–63**	**4410**	**0.149 ± 0.004**	**0.275 ± 0.003**	**8.7 ± 0.1**
19.0	0	137	-0.02 ± 0.09	1.03 ± 0.06	10.3 ± 0.6
	18	333	0.31 ± 0.05	0.92 ± 0.04	9.2 ± 0.4
	26	478	0.40 ± 0.05	1.03 ± 0.03	10.3 ± 0.3
	32	730	0.34 ± 0.03	0.88 ± 0.02	8.8 ± 0.2
	38	550	0.39 ± 0.04	0.82 ± 0.02	8.2 ± 0.2
	41	915	0.36 ± 0.03	0.82 ± 0.02	8.2 ± 0.2
	45	693	0.40 ± 0.03	0.73 ± 0.02	7.3 ± 0.2
	49	1033	0.33 ± 0.02	0.63 ± 0.01	6.3 ± 0.1
	53	710	0.34 ± 0.02	0.65 ± 0.02	6.5 ± 0.2
	57	821	0.31 ± 0.02	0.64 ± 0.02	6.4 ± 0.2
	60	469	0.26 ± 0.03	0.60 ± 0.02	6.0 ± 0.2
	63	617	0.31 ± 0.02	0.62 ± 0.02	6.2 ± 0.2
19.0	**0–63**	**7486**	**0.341 ± 0.009**	**0.767 ± 0.006**	**7.67 ± 0.06**
19.5	0	104	-1.1 ± 0.3	3.3 ± 0.2	10.3 ± 0.7
	18	269	0.5 ± 0.2	2.6 ± 0.1	8.3 ± 0.4
	26	502	0.5 ± 0.1	2.96 ± 0.09	9.4 ± 0.3
	32	870	0.82 ± 0.09	2.65 ± 0.06	8.4 ± 0.2
	38	851	1.02 ± 0.09	2.61 ± 0.06	8.3 ± 0.2
	41	946	1.28 ± 0.08	2.31 ± 0.05	7.3 ± 0.2
	45	942	0.93 ± 0.07	2.01 ± 0.05	6.4 ± 0.1
	49	1051	0.85 ± 0.06	1.82 ± 0.04	5.8 ± 0.1
	53	981	0.80 ± 0.06	1.73 ± 0.04	5.5 ± 0.1
	57	777	0.80 ± 0.06	1.65 ± 0.04	5.2 ± 0.1
	60	703	0.78 ± 0.05	1.45 ± 0.04	4.6 ± 0.1
	63	790	0.81 ± 0.05	1.48 ± 0.04	4.7 ± 0.1
19.5	**0–63**	**8786**	**0.84 ± 0.02**	**2.13 ± 0.02**	**6.74 ± 0.05**
20.0	0	22	2.3 ± 0.7	2.8 ± 0.5	2.8 ± 0.5
	18	121	0.8 ± 0.5	4.9 ± 0.3	4.9 ± 0.3
	26	424	1.6 ± 0.3	4.6 ± 0.2	4.6 ± 0.2
	32	544	1.6 ± 0.2	4.6 ± 0.2	4.6 ± 0.2
	38	507	1.4 ± 0.2	4.6 ± 0.2	4.6 ± 0.2
	41	882	1.7 ± 0.2	4.3 ± 0.1	4.3 ± 0.1
	45	826	1.8 ± 0.1	4.0 ± 0.1	4.0 ± 0.1
	49	1160	2.0 ± 0.1	3.64 ± 0.08	3.64 ± 0.08
	53	586	2.0 ± 0.1	3.5 ± 0.1	3.5 ± 0.1
	57	1554	2.03 ± 0.08	3.20 ± 0.06	3.20 ± 0.06
	60	861	2.0 ± 0.1	2.95 ± 0.07	2.95 ± 0.07
	63	795	2.1 ± 0.1	2.81 ± 0.07	2.81 ± 0.07

Log(E/eV)	θ [°]	N	$\langle E \rangle$ [EeV]	$R^{\text{hyb-abs}}_{E-\text{sim}}$ [EeV]	$R^{\text{hyb-rel}}_{E-\text{sim}}$ [%]
20.0	**0–63**	**8282**	**1.85 ± 0.05**	**3.78 ± 0.03**	**3.78 ± 0.03**

Table 5.4: X_{max} resolution of the Hybrid reconstruction from Monte Carlo simulations. $\langle X_{\text{max}} \rangle = \langle X_{\text{max-rec}} - X_{\text{max-sim}} \rangle$, see Fig.5.6, is the mean of X_{max} distribution of reconstructed events and $R^{\text{hyb}}_{X\text{max-sim}}$ denotes the absolute X_{max} resolution of the Hybrid reconstruction. For more details see caption to Table 5.3.

Log(E/eV)	θ [°]	N	$\langle X_{\text{max}} \rangle$ [g cm^{-2}]	$R^{\text{hyb}}_{X\text{max-sim}}$ [g cm^{-2}]
18.5	0	199	−4 ± 2	28 ± 1
	18	277	−2 ± 2	26 ± 1
	26	344	2 ± 1	22.9 ± 0.9
	32	431	1.5 ± 1.3	27.0 ± 0.9
	38	437	3 ± 1	23.1 ± 0.8
	41	534	3 ± 1	22.3 ± 0.7
	45	418	−0.4 ± 1	20.8 ± 0.7
	49	518	−0.2 ± 0.9	20.3 ± 0.6
	53	335	−1 ± 1	21.1 ± 0.8
	57	394	−2 ± 1	24.1 ± 0.9
	60	260	−0.6 ± 2	24 ± 1
	63	263	0.02 ± 2	27 ± 1
18.5	**0–63**	**4410**	**0.26 ± 0.36**	**23.4 ± 0.3**
19.0	0	137	−6 ± 2	26 ± 2
	18	333	−2 ± 1	23.4 ± 0.9
	26	478	3 ± 1	25.6 ± 0.8
	32	730	1.4 ± 0.9	24.1 ± 0.6
	38	550	3 ± 1	23.3 ± 0.7
	41	915	1.5 ± 0.8	22.8 ± 0.5
	45	693	1.5 ± 0.7	19.7 ± 0.5
	49	1033	0.09 ± 0.6	18.0 ± 0.4
	53	710	0.3 ± 0.7	18.2 ± 0.5
	57	821	−0.6 ± 0.6	16.3 ± 0.4
	60	469	−3.6 ± 0.8	16.3 ± 0.5
	63	617	−4.0 ± 0.7	16.4 ± 0.5
19.0	**0–63**	**7486**	**0.2 ± 0.2**	**20.7 ± 0.2**
19.5	0	104	−17 ± 3	28 ± 2
	18	269	−4 ± 1	23 ± 1
	26	502	−2 ± 1	23.4 ± 0.7
	32	870	2.1 ± 0.8	22.1 ± 0.5
	38	851	2.8 ± 0.8	24.2 ± 0.6
	41	946	4.0 ± 0.7	20.4 ± 0.5
	45	942	2.1 ± 0.6	19.4 ± 0.4
	49	1051	2.0 ± 0.5	17.4 ± 0.4
	53	981	−0.3 ± 0.6	17.6 ± 0.4

Log(E/eV)	θ [°]	N	$\langle X_{\max} \rangle$ [g cm^{-2}]	$R^{\mathrm{hyb}}_{X\mathrm{max-sim}}$ [g cm^{-2}]
	57	777	-0.6 ± 0.6	17.8 ± 0.5
	60	703	-2.4 ± 0.6	15.2 ± 0.4
	63	790	-4.9 ± 0.6	15.9 ± 0.4
19.5	**0–63**	**8786**	**0.3 ± 0.2**	**19.8 ± 0.2**
20.0	0	22	-14 ± 7	31 ± 5
	18	121	-11 ± 2	25 ± 2
	26	424	-5 ± 1	23.2 ± 0.8
	32	544	-3 ± 1	23.8 ± 0.7
	38	507	3 ± 1	23.9 ± 0.8
	41	882	2.8 ± 0.7	21.5 ± 0.5
	45	826	2.4 ± 0.7	19.8 ± 0.5
	49	1160	3.1 ± 0.5	17.2 ± 0.4
	53	586	1.9 ± 0.7	16.6 ± 0.5
	57	1554	0.4 ± 0.4	15.9 ± 0.3
	60	861	-1.5 ± 0.5	15.7 ± 0.4
	63	795	-3.6 ± 0.6	15.9 ± 0.4
20.0	**0–63**	**8282**	**0.5 ± 0.2**	**19.4 ± 0.2**

Table 5.5: Angular resolution of the Hybrid reconstruction from Monte Carlo simulations. $R^{\mathrm{hyb}}_{\mathrm{ang-sim}}$ is the angular resolution of the Hybrid reconstruction. For more details see caption to Table 5.3

Log(E/eV)	θ [°]	N	$R^{\mathrm{hyb}}_{\mathrm{ang-sim}}$ [°]
18.5	0	199	0.58 ± 0.03
	18	277	0.51 ± 0.02
	26	344	0.61 ± 0.02
	32	431	0.80 ± 0.03
	38	437	0.67 ± 0.02
	41	534	0.65 ± 0.02
	45	418	0.60 ± 0.02
	49	518	0.57 ± 0.02
	53	335	0.55 ± 0.02
	57	394	0.55 ± 0.02
	60	260	0.56 ± 0.02
	63	263	0.54 ± 0.02
18.5	**0–63**	**4410**	**0.598 ± 0.001**
19.0	0	137	0.70 ± 0.04
	18	333	0.55 ± 0.02
	26	478	0.85 ± 0.03
	32	730	0.84 ± 0.02
	38	550	0.75 ± 0.02
	41	915	0.69 ± 0.02
	45	693	0.65 ± 0.02

Log(E/eV)	θ [°]	N	$R_{\text{ang-sim}}^{\text{hyb}}$ [°]
	49	1033	0.64 ± 0.01
	53	710	0.57 ± 0.02
	57	821	0.55 ± 0.01
	60	469	0.46 ± 0.02
	63	617	0.43 ± 0.01
19.0	**0–63**	**7486**	**0.623 ± 0.001**
19.5	0	104	0.74 ± 0.05
	18	269	0.57 ± 0.02
	26	502	0.89 ± 0.03
	32	870	0.93 ± 0.02
	38	851	0.89 ± 0.02
	41	946	0.75 ± 0.02
	45	942	0.66 ± 0.02
	49	1051	0.64 ± 0.01
	53	981	0.63 ± 0.01
	57	777	0.54 ± 0.01
	60	703	0.48 ± 0.01
	63	790	0.42 ± 0.01
19.5	**0–63**	**8786**	**0.652 ± 0.001**
20.0	0	22	0.42 ± 0.06
	18	121	0.59 ± 0.04
	26	424	0.95 ± 0.03
	32	544	1.11 ± 0.03
	38	507	1.03 ± 0.03
	41	882	0.87 ± 0.02
	45	826	0.72 ± 0.02
	49	1160	0.64 ± 0.01
	53	586	0.63 ± 0.02
	57	1554	0.515 ± 0.009
	60	861	0.48 ± 0.01
	63	795	0.41 ± 0.01
20.0	**0–63**	**8282**	**0.671 ± 0.001**

Resolutions of the Hybrid reconstruction depend on precision of the time fit, for details of the reconstruction see Section 4.3. Quality of the time fit depends on the number of triggered pixels in FD camera, thus on the angular length of the shower axis in FD camera. Because of that, the resolutions are better for higher angles as can be seen in Tables 5.3, 5.4 and 5.5. Dependence on energies of primary particles is not substantial, because it does not affect the angular length much.

The $X_{\max}$ resolution is approximately 20 g cm^{-2}. This result agrees with the $X_{\max}$ resolution presented in Ref.[9]. Angular and energy resolutions of the Hybrid reconstruction agree with resolutions presented in Refs.[22] and [7] as well.
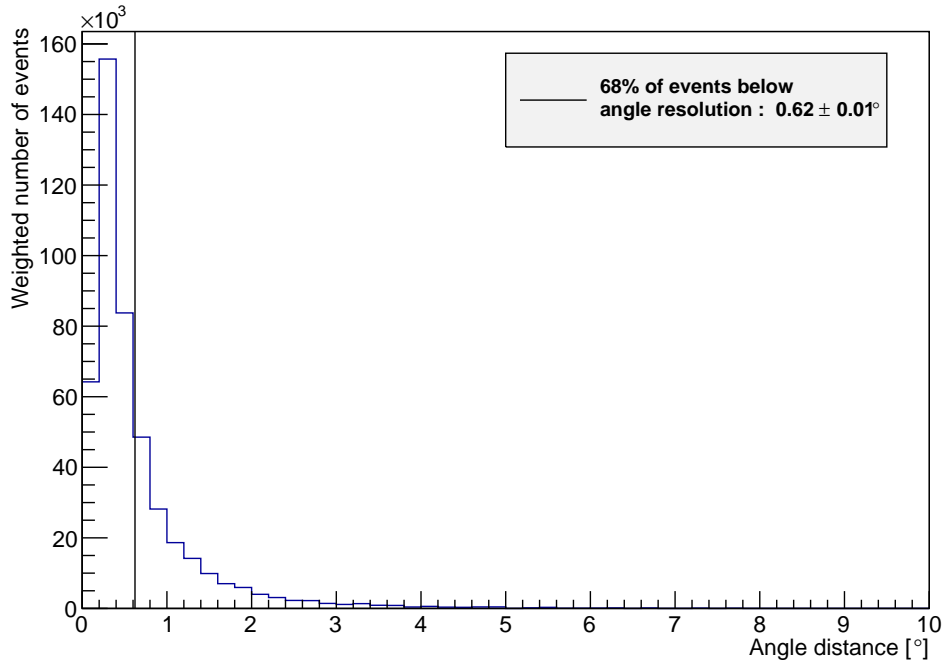
Figure 5.4: Angular resolution of the Hybrid reconstruction for $\theta = 0..63°$. Simulated data are adopted. Energies of primary protons are $10^{19.0}$ eV. Vertical line marks the boundary below which 68% of events is found.
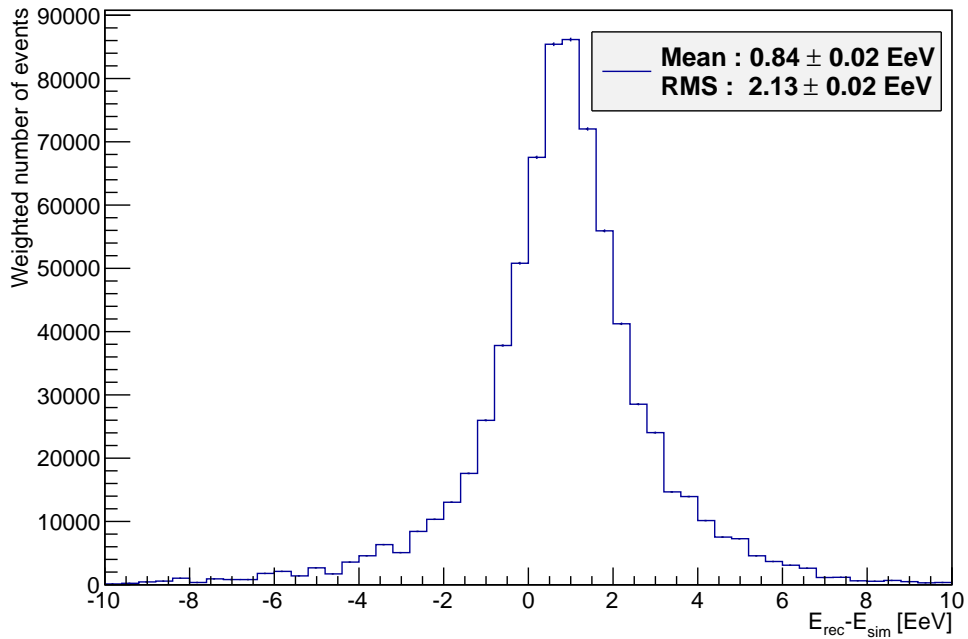

Figure 5.5: Energy resolution of the Hybrid reconstruction for $\theta = 0..63°$. Simulated data for primary protons with energies of $10^{19.5}$ eV are depicted.
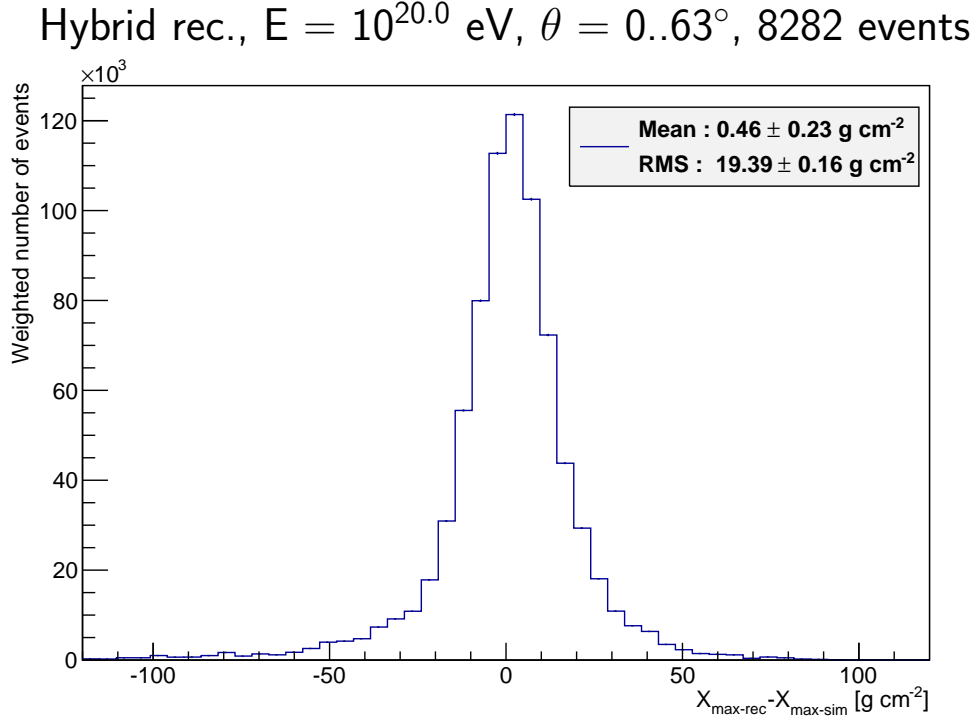
Figure 5.6: X_{max} resolution of the Hybrid reconstruction for $\theta = 0..63°$. Simulated data for primary protons with energies of 10^{20} eV are shown.

5.2.2 Data

Energy, X_{max} and angular resolutions can be determined from experimental data. If one considers showers viewed from two or more FD stations, there exists two or more Hybrid reconstructions of the same shower. Histograms of differences between reconstructed quantities, i.e. E, X_{max} and angular distance, can be created. From these distributions E, X_{max} and angular resolutions can be calculated.

Results of E and X_{max} resolution analyses of the Hybrid reconstruction on experimental data are shown in Figs.5.7 and 5.8, respectively. The angular resolution derived from experimental data is shown in Fig.5.9.

I have obtained the energy resolution of the Hybrid reconstruction as

$$R_{\mathrm{E-dat}}^{\mathrm{hyb}} = 10.2 \pm 0.4\%. \tag{5.1}$$

The value of the X_{max} resolution of the Hybrid reconstruction has turned out to be

$$R_{\mathrm{Xmax-dat}}^{\mathrm{hyb}} = 23.3 \pm 0.9 \text{ g cm}^{-2}, \tag{5.2}$$

and the angular resolution of the Hybrid reconstruction has been calculated as

$$R_{\mathrm{ang-dat}}^{\mathrm{hyb}} = 1.17 \pm 0.05°. \tag{5.3}$$

Uncertainties correspond to statistical errors.

Experimentally obtained values of the resolutions are worse then those obtained by simulations. This can be caused by contributions of atmospheric effects. Accuracy of the Hybrid reconstruction depends on the angular length of
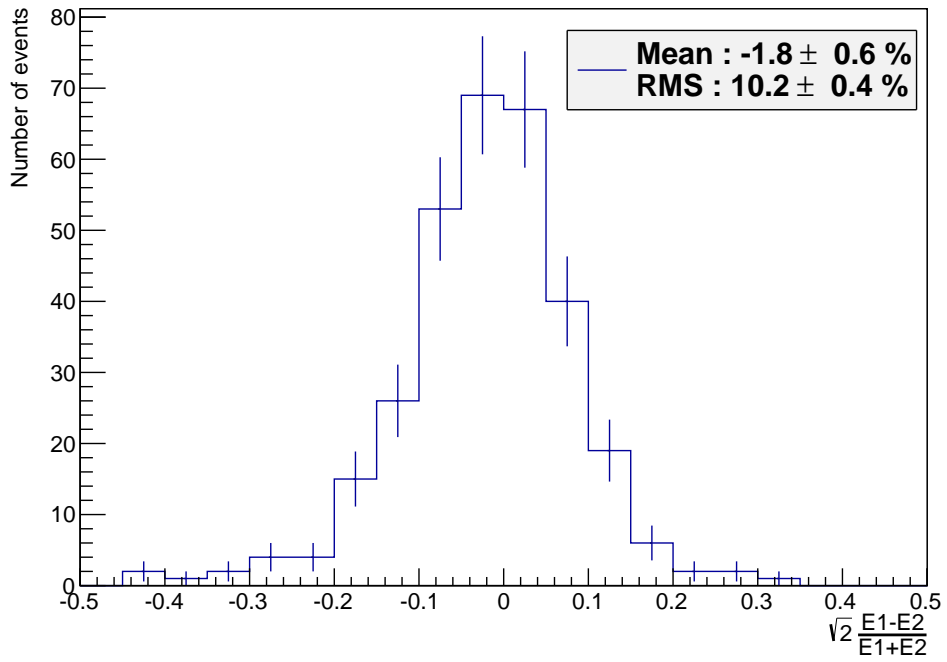
Figure 5.7: Relative energy resolution of the Hybrid reconstruction obtained from experimental data.
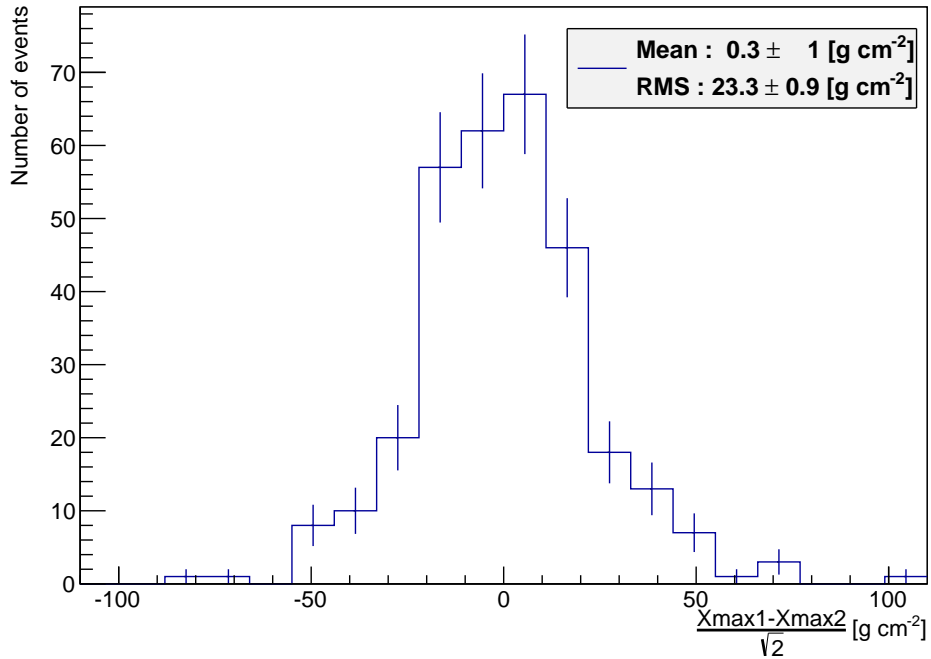
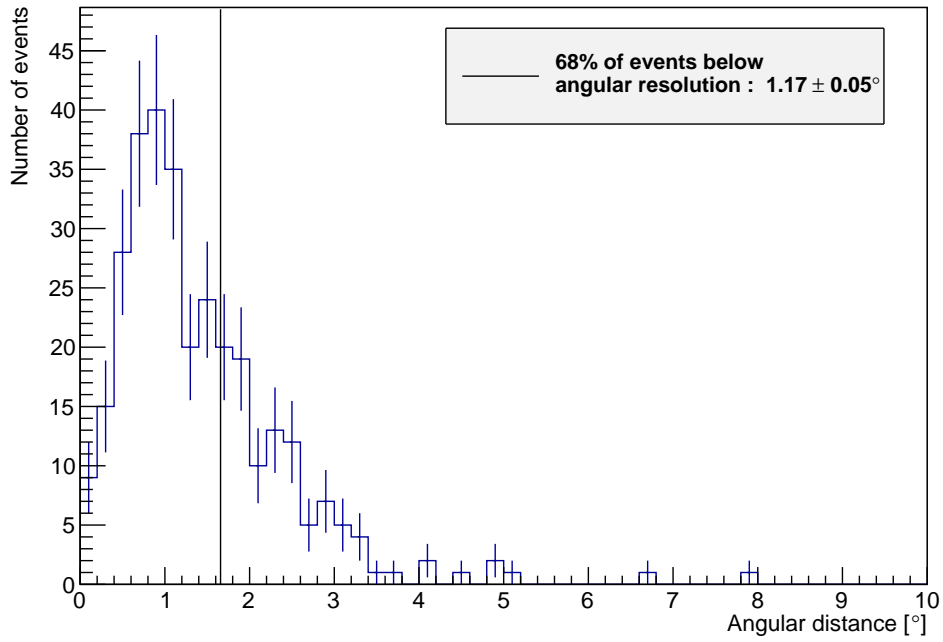Figure 5.8: X_{max} resolution of the Hybrid reconstruction deduced from experimental data.

Figure 5.9: Angular resolution of the Hybrid reconstruction gathered from experimental data. Vertical line marks the boundary below which 68% of events is found.
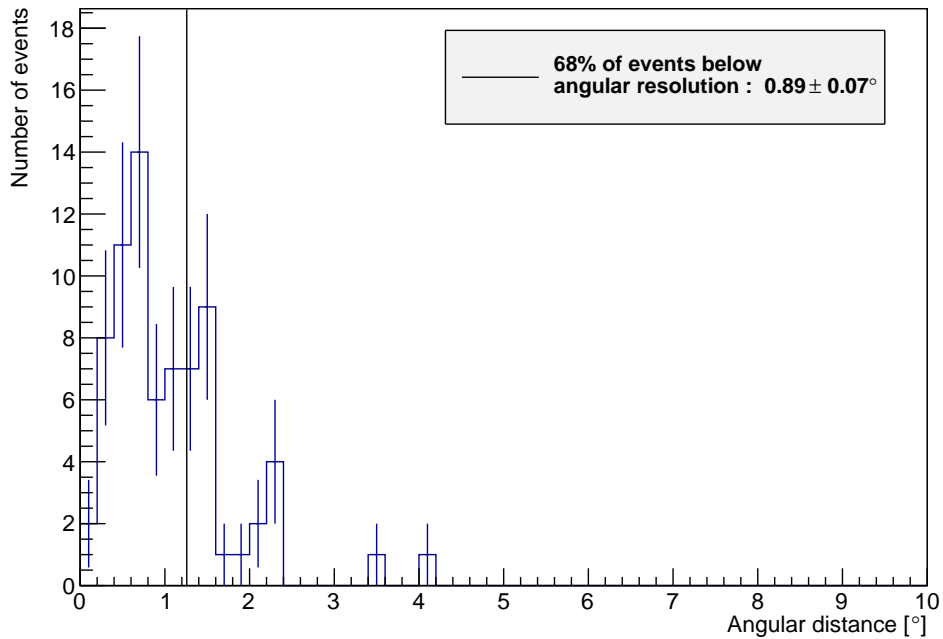

Figure 5.10: Angular resolution of the Hybrid reconstruction gain from experimental data. Additional cut for angular length $> 20°$ is added. Vertical line marks the boundary below which 68% of events is found.

the shower axis in FD camera. This effect is illustrated in Fig.5.10, where additional cut for angular length $> 20°$ is added. The angular resolution in this case is better.

5.3 Multiple-eye Reconstruction

The Multiple–eye reconstruction method is discussed in Section 4.4. In the Stereo reconstruction, it is possible to calculate shower geometry, in particular its zenith angle θ and azimuth angle ϕ. Shower energy E and longitudinal profile, i.e. atmospheric depth $X_{\max}$, can be calculated as well. In this Section, energy, $X_{\max}$ and angular resolutions of the Stereo reconstruction are calculated both from simulations and experimental Auger data.

5.3.1 Monte Carlo Simulations

Methods to deduce the absolute and relative energy resolution and the $X_{\max}$ resolution are similar to those used in Sections 5.1.1 a 5.2.1. Definition of the angular resolution is the same as that one given in Section 5.1.1 and method of its estimation is similar. Histogram used for the determination of the energy resolution for $E = 10^{19}$ eV is depicted in Fig.5.5. Histograms used to deduce $X_{\max}$ resolutions for $E = 10^{18.5}$ eV, $\theta = 49°$ and for $E = 10^{19.5}$ eV, $\theta = 0..63°$ are depicted in Figs.5.11 and 5.13, respectively. Histogram used for the determination of the angular resolution for $E = 10^{20}$ eV is shown in Fig.5.14.

Results of the energy and $X_{\max}$ resolution analyses of the Stereo reconstruction on simulated data are summarized in Tables 5.6 and 5.7, respectively. Results of the angular resolution on simulated data are listed in Table 5.8.

Table 5.6: Energy resolution of the Multiple–eye reconstruction from Monte Carlo simulations. E assigns simulated energy of simulated primary protons, θ is zenith angle, N is the number of reconstructed events, $\langle E \rangle = \langle E_{\mathrm{rec}} - E_{\mathrm{sim}} \rangle$, see Fig.5.12, is the mean of energy distribution of reconstructed events. $R_{E-\mathrm{sim}}^{\mathrm{ste-abs}}$ is the absolute energy resolution of the Multiple–eye reconstruction, $R_{E-\mathrm{sim}}^{\mathrm{ste-rel}}$ is the relative energy resolution of the Multiple–eye reconstruction. Uncertainties correspond to statistical errors. In the case that there is not enough statistics, no quantities are calculated.

Log(E/eV)	θ [°]	N	$\langle E \rangle$ [EeV]	$R_{E-\mathrm{sim}}^{\mathrm{ste-abs}}$ [EeV]	$R_{E-\mathrm{sim}}^{\mathrm{ste-rel}}$ [%]
18.5	0	0	–	–	–
	18	2	–	–	–
	26	4	–	–	–
	32	17	0.05 ± 0.06	0.26 ± 0.04	8 ± 1
	38	42	0.09 ± 0.05	0.34 ± 0.04	10 ± 1
	41	49	0.11 ± 0.04	0.25 ± 0.03	8.0 ± 0.8
	45	57	0.17 ± 0.04	0.28 ± 0.03	9.0 ± 0.8
	49	112	0.20 ± 0.03	0.28 ± 0.02	9.0 ± 0.6
	53	105	0.17 ± 0.03	0.32 ± 0.02	10.0 ± 0.7
	57	125	0.20 ± 0.03	0.33 ± 0.02	10.3 ± 0.7

Continued on next page

Continued from previous page

| Log(E/eV)	θ [°]	N	$\langle E \rangle$ [EeV]	$R_{E-\text{sim}}^{\text{ste}-\text{abs}}$ [EeV]	$R_{E-\text{sim}}^{\text{ste}-\text{rel}}$ [%]
	60	122	0.22 ± 0.03	0.30 ± 0.02	9.6 ± 0.6
	63	136	0.26 ± 0.03	0.33 ± 0.02	10.3 ± 0.6
18.5	**0–63**	**771**	**0.19 ± 0.01**	**0.315 ± 0.008**	**9.9 ± 0.3**
19.0	0	38	-0.5 ± 0.2	1.4 ± 0.2	14 ± 2
	18	115	-0.1 ± 0.1	1.11 ± 0.07	11.1 ± 0.7
	26	197	0.22 ± 0.07	1.05 ± 0.05	10.5 ± 0.5
	32	359	0.12 ± 0.05	0.91 ± 0.03	9.1 ± 0.3
	38	330	0.09 ± 0.05	0.89 ± 0.03	8.9 ± 0.3
	41	609	0.12 ± 0.03	0.80 ± 0.02	8.0 ± 0.2
	45	512	0.07 ± 0.04	0.81 ± 0.03	8.1 ± 0.3
	49	852	0.05 ± 0.02	0.69 ± 0.02	6.9 ± 0.2
	53	593	0.11 ± 0.03	0.66 ± 0.02	6.6 ± 0.2
	57	712	0.18 ± 0.02	0.65 ± 0.02	6.5 ± 0.2
	60	417	0.24 ± 0.03	0.63 ± 0.02	6.3 ± 0.2
	63	569	0.40 ± 0.03	0.69 ± 0.02	6.9 ± 0.2
19.0	**0–63**	**5303**	**0.14 ± 0.01**	**0.782 ± 0.008**	**7.82 ± 0.08**
19.5	0	76	-1.7 ± 0.4	3.4 ± 0.3	10.7 ± 0.9
	18	177	-0.5 ± 0.2	2.8 ± 0.1	8.9 ± 0.5
	26	378	-0.1 ± 0.1	2.6 ± 0.1	8.3 ± 0.3
	32	664	-0.25 ± 0.09	2.37 ± 0.07	7.5 ± 0.2
	38	662	-0.18 ± 0.09	2.34 ± 0.06	7.4 ± 0.2
	41	769	-0.11 ± 0.08	2.21 ± 0.06	7.0 ± 0.2
	45	784	-0.49 ± 0.07	1.89 ± 0.05	6.0 ± 0.2
	49	840	-0.49 ± 0.06	1.69 ± 0.04	5.4 ± 0.1
	53	789	-0.35 ± 0.06	1.66 ± 0.04	5.2 ± 0.1
	57	690	-0.25 ± 0.07	1.72 ± 0.05	5.4 ± 0.1
	60	616	0.22 ± 0.06	1.50 ± 0.04	4.7 ± 0.1
	63	699	0.71 ± 0.05	1.38 ± 0.04	4.4 ± 0.1
19.5	**0–63**	**7144**	**-0.19 ± 0.02**	**2.00 ± 0.02**	**6.34 ± 0.05**
20.0	0	12	-0.6 ± 0.8	2.4 ± 0.6	2.4 ± 0.6
	18	84	-1.7 ± 0.5	4.6 ± 0.4	4.6 ± 0.4
	26	298	-1.1 ± 0.3	4.2 ± 0.2	4.2 ± 0.2
	32	412	-1.5 ± 0.2	4.3 ± 0.2	4.3 ± 0.2
	38	391	-2.0 ± 0.3	4.4 ± 0.2	4.4 ± 0.2
	41	681	-2.2 ± 0.2	4.1 ± 0.1	4.1 ± 0.1
	45	666	-2.5 ± 0.2	4.0 ± 0.1	4.0 ± 0.1
	49	969	-2.7 ± 0.1	3.90 ± 0.09	3.90 ± 0.09
	53	511	-2.5 ± 0.2	3.6 ± 0.1	3.6 ± 0.1
	57	1319	-1.8 ± 0.1	3.58 ± 0.07	3.58 ± 0.07
	60	777	-1.2 ± 0.1	3.34 ± 0.09	3.34 ± 0.09
	63	715	0.3 ± 0.1	3.05 ± 0.08	3.05 ± 0.08
20.0	**0–63**	**6835**	**-1.85 ± 0.05**	**3.90 ± 0.04**	**3.90 ± 0.04**
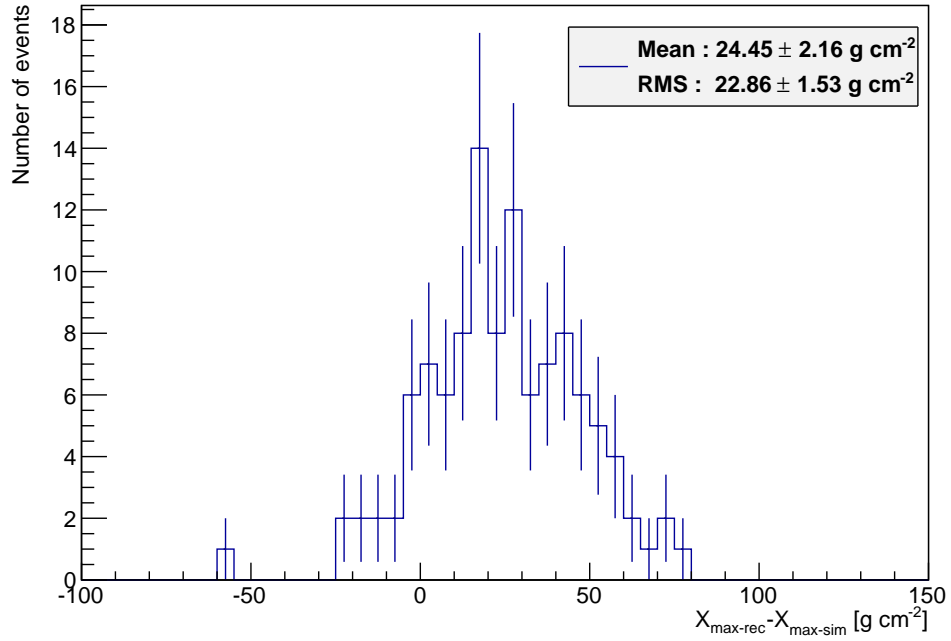
Figure 5.11: X_{max} resolution of the Stereo reconstruction for $\theta = 49°$. Simulated data for primary protons with energies of $10^{18.5}$ eV are shown.
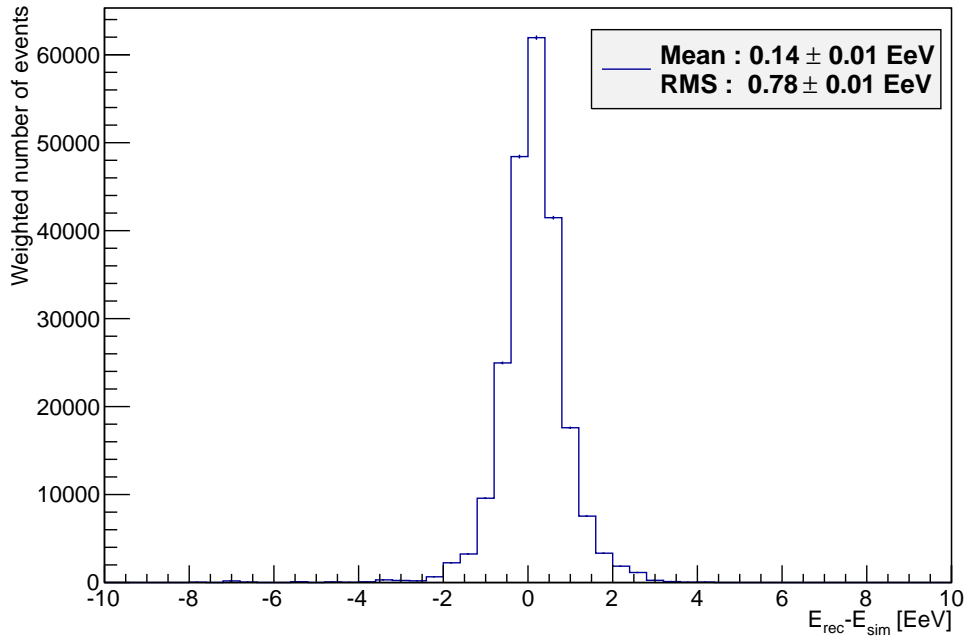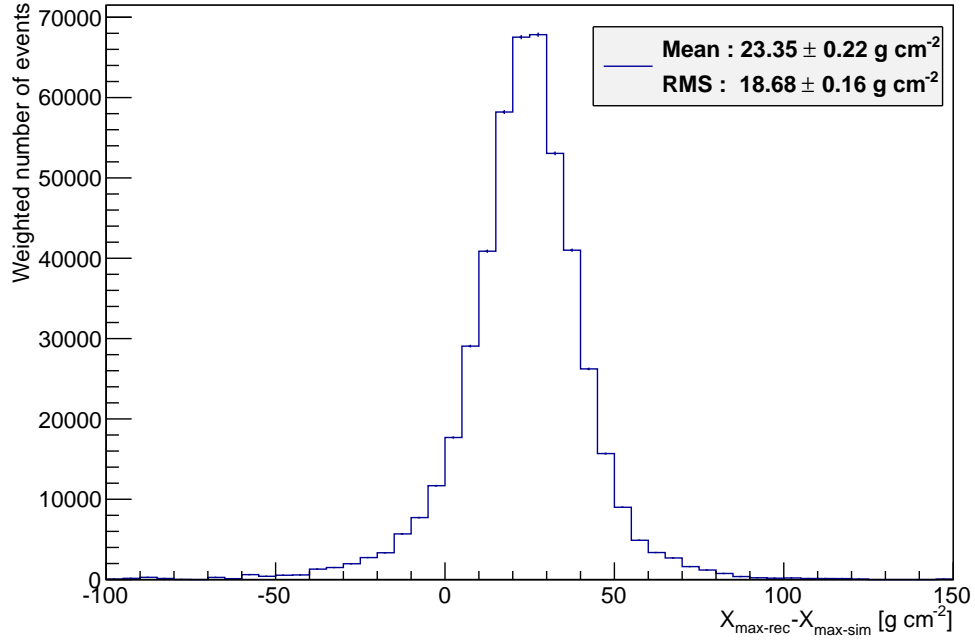

Figure 5.12: Energy resolution of the Stereo reconstruction for $\theta = 0..63°$. Simulated events are used. Energies of primary protons are 10^{19} eV.

Figure 5.13: X_{max} resolution of the Stereo reconstruction for $\theta = 0..63°$. Simulated data are depicted. Energies of primary protons are $10^{19.5}$ eV.
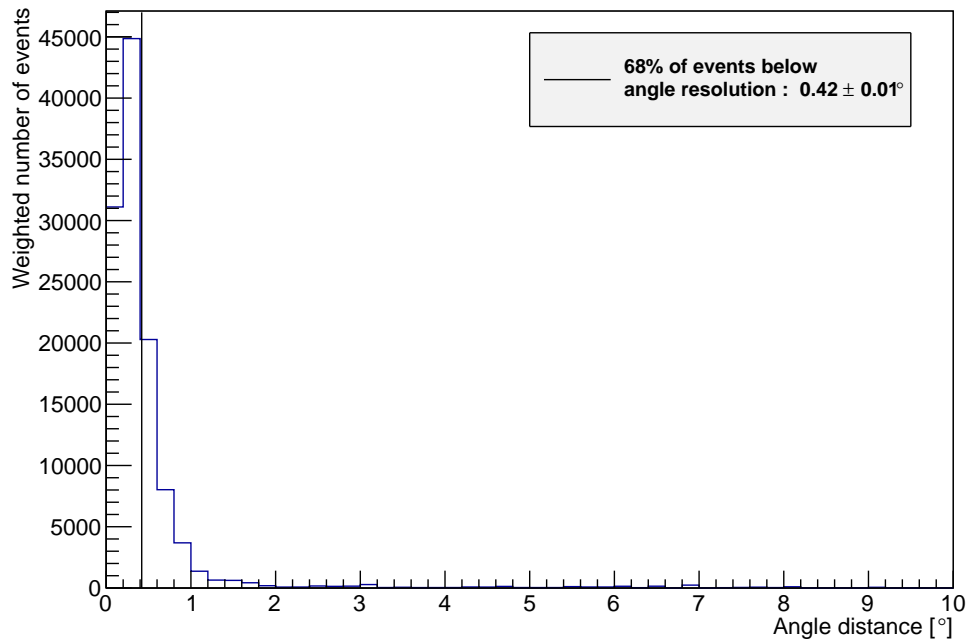
Figure 5.14: Angular resolution of the Stereo reconstruction for $\theta = 0..63°$. Simulated events for primary protons with energies of 10^{20} eV are shown. Vertical line marks the boundary below which 68% of events is found.

Table 5.7: $X_{\max}$ resolution of the Multiple–eye reconstruction from Monte Carlo simulations. $\langle X_{\max} \rangle = \langle X_{\max-\text{rec}} - X_{\max-\text{sim}} \rangle$, see Fig.5.11, is the mean of $X_{\max}$ distribution of reconstructed events. $R^{\text{ste}}_{X\max-\text{sim}}$ denotes the absolute $X_{\max}$ resolution of the Multiple–eye reconstruction. For more details see caption to Table 5.6.

Log(E/eV)	θ [°]	N	$\langle X_{\max} \rangle$ [g cm^{-2}]	$R^{\text{ste}}_{X\max-\text{sim}}$ [g cm^{-2}]
18.5	0	0	–	–
	18	2	–	–
	26	4	–	–
	32	17	7 ± 8	32 ± 6
	38	42	16 ± 5	29 ± 3
	41	49	17 ± 4	31 ± 3
	45	57	24 ± 3	23 ± 2
	49	112	24 ± 2	23 ± 2
	53	105	25 ± 3	27 ± 2
	57	125	30 ± 2	27 ± 2
	60	122	30 ± 3	29 ± 2
	63	136	37 ± 3	31 ± 2
18.5	**0–63**	**771**	**26 ± 1**	**28.7 ± 0.7**
19.0	0	38	7 ± 5	33 ± 4
	18	115	13 ± 3	28 ± 2
	26	197	20 ± 2	28 ± 1
	32	359	18 ± 1	25.2 ± 0.9
	38	330	21 ± 1	23.5 ± 0.9
	41	609	21.3 ± 0.9	21.3 ± 0.6
	45	512	21.9 ± 0.9	19.8 ± 0.6
	49	852	23.5 ± 0.6	18.2 ± 0.4
	53	593	26.7 ± 0.7	18.0 ± 0.5
	57	712	28.4 ± 0.7	17.4 ± 0.5
	60	417	30.6 ± 0.8	15.7 ± 0.5
	63	569	34.8 ± 0.7	17.6 ± 0.5
19.0	**0–63**	**5303**	**24.6 ± 0.3**	**20.9 ± 0.2**
19.5	0	76	-0.03 ± 3	26 ± 2
	18	177	11 ± 2	23 ± 1
	26	378	15 ± 1	21.3 ± 0.8
	32	664	19.0 ± 0.8	20.4 ± 0.6
	38	662	19.8 ± 0.8	21.5 ± 0.6
	41	769	21.9 ± 0.7	19.6 ± 0.5
	45	784	21.6 ± 0.6	16.7 ± 0.4
	49	840	24.7 ± 0.6	16.2 ± 0.4
	53	789	23.7 ± 0.6	15.7 ± 0.4
	57	690	26.7 ± 0.6	16.7 ± 0.5
	60	616	31.0 ± 0.6	15.1 ± 0.4
	63	699	33.2 ± 0.6	14.8 ± 0.4
19.5	**0–63**	**7144**	**23.4 ± 0.2**	**18.7 ± 0.2**
20.0	0	12	-2 ± 8	28 ± 6

Continued on next page

63

$\mathrm{Log}(E/\mathrm{eV})$	θ [°]	N	$\langle X_{\mathrm{max}}\rangle$ [g cm^{-2}]	$R^{\mathrm{ste}}_{X\mathrm{max-sim}}$ [g cm^{-2}]
	18	84	6 ± 2	23 ± 2
	26	298	11 ± 1	23 ± 1
	32	412	12 ± 1	21.8 ± 0.8
	38	391	19 ± 1	21.0 ± 0.8
	41	681	19.0 ± 0.7	17.2 ± 0.5
	45	666	18.8 ± 0.8	19.8 ± 0.5
	49	969	21.7 ± 0.5	15.9 ± 0.4
	53	511	24.3 ± 0.7	15.7 ± 0.5
	57	1319	25.9 ± 0.4	15.5 ± 0.3
	60	777	29.1 ± 0.5	13.8 ± 0.4
	63	715	32.3 ± 0.6	16.5 ± 0.4
20.0	**0–63**	**6835**	**22.2 ± 0.2**	**18.6 ± 0.2**

Table 5.8: Angular resolution of the Multiple–eye reconstruction from Monte Carlo simulations. $R^{\mathrm{ste}}_{\mathrm{ang-sim}}$ is the angular resolution of the Multiple–eye reconstruction. For more details see caption to Table 5.6.

$\mathrm{Log}(E/\mathrm{eV})$	θ [°]	N	$R^{\mathrm{ste}}_{\mathrm{ang-sim}}$ [°]
18.5	0	0	–
	18	2	–
	26	4	–
	32	15	1.5 ± 0.3
	38	34	0.9 ± 0.1
	41	43	0.83 ± 0.09
	45	51	0.72 ± 0.07
	49	88	0.72 ± 0.05
	53	87	0.55 ± 0.04
	57	115	0.68 ± 0.04
	60	112	0.56 ± 0.04
	63	131	0.58 ± 0.04
18.5	**0–63**	**682**	**0.660 ± 0.008**
19.0	0	33	0.73 ± 0.09
	18	91	0.71 ± 0.05
	26	159	0.76 ± 0.04
	32	271	0.73 ± 0.03
	38	223	0.51 ± 0.02
	41	398	0.58 ± 0.02
	45	321	0.51 ± 0.02
	49	502	0.39 ± 0.01
	53	368	0.36 ± 0.01
	57	470	0.38 ± 0.01
	60	296	0.34 ± 0.01
	63	416	0.32 ± 0.01
19.0	**0–63**	**3548**	**0.461 ± 0.001**

Log(E/eV)	θ [°]	N	$R_{\text{ang}-\text{sim}}^{\text{ste}}$ [°]
19.5	0	64	0.56 ± 0.05
	18	147	0.52 ± 0.03
	26	264	0.63 ± 0.03
	32	418	0.57 ± 0.02
	38	364	0.53 ± 0.02
	41	417	0.50 ± 0.02
	45	387	0.43 ± 0.02
	49	425	0.46 ± 0.02
	53	394	0.36 ± 0.01
	57	359	0.34 ± 0.01
	60	325	0.34 ± 0.01
	63	410	0.29 ± 0.01
19.5	**0–63**	**3974**	$\mathbf{0.483 \pm 0.001}$
20.0	0	11	0.37 ± 0.08
	18	70	0.49 ± 0.04
	26	203	0.61 ± 0.03
	32	250	0.58 ± 0.03
	38	195	0.49 ± 0.02
	41	306	0.47 ± 0.02
	45	300	0.46 ± 0.02
	49	404	0.40 ± 0.01
	53	208	0.39 ± 0.02
	57	545	0.34 ± 0.01
	60	351	0.31 ± 0.01
	63	349	0.25 ± 0.01
20.0	**0–63**	**3192**	$\mathbf{0.419 \pm 0.001}$

Resolutions of the Stereo reconstruction depends on the number of pixels included in the time and SDP fits, for details see Section 4.4. Because of that, the dependence on zenith angle is more evident in comparison to dependence on shower energy. It is caused by larger angular length of the shower axis in the FD camera for larger zenith angles.

The energy resolution is comparable to the resolution obtained from the Hybrid reconstruction. The angular resolution for energies above 10^{19} eV is even better then those received from the Hybrid reconstruction. The X_{max} resolution is comparable to the Hybrid reconstruction one as well, but there is a systematic shift in X_{max} of about 23 g cm^{-2}. This shift depends on zenith angle and is approximately identical for all energies. This implies that the shower geometry determination and the algorithm used for fluorescence light propagation are not in good agreement. Here is a field for further analyses and improvements.

5.3.2 Data

Energy, X_{max} and angular resolutions can be determined from experimental data. In the Stereo reconstruction, there exists two or more energies and X_{max}'s
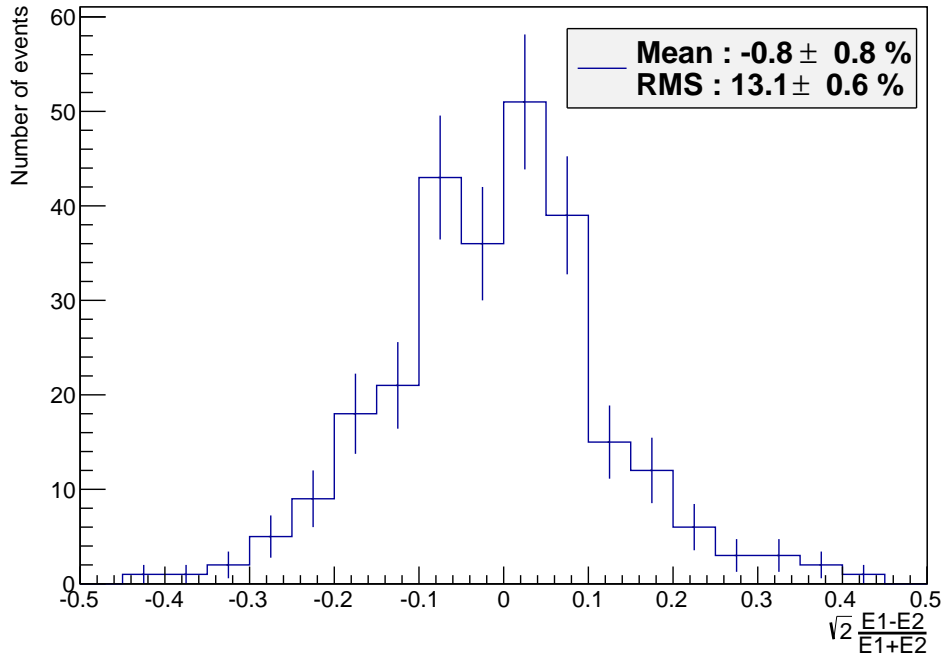
Figure 5.15: Relative energy resolution of the Stereo reconstruction obtained from experimental data.

reconstructions. Histograms of differences between reconstructed energies and X_{max}'s can be created. From such distributions the energy and X_{max} resolutions can be calculated. Results of the energy and X_{max} resolution analyses of the Stereo reconstruction on experimental data are shown in Figs.5.15 and 5.16, respectively.

For the determination of the angular resolution of the Stereo reconstruction from experimental data the method of so called triple events is used. If shower is viewed from three or four FD stations, three or more separate Stereo reconstructions can be performed, if we exclude one or more eye. From the distribution of angular distances between separately reconstructed triple events, the angular resolution of the Stereo reconstruction can be calculated. The angular resolution derived from experimental data is shown in Fig.5.17, only reconstructions from neighbour eyes are included.

I have obtained the energy resolution of the Multiple–eye reconstruction as

$$R_{\mathrm{E-dat}}^{\mathrm{ste}} = 13.1 \pm 0.6\%. \tag{5.4}$$

The value of the X_{max} resolution of the Multiple–eye reconstruction has been calculated as

$$R_{\mathrm{Xmax-dat}}^{\mathrm{ste}} = 24.5 \pm 1.1 \ \mathrm{g \ cm}^{-2} \tag{5.5}$$

and the angular resolution of the Multiple–eye reconstruction has been estimated as

$$R_{\mathrm{ang-dat}}^{\mathrm{ste}} = 1.06 \pm 0.04^{\circ} \tag{5.6}$$

Uncertainties correspond to statistical errors.

Stereo X$_{max}$ resolution, 268 events
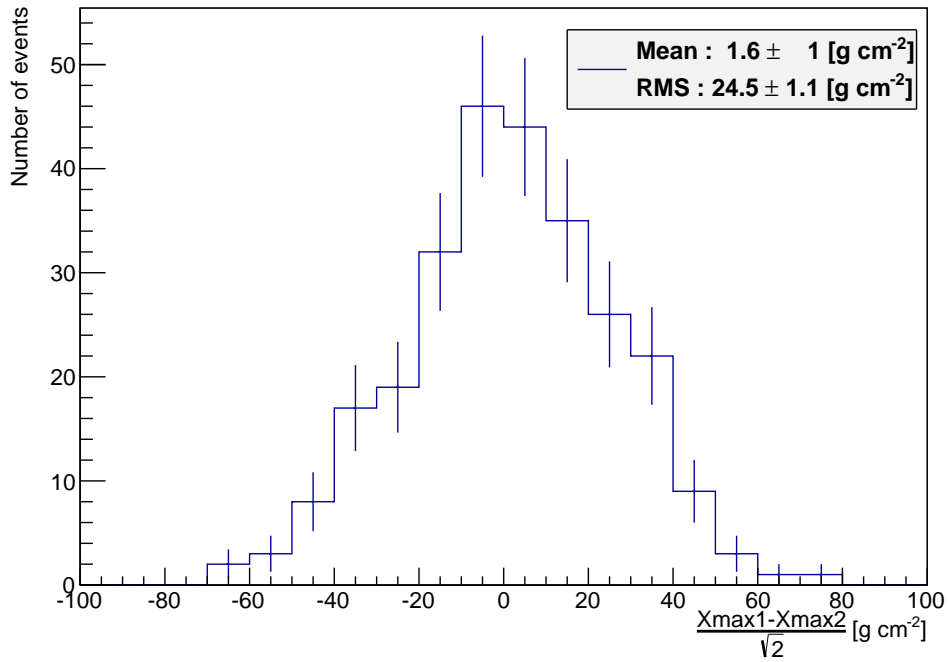
Figure 5.16: Relative $X_{\max}$ resolution of the Stereo reconstruction as deduced from experimental data.

Stereo angular distance, 308 events
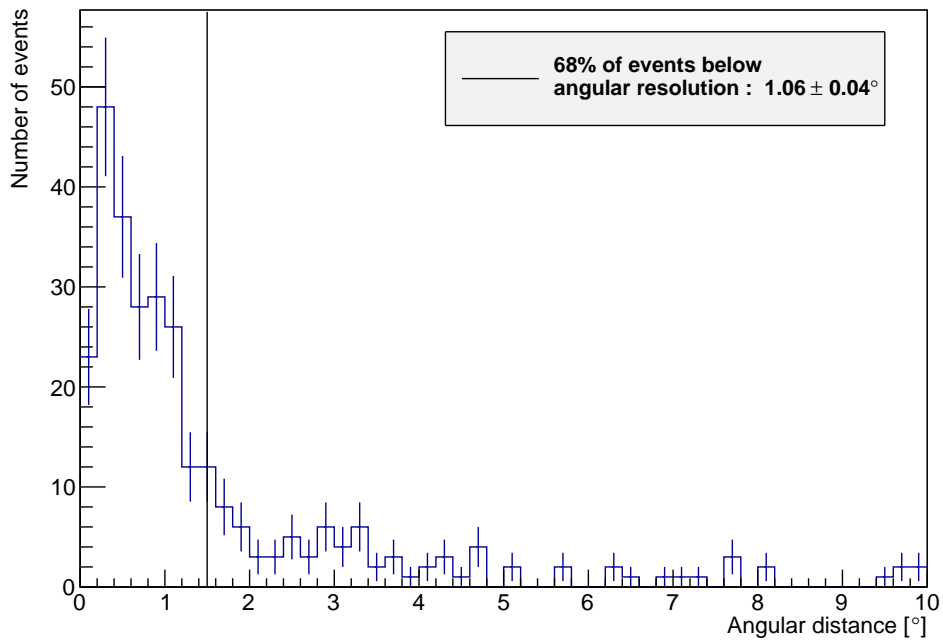
Figure 5.17: Angular resolution of the Stereo reconstruction obtained from experimental data. Vertical line marks the boundary below which 68% of events is found.

Stereo angular distance, 243 events

68% of events below
angular resolution : $0.87 \pm 0.04°$
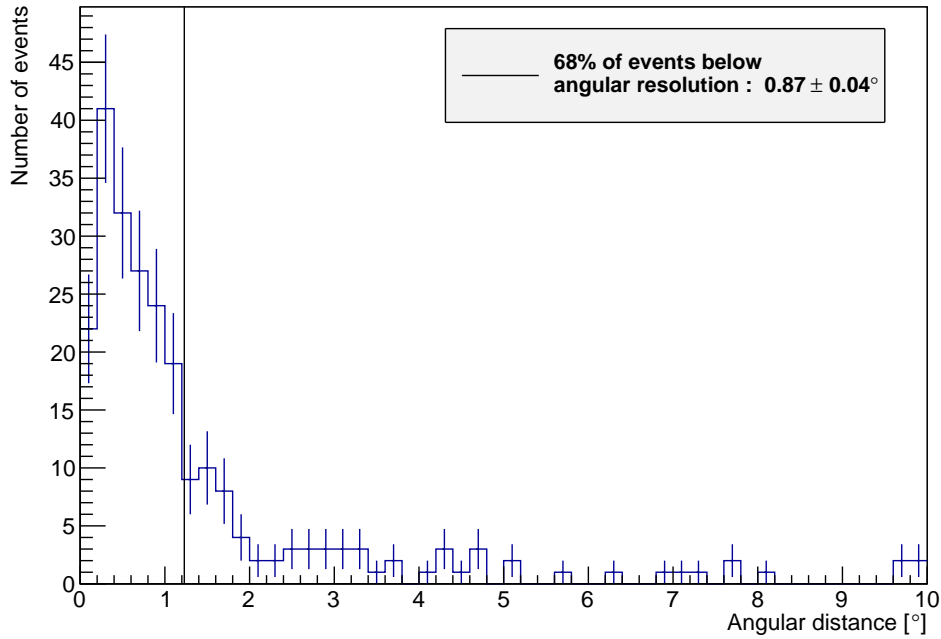
Figure 5.18: Angular resolution of the Stereo reconstruction calculated from experimental data. Additional cut for angular length $> 20°$ is added. Vertical line marks the boundary below which 68% of events is found.

Resolutions obtained from experimental data are worse then the one obtained from simulations. This can be caused by atmospheric conditions. The experimental energy and X_{max} resolutions are worse in comparison to the one obtained from the Hybrid reconstruction. This may be caused by the improper accounting for fluorescence light propagation reconstruction in the Stereo reconstruction. Also, the sizes of data sets play the role. Not every EASs reconstructed by the Hybrid reconstruction can be reconstructed by the Stereo reconstruction. For the Hybrid angular resolutions, the number of reconstructions is the same as the number of eyes which see the shower. For the simulated Stereo angular resolutions only one event per shower is reconstructed. The experimental Stereo angular resolution is determined by the triple event method described above. Its experimental angular resolution is better then the Hybrid reconstruction one. This fact corresponds to the results of analysis on simulated events.

Accuracy of the Stereo reconstruction depends on the angular length of the shower axis in the FD camera. This effect is illustrated in Fig.5.18, where the additional cut for angular length $> 20°$ is added. In this case, the angular resolution is better.

Analysis presented in this thesis shows that Multiple–eye reconstruction is a valuable reconstruction technique and has similar energy, X_{max} and angular resolutions as the Hybrid reconstruction which is mainly used at the Pierre Auger Observatory. Moreover, there is a room to make the Stereo analysis better to achieve more trustworthy estimates.

Conclusions

In this thesis, the cosmic rays at very high energies were studied. Especially, reconstruction techniques used to estimate shower parameters were studied. For this purpose, the data collected at the Pierre Auger Observatory for almost eight years of its operation as well as the simulated events prepared by the Auger group were adopted.

I made use of Monte Carlo tool CORSIKA with the thinning algorithm turned on to simulate extensive air showers. I simulated depths of shower maxima X_{max} as a function of energy. In accord with other analyses, my analysis suggests heavier nuclei as primary particles at higher energies and proton composition at lower energies.

Calculation of the Multiple–eye reconstruction resolutions was the main goal of the work. At the Pierre Auger Observatory, the Surface Detector reconstruction and the Hybrid reconstruction are currently used. Multiple–eye reconstruction is a valuable crosscheck of an accuracy of the Hybrid reconstruction method, because it does not use information from the surface detector.

I compared above mentioned three types of reconstruction and estimated their reconstruction resolutions both from the experimental and simulated data.

Energy resolutions of the Hybrid and Multiple–eye reconstructions are better than the Surface Detector reconstruction one. In case of angular resolution, it depends on energy. The Multiple–eye method yields similar resolutions to the Hybrid reconstruction, although a systematic shift in the reconstruction of X_{max} exists. This fact should be further analysed.

Calculated resolutions of the Surface Detector and Hybrid reconstructions are in overall agreement with the ones officially published by the Pierre Auger Collaboration. Energy, X_{max} and angular Multiple–eye reconstruction resolutions are the original results of this thesis.

Bibliography

[1] Centre de Calcul de l'Institut National de Physique Nucléaire et de Physique des Particules (CC-IN2P3).
`http://cc.in2p3.fr/`. 11. 11. 2012.

[2] The Auger Observer.
`http://augerobserver.fzk.de/`. 11. 11. 2012.

[3] The Pierre Auger Project Design Report. Tech. rep., 1996.

[4] ABRAHAM, J., ET AL. Properties and performance of the prototype instrument for the Pierre Auger Observatory. *Nucl.Instrum.Meth. A523* (2004), 50–95.

[5] ABRAHAM, J., ET AL. The Cosmic Ray Energy Spectrum and Related Measurements with the Pierre Auger Observatory. 0906.2189.

[6] ABRAHAM, J., ET AL. Measurement of the Depth of Maximum of Extensive Air Showers above 10^{18} eV. *Phys.Rev.Lett. 104* (2010), 091101, 1002.0699.

[7] ABRAHAM, J., ET AL. Measurement of the energy spectrum of cosmic rays above 10^{18} eV using the Pierre Auger Observatory. *Phys.Lett. B685* (2010), 239–246, 1002.1975.

[8] ABRAHAM, J., ET AL. The Fluorescence Detector of the Pierre Auger Observatory. *Nucl.Instrum.Meth. A620* (2010), 227–251, 0907.4282.

[9] ABREU, P., ET AL. The Pierre Auger Observatory II: Studies of Cosmic Ray Composition and Hadronic Interaction models. 1107.4804.

[10] ABU-ZAYYAD, T., ET AL. HiRes/MIA measurements of extensive air shower development between 10**17-eV and 10**18-eV: Detector description and performance.

[11] ALLISON, P. Microwave detection of cosmic ray showers at the Pierre Auger Observatory.

[12] ANDREWS, D., ET AL. General results from the haverah park large e.a.s. array. *Conf.Proc. C690825* (1969), 337–342.

[13] ANTONI, T., ET AL. The cosmic-ray experiment KASCADE. *Nuclear Instruments and Methods in Physics Research A 513* (Nov. 2003), 490–510.

[14] ARGIRO, S., ET AL. The Offline Software Framework of the Pierre Auger Observatory. *Nucl.Instrum.Meth. A580* (2007), 1485–1496, 0707.1652.

[15] ARMENGAUD, E., SIGL, G., BEAU, T., AND MINIATI, F. Crpropa: a numerical tool for the propagation of uhe cosmic rays, gamma-rays and neutrinos. *Astropart.Phys. 28* (2007), 463–471, astro-ph/0603675.

[16] ARTAMONOV, V., ET AL. Present state and outlook of the Yakutsk EAS array. *Bull.Russ.Acad.Sci.Phys. 58* (1994), 2026–2031.

[17] BALLARINI, F., ET AL. The FLUKA code: an overview. *Journal of Physics Conference Series 41* (May 2006), 151–160.

[18] BELLIDO, J., CLAY, R., DAWSON, B., AND JOHNSTON-HOLLITT, M. Southern hemisphere observations of a 10**18-eV cosmic ray source near the direction of the galactic center. *Astropart.Phys. 15* (2001), 167–175, astro-ph/0009039.

[19] BENZVI, S., ET AL. The Lidar System of the Pierre Auger Observatory. *Nucl.Instrum.Meth. A574* (2007), 171–184, astro-ph/0609063.

[20] BHATTACHARJEE, P., AND SIGL, G. Origin and propagation of extremely high-energy cosmic rays. *Phys.Rept. 327* (2000), 109–247, astro-ph/9811011.

[21] BLEICHER, M., ET AL. Relativistic hadron hadron collisions in the ultrarelativistic quantum molecular dynamics model. *J.Phys. G25* (1999), 1859–1896, hep-ph/9909407.

[22] BONIFAZI, C. The angular resolution of the Pierre Auger Observatory. *Nucl.Phys.Proc.Suppl. 190* (2009), 20–25, 0901.3138.

[23] BRUN, R., AND RADEMAKERS, F. ROOT - An object oriented data analysis framework. *Nuclear Instruments and Methods in Physics Research A 389* (Feb. 1997), 81–86.

[24] CASO, C., ET AL. Review of particle physics. Particle Data Group. *Eur.Phys.J. C3* (1998), 1–794.

[25] CRONIN, J. W. The Highest - energy cosmic rays. *Nucl.Phys.Proc.Suppl. 138* (2005), 465–491, astro-ph/0402487.

[26] CRONIN, J. W. Recent results from the Pierre Auger Observatory. 0911.4714.

[27] CSÖRGÖ, T., ET AL. Elastic Scattering and Total Cross-Section in $p + p$ reactions measured by the LHC Experiment TOTEM at $\sqrt{s} = 7$ TeV. *Prog.Theor.Phys.Suppl. 193* (2012), 180–183, 1204.5689.

[28] DRESCHER, H. J., HLADIK, M., OSTAPCHENKO, S., PIEROG, T., AND WERNER, K. Parton-based Gribov-Regge theory. *Physics Reports350* (Sept. 2001), 93–289, arXiv:hep-ph/0007198.

[29] ETCHEGOYEN, A. AMIGA, Auger Muons and Infill for the Ground Array. 0710.1646.

[30] FESEFELDT, H. THE SIMULATION OF HADRONIC SHOWERS: PHYSICS AND APPLICATIONS.

[31] FLETCHER, R. S., GAISSER, T. K., LIPARI, P., AND STANEV, T. sibyll: An event generator for simulation of high energy cosmic ray cascades. *Phys. Rev. D50* (Nov. 1994), 5710–5731.

[32] GAISSER, T. Cosmic rays and particle physics.

[33] GAISSER, T. K., AND HILLAS, A. M. Reliability of the method of constant intensity cuts for reconstructing the average development of vertical showers. In *International Cosmic Ray Conference* (1977), vol. 8 of *International Cosmic Ray Conference*, pp. 353–357.

[34] GREISEN, K. End to the cosmic ray spectrum? *Phys.Rev.Lett. 16* (1966), 748–750.

[35] HAUNGS, A., REBEL, H., AND ROTH, M. Energy spectrum and mass composition of high-energy cosmic rays. *Rept.Prog.Phys. 66* (2003), 1145–1206.

[36] HECK, D., KNAPP, J., CAPDEVIELLE, J. N., SCHATZ, G., AND THOUW, T. *CORSIKA: a Monte Carlo code to simulate extensive air showers.* Feb. 1998.

[37] HECK, D., AND PIEROG, T. Extensive air shower simulation with corsika: A user's guide.
http://www-ik.fzk.de/~corsika/usersguide/corsika_tech.html,
2013. 1. 3. 2013.

[38] HECK, D., RISSE, M., AND KNAPP, J. Comparison of hadronic interaction models at Auger energies. *Nucl.Phys.Proc.Suppl. 122* (2003), 364–367, astro-ph/0210392.

[39] HEITLER, W. *Quantum theory of radiation.* 1954.

[40] HILLAS, A. Shower simulation: Lessons from MOCCA. *Nucl.Phys.Proc.Suppl. 52B* (1997), 29–42.

[41] HILLAS, A. M. Cosmic rays in an evolving universe. *Canadian Journal of Physics 46* (1968), 623.

[42] KALMYKOV, N. N., AND OSTAPCHENKO, S. S. The nucleus-nucleus interaction, nuclear fragmentation, and fluctuations of extensive air showers. *Physics of Atomic Nuclei 56* (Mar. 1993), 346–353.

[43] KAMATA, K., AND NISHIMURA, J. The Lateral and the Angular Structure Functions of Electron Showers. *Progress of Theoretical Physics Supplement 6* (1958), 93–155.

[44] KASAHARA, K., ET AL. The current status and prospect of the ta experiment. astro-ph/0511177.

[45] KEILHAUER, B., AND WILL, M. Description of Atmospheric Conditions at the Pierre Auger Observatory Using Meteorological Measurements and Models. *Eur.Phys.J.Plus 127* (2012), 96, 1208.5417.

[46] KUEMPEL, D., KAMPERT, K.-H., AND RISSE, M. Geometry reconstruction of fluorescence detectors revisited. *Astropart.Phys. 30* (2008), 167–174, 0806.4523.

[47] LONGAIR, M. High-energy astrophysics. Vol. 1: Particles, photons and their detection.

[48] LOUEDEC, K., LOSNO, R., AND LOSNO, R. Atmospheric aerosols at the Pierre Auger Observatory and environmental implications. *Eur.Phys.J.Plus 127* (2012), 97, 1208.6275.

[49] MATTHEWS, J. A Heitler model of extensive air showers. *Astropart.Phys. 22* (2005), 387–397.

[50] MEURER, C., AND SCHARF, N. HEAT - a low energy enhancement of the Pierre Auger Observatory. *Astrophys.Space Sci.Trans. 7* (2011), 183–186, 1106.1329.

[51] MOSTAFA, M. The Hybrid Activities of the Pierre Auger Observatory. *Nucl.Phys.Proc.Suppl. 165* (2007), 50–58, astro-ph/0608670.

[52] NAGANO, M., AND WATSON, A. A. Observations and implications of the ultrahigh-energy cosmic rays. *Rev.Mod.Phys. 72* (2000), 689–732.

[53] NELLEN, L. The Pierre Auger Observatory: Status, results and outlook. *Nucl.Phys.Proc.Suppl. 188* (2009), 233–238.

[54] NOVOTNÝ, V. Highest energy cosmic ray propagation. Bachelor's thesis, Charles University in Prague, 2011.

[55] PEIXOTO, C. J. T., DE SOUZA, V., AND BELLIDO, J. Comparison of the moments of the Xmax distribution predicted by different cosmic ray shower simulation models. 1301.5555.

[56] PENZIAS, A. A., AND WILSON, R. W. A Measurement of excess antenna temperature at 4080-Mc/s. *Astrophys.J. 142* (1965), 419–421.

[57] PIEROG, T. Lhc data and extensive air showers. In *International Symposium on Very High Energy Cosmic Ray Interactions* (2013).

[58] PIEROG, T., AND WERNER, K. EPOS Model and Ultra High Energy Cosmic Rays. *Nuclear Physics B Proceedings Supplements 196* (Dec. 2009), 102–105, 0905.1198.

[59] PROTHEROE, R. Acceleration and interaction of ultrahigh-energy cosmic rays. astro-ph/9812055.

[60] RANFT, J. Dual parton model at cosmic ray energies. *Phys. Rev. D51* (Jan. 1995), 64–84.

[61] REVENU, B. Overview of MHz air shower radio experiments and results. 1302.2733.

[62] SCHMIDT, F. Measurements of the Muon Content of UHECR Air Showers with the Pierre Auger Observatory. *Nucl.Phys.Proc.Suppl. 196* (2009), 141–146, 0902.4613.

[63] SOKOLSKY, P. Final results from the High Solution Fly's Eye (HiRes) experiment. *Nucl.Phys.Proc.Suppl. 212-213* (2011), 74–78.

[64] SOKOLSKY, P. Final results from the High Solution Fly's Eye (HiRes) experiment. *Nucl.Phys.Proc.Suppl. 212-213* (2011), 74–78.

[65] TESHIMA, M., ET AL. EXPANDED ARRAY FOR GIANT AIR SHOWER OBSERVATION AT AKENO. *Nucl.Instrum.Meth. A247* (1986), 399.

[66] THAKURIA, C. C., AND BORUAH, K. Comparison of EPOS and QGSJET-II in EAS Simulation using CORSIKA. 1202.3661.

[67] TSUNESADA, Y. Highlights from Telescope Array. 1111.2507.

[68] ULRICH, R. M. *Measurement of the proton-air cross section using hybrid data of the Pierre Auger Observatory.* PhD thesis, Universität Karlsruhe, 2007. GAP Note 2008-004.

[69] VOROBIOV, S. The Pierre Auger Observatory - a new stage in the study of the ultra-high energy cosmic rays. 0811.0752.

[70] VÍCHA, J. Aspects of energy calibration of cosmic ray showers detected by surface detector at the pierre auger observatory. Master's thesis, Czech Technical University in Prague, 2010.

[71] WERNER, K. Strings, pomerons and the VENUS model of hadronic interactions at ultrarelativistic energies. *Physics Reports232* (Sept. 1993), 87–299.

[72] ZATSEPIN, G., AND KUZMIN, V. Upper limit of the spectrum of cosmic rays. *JETP Lett. 4* (1966), 78–80.

List of Tables

List of Figures

List of Abbreviations

ADC   Analog to Digital Converter

CIC   Constant Intensity Cut

CIRB   Cosmic Infrared Background radiation

CLF   Central Laser Facility

CMB   Cosmic Microwave Background radiation

CR   Cosmic Ray

EAS   Extensive Air Shower

FD   Fluorescence Detector

GZK   Geiser–Zatsepin–Kuzmin cutoff

LDF   Lateral Distribution Function

RMS   Root Mean Square

RSS   Residual Sum of Squares

SD   Surface Detector

SDP   Shower–Detector Plane

UHECR   Ultra–High Energy Cosmic Ray

VEM   Vertical Equivalent Muon